NOTE TO USERS

Dissertation

Seasonal variations of Diurnal and semidiurnal tidal-period perturbations in mesopause region temperature and zonal and meridional winds above Ft. Collins, CO (40°N, 105°W) based on Na-Lidar observation over full diurnal cycles

Submitted by
Tao Yuan
Department of Physics

In partial fulfillment of the requirements
for the Degree of Doctor of Philosophy
Colorado State University
Fort Collins, Colorado
June 2004

INFORMATION TO USERS

The quality of this reproduction is dependent upon the quality of the copy submitted. Broken or indistinct print, colored or poor quality illustrations and photographs, print bleed-through, substandard margins, and improper alignment can adversely affect reproduction.

In the unlikely event that the author did not send a complete manuscript and there are missing pages, these will be noted. Also, if unauthorized copyright material had to be removed, a note will indicate the deletion.

ProQuest Information and Learning Company
300 North Zeeb Road
P.O. Box 1346
Ann Arbor, MI 48106-1346

COLORADO STATE UNIVERSITY

June 11th, 2004

WE HEREBY RECOMMEND THAT THE DISSERTATION PREPARED UNDER OUR SUPERVISION BY TAO YUAN ENTITLED "SEASONAL VARIATIONS OF DIURNAL AND SEMIDIURNAL TIDAL-PERIOD PERTURBATIONS IN MESOPAUSE REGION: TEMPERATER, ZONAL AND MERIDIONAL WINDS ABOVE FORT COLLINS, CO (40°N, 105°W) BASE ON NA-LIDAR OBSERVATION OVER FULL DIURNAL CYCLES" BE ACCEPTED AS FULFULLING IN PART REQUIREMENTS FOR THE DEGREE OF DOCTOR OF PHILOSOPHY.

Committee On Graduate Work

Adviser

Co-Adviser

Department Head

Abstract of Dissertation

Seasonal variations of diurnal and semidiurnal tidal-period perturbations in mesopause region temperature and zonal and meridional winds above Ft. Collins, CO (40°N, 105°W) based on Na-Lidar observation over full diurnal cycles

With continued efforts by all the members (past and present) in the Na-Lidar group at Colorado State University, the lidar system was capable of simultaneous measurement of mesopause region temperature and horizontal wind at night. Since May 2002, the CSU fluorescence lidar system has been able to perform these observations on 24-hour continuous basis for a long-period, weather permitting. The key factor, which makes lidar observation under sunlit conditions possible, is a pair of robust (reliable and stable) Faraday filters that reduces the sky background. To attain such a Faraday Filter, in this thesis we developed and implemented dual temperature control (to ±0.1K) of sodium cell inside the filters, and of the cell's tip-off region. The dual control allows independent setting of cell temperature and the Na vapor pressure, thus stabilizing Na vapor density in the cell and the transmission function of the Faraday filter.

This 24-hour continuous observation capability provided us with the first yearlong data set with campaigns of full diurnal cycle coverage leading to the first study of diurnal and semidiurnal tides of mesopsuse region temperature, zonal and meridional winds based on ground based observation. The yearlong data set include a total of 1,491 hours with 659 hours under sunlit conditions, within which there are 29 sets of 24-hour continuous observation. We binned these 29 data sets into bimonthly time series and performed harmonic analysis to deduce diurnal mean, diurnal and semidiurnal tidal-period oscillations of the mesopause region temperature, zonal and meridional winds over Fort Collins, CO.

The resulting bimonthly tidal amplitudes and phases are compared to the predictions of Global Scale Wave Models (GSWM00 and GSWM02) and Thermosphere, Ionosphere, Mesosphere and Electrodynamics - General Circulation Model (TIME-GCM02). Other than diurnal temperatures in Nov-Dec, we found excellent agreement between observation and GSWM00 model for diurnal tides, suggesting that migrating solar tides dominate the observed oscillations. The observed diurnal temperature phase in Nov-Dec suggests the existence of midnight local heating, which requires further study. For non-winter months, all three models considerably underestimate the semidiurnal amplitudes, implicating the existence of considerable local wave perturbations at or near semidiurnal period. At the present, the causes for the discrepancy between observation and model prediction are not understood. For the bimonthly periods with significant discrepancy between observation and model predictions, analysis of more recent data taken during the same bimonthly periods showed general agreement between two data sets. Continued observation for two additional years is planned. At the end of that time, we should have enough data to determine not only tidal climatology but also tidal variability, revealing unexpected interactions between tides and gravity waves and planetary waves. Our results will provide complementary information to satellite observations which provide global but lack local-time coverage. In collaboration with modeling efforts at National Center for Atmospheric Research, our data set hopefully will play a significant role in advancing our understanding of solar tides and their roles in the structure and dynamics of the Mesosphere and Lower Thermosphere.

Tao Yuan

Department of Physics

Colorado State University

Fort Collins, CO 80523

Summer 2004

Table of Contents

List of figures:

Chapter 1 Introduction

This chapter introduces some basic definitions and techniques of the Lidar system, followed by the motivation of this research project. Basic knowledge of the mesopause region and interesting atmospheric phenomena in this region are then discussed. Since history can help us understand the present better, the milestone achievements of the CSU Na-Lidar are briefly presented. Finally the structure of the thesis will be presented.

1-1 What is Lidar?

Lidar is an acronym for light detection and ranging. Its major scientific use is for measuring the properties of the earth's atmosphere. It relies on the interactions, scattering, and/or absorption, of a beam of light by the constituents of the atmosphere. In general, a laser beam is sent through the atmosphere. Then, the selected atmospheric information along the path of laser beam may be retrieved from the returned signal by a telescope, which is aligned along the laser beam direction. Depending on the design of the lidar, a variety of atmospheric parameters may be measured. These parameters may range from atmospheric state parameters such as temperature, pressure, and density, to dynamic properties such as waves and turbulence, to species detection such as pollutant concentration, water vapor concentration, as well as clouds and ice particles.

There have been various lidar techniques developed, such as differential absorption lidar (DIAL), Raman lidar, Rayleigh lidar, Mie or aerosol lidar, and, of course,

fluorescence lidar. These techniques use different scattering mechanisms, which provides the return signal. DIfferential Absorption Lidar (DIAL) is used to measure chemical and species concentrations (such as ozone, water vapor, and pollutants) in the atmosphere. A DIAL lidar uses two different laser wavelengths, which are so selected that one of the wavelengths is absorbed by the molecule of interest while the other wavelength is not. The difference in the line-of-sight derivative of intensity of the two return signals can be used to deduce the concentration of the molecule being investigated. Mie lidar, on the other hand, takes advantage of the elastic Mie-backscattering by the large particles in the atmosphere (larger than the laser wavelength), such as dust, and is used to measure the temporal and spatial distributions of aerosol and clouds. Raman lidar uses the light which is up or downshifted in frequencies by inelastic Raman scattering from constituent molecules of the atmosphere to detect their abundance and density distribution. Often, by comparing Raman scattering signal from different frequency components of nitrogen and/or oxygen molecules, one can determine atmospheric temperature. Rayleigh lidar uses quasi-elastic Rayleigh scattering by the air molecules to deduce temperature, density and other parameters from the spectrally broadened return signal.

The lidar based on non-resonant Rayleigh and Raman scattering can be used to infer the temperature by iterative integration assuming that the atmosphere is an ideal gas and in hydrostatic equilibrium. This relates the temperature (T), pressure (p), average molar mass (M) of the atmosphere, mass density (ρ), and altitude (z) by

$$p = \left(\frac{\rho}{M}\right) RT \quad \text{and} \quad \frac{\partial p}{\partial z} = -\rho g \tag{1-1}$$

where $R=8.3145\ J/molK$ is the ideal gas constant and g is the acceleration due to gravity. The iterative procedure requires an initial temperature at the top altitude, which is normally obtained by an educated guess based on a model, rendering the deduced temperatures in the highest ~10km inaccurate. This along with air density decreasing with altitude at the exponential rate and the relatively weak non-resonance scattering processes [She, 1990], limits the temperature measurement by a non-resonance lidar to below ~ 80km, depending on the laser power and the size of the receiving telescope. For a discussion of this method of temperature profiling, see Hauchecorne and Chanin [1980].

The fluorescence lidar, like CSU Na-Lidar, utilizes resonance scattering of the atmospheric constituents (mostly metal atoms, so it also called Metal fluorescence lidar) to determine the dynamical parameters of that constituent. Assuming thermal equilibrium among atmosphere constituents, which is the case in the mesopause region, temperature and wind so determined are faithful proxy for the atmosphere.

Because the laser pulses are tuned to the resonance frequency of the atomic line of certain species, the scattering cross-section is enhanced by as much as a factor of $\sim 10^{14}$-10^{15} over Rayleigh scattering of that specific species (For Na, the peak cross section is $14.9\times10^{-16}m^2$). So, a much weaker pulse, compared with that required for the non-resonance lidar, has appreciatable return signal, even though the air molecule density is an order of 10 larger than sodium atom density. Also, metal fluorescence lidar measures temperature and wind directly, and does not rely on any assumptions about the hydrostatic equilibrium or guessed initial values. By now there are several kinds of fluorescence lidar in operation, such as sodium lidar, potassium lidar and iron lidar.

These metal fluorescence lidars could all offer high temporal and spatial resolution profiles of the thermal and dynamic properties of the mesopause region and they are getting more popular and widely used for the studies of the middle and upper atmosphere.

1-2 Introduction of the mesopause region

Based on the vertical thermal structure of the earth atmosphere, scientists divide atmosphere into four layers. In the order of altitude increasing, they are troposphere, stratosphere, mesosphere and thermosphere, separated by temperature minimum or maximum. These regions where the temperature reaches the minimum or maximum are denoted as the '-pause' of the layer below it (see Fig.1-1).

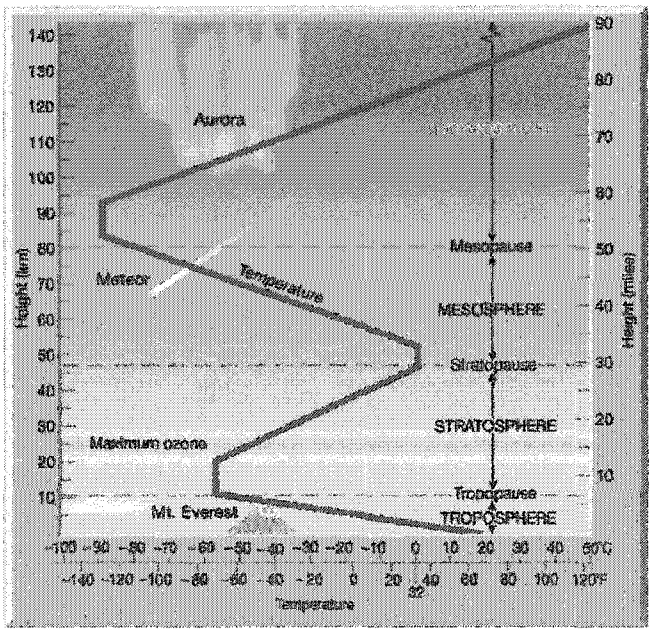

Fig. 1-1 Vertical Thermal structure of Earth atmosphere

Why is this region of atmosphere so special that scientists have been developing all kinds of techniques, such as satellites, rocket campaign and advanced remote-sensing instruments, to explore it (weather balloons is not an option here due to high altitude of

the mesopause)? It is the coldest region of the terrestrial atmosphere, and has a counter-intuitive seasonal temperature dependence with summer being colder than winter, even though it is under constant solar radiation in summer while in darkness throughout the winter. The polar mesopause region, where the counter-intuitive summer-winter difference is as much as 70K, has been proposed as the "miner's canary of global change" [Thomas, 1996], anticipating early observable anthropogenic changes of the atmosphere occurring in the mesopause region. It is also the region of atmosphere that links the space weather environment to the terrestrial weather environment. The mesopause observations can also be used for ionosphere lower boundary condition, as this region happens to cover the bottom of the ionosphere.

Metallic elements are deposited in the atmosphere at ~ 100km, believed to be a by-product of meteors' vaporization on entering the atmosphere. Below about 80km, the atmosphere is too dense for these elements to exist in their atomic form, and they tend to bind with other atoms or radicals to form molecules. The result is a layer of these metallic elements in their atomic form, at the height of the mesopause region (See Fig.1-1). Of particular interest here is the sodium layer, which generally occupies altitudes between 80 and 110km of the mesopause providing an ideal tracer for fluorescence measurements in this region. The peak density of these neutral Na atoms, 10^9 to 10^{10} m^{-3}, typically occurs around 92km.

As we can see from Fig.1-1, the mesopause region exhibits the lowest the temperature in the earth atmosphere, falling to as low as 175K for the nightly mean in the midlatitudes [She *et. al.*, 2000]. Contrary to people's common sense, this region experiences the lowest temperature in the middle of summer and warmest in the winter [She and von

Zahn, 1998], which suggests that it is not the solar flux, but rather dynamical or chemical processes that drive this region's heating budget [She *et. al.*, 1995]. The dynamical energy sources in the mesopause region include atmospheric tides, which are waves excited by solar heating and propagate through the atmosphere with periods equal to the subharmonic of one solar day, and atmospheric gravity waves, which are typically excited near the earth surface by convection, orographic perturbation, and thunder storms [Fritts, 2003]. They propagate upward through the atmosphere with increasing amplitude. The signatures of such waves have been observed in the lidar profiles of sodium density [Batista *et. al.*, 1985] temperature [She *et. al.*, 2002] and wind velocity [Yu et al., 1997].

The winds in the mesopause can be treated separately according to the direction of their velocities. Vertical wind speed is pretty small, usually about a few centimeters per second. In horizontal plane, zonal wind is east or westward, and sometimes can be over 100m/s [Sherman et al., 2003]; meridional wind travels north or southward, whose multi-day mean is smaller than that of zonal wind. Both zonal and meridional winds have strong seasonal dependence, and show considerably different daytime and nighttime behaviors due to solar thermal tidal effects. Their interrogations are among the topics dealt with in this thesis.

There are varieties of chemical species in the altitude around the mesopause, including atomic metals: sodium, potassium, calcium, and iron. For sodium atoms in this region over Fort Collins, CO (105° W, 40.5° N), during the summer, it goes to its minimum about 10^{8} m^{-3}, and reaches its maximum about 10^{9} m^{-3} in the early winter. Although the sodium peak density is around 92km most of the time, the sodium layer is very active in the mesopause region, and multiple sodium layers are often observed. The sporadic

sodium layer, with FWHM about 1-2 km (sometimes it is just a few of hundred meters), and typically lasting tens of minutes or even hours (Fig 1-2), is one of the most interesting phenomena, which has drawn increasing attention from atmospheric scientists all around the world.

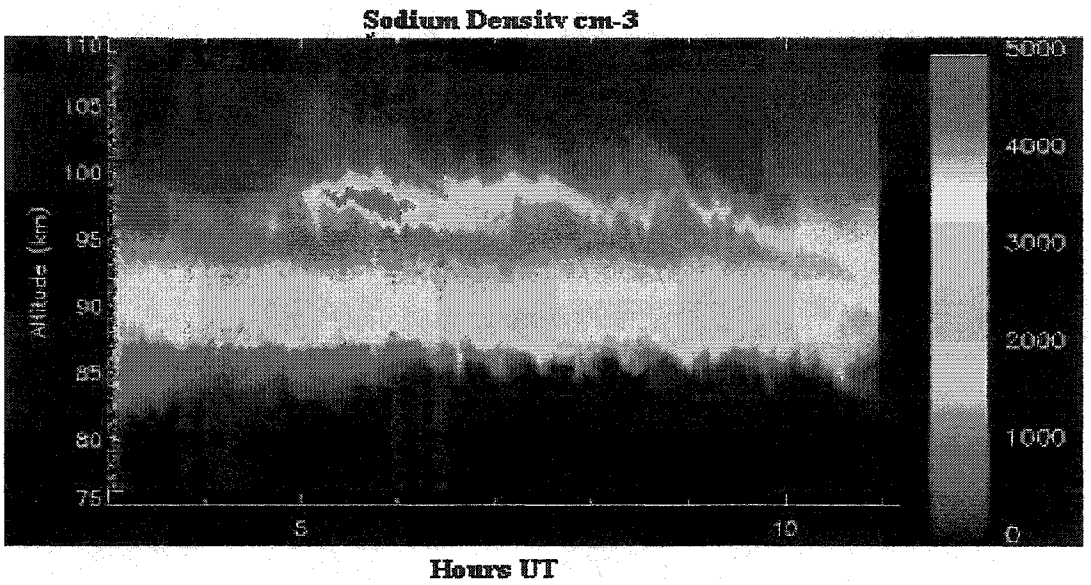

Fig. 1-2 Sporadic sodium layer observed on night UTday 3187, July 6th, 2003

The plot above shows a sporadic sodium layer event from July 6th, 2003. The typical sodium layer peak is at around 90-93km. In this event, the sporadic sodium layer's peak density was at around 98-99km, which is way above the normal layer (at 90km). Also, it was about double the normal sodium peak density and lasted about 5 hours. Sporadic Na layer events mostly happen during the summer season above Fort Collins. The theory behind this sporadic event is yet clearly understood, but there are many discussions [Clemesha, 1996; Kane, 2001]. Its accompany with sporadic E layer (metallic ion layer in the ionosphere E region) tells us it may be the result of ion neutralization that is related to

the electronic field bending or wind shear mechanism in the lower thermosphere, which pushing the Na^+ down.

1-3 CSU Lidar History and Thesis structure

Colorado State University lidar group in Fort Collins, Colorado (40.5°N, 105°W) started with Rayleigh lidar in the mid 1980's. In 1989, in collaboration with scientists from the University of Illinois, CSU's first Na resonance lidar observation of mesopause region temperature was made on August 1989 [She *et al.*, 1990]. From then on, routine data collection and system development have been carried out for over fourteen years. At the beginning, the CSU Na-lidar was operating at two-frequencies (D_{2a} and crossover) to measure sodium density and temperature. Then, in 1994, a third frequency was introduced by Yu [1994], using an acoustic-optic modulator for mesopause wind measurement [She and Yu, 1994]. A couple of years later, in 1996, a custom acoustic-optic modulator system with two AO modulator and double pass was incorporated into the lidar for 3-frequency simultaneous line-of-sight wind, temperature and Na density observation. Shortly after that, the construction and integration of a Faraday anomalous dispersion filter, which was used for daytime operation, were achieved by H. Chen (1997), along with the first 24-hour monitoring of temperature and density detection above Fort Collins [Chen *et. al.*, 1996]. In 1999, a vertical wind bias was noticed and a frequency monitor based on iodine absorption spectroscopy was successfully added to the lidar transmitter, and the frequency of the output laser pulses could be accurately monitored for diagnostics and for correction of the observed wind velocity [White, 1999]. The Faraday filter facilitated 24-hour continuous temperature measurements between

1997 and 1999 [Chen et al., 2000]. This was followed by simultaneous measurements of temperature and line-of-sight wind off and on in 2000 and 2001, though the stability was not good or robust enough for long-period wind measurements. Another milestone of the CSU Na-lidar came in the early 2002, when it was used to measure zonal and meridional winds, and temperature, and Na density simultaneously by pointing two laser beams: one 30° from zenith to the east and the other 30° from zenith to the north [Sherman, 2002]. At almost the same time, big improvement in the robustness of Faraday filter occurred as the method to independent by control the temperature and pressure of the Na cell was introduced. This makes it very stable for long-period daytime simultaneous observation of temperature, and horizontal wind (both zonal and meridional); considerable data on simultaneous temperature, zonal and meridional winds have now been acquired by the CSU Na-lidar and they are deposited in the community CEDAR database. Since then (May 2002), observations over complete diurnal cycle, which is necessary for investigation of atmospheric solar thermal tides, has been running as campaign mode for some 20 months. There have been hundreds hours of data with complete diurnal cycle observation, with the longest continuous campaign thus far over 200 hours, achieved from September 21st to 29th in 2003.

The CSU lidar program, under the guidance of Professors She and Krueger, has been providing data profiles for about fourteen years, and achieved a great deal. The focus of this dissertation is on the full diurnal cycle campaigns and the data acquired will be used for study of solar thermal tides. Some key instruments and the associated theory of the measurement are also outlined here for comprehensive understanding of measurement technique and error bar.

Chapter 2 outlines the basic physical processes involved in laser-induced fluorescence of sodium at 589nm, and the theory of Na-lidar operation: how the thermal broadening and Doppler shift contribute to the measurement of temperature and winds.

Chapter 3 introduces the design of the 3-frequency Na-lidar system and the related background knowledge of fundamental physics. Since the Faraday Filter is the key instrument of the diurnal cycle observation, its relevant theory will be discussed in more detail. It involved significant amount of hard work, and the reward is very appreciable.

Chapter 4 first shows the CSU Na-lidar data-processing algorithm, and then shifts to the tidal analysis using the full diurnal cycle data. Tidal signatures are revealed and studied, including year-to-year variation. Monthly mean temperature and winds (zonal and meridional wind), based on complete diurnal cycle campaign are presented and compared with model.

Chapter 5 gives some introduction of solar thermal tides and classical tidal theory. The most recent theoretical models, including GSWM (Global Scale Wave Model), TIME-GCM (Thermosphere Ionosphere Mesosphere Electrodynamic General Circulation Model) are briefly discussed as well.

Chapter 6 presents the comparison between CSU Na-Lidar diurnal and semidiurnal tidal-period oscillation and GSWM and TIME-GCM respectively. Discussion and summary are also presented at the end of every chapter.

Chapter 7 presents the conclusion and some future improvement of this lidar system.

Reference:

Batista, P. P., B. R. Clemesha, D. M. Simonich and V. W. J. H. Kirchhoff, Tidal oscillations in the Atmospheric Sodium Layer, *J. Geophys. Res., 90,* 3881-3888. 1985.

Chen, H., M. A. White, D. A. Krueger and C. Y. She, Daytime mesopause temperature measurements using a sodium-vapor dispersive Faraday filter in lidar receiver. *Opt. Lett. 21,* 1003-1005, 1996.

Clemesha, B. R., P. P. Batista and D. M. Simonich, Formation of sporadic sodium layers, *J. Geophys. Res., 101,* 19701-19706, 1996.

Hauchecorne, A and Chanin, M. L., *Geophys. Res. Lett.*7, 565-568 1980.

Kane, T., B. Grime, S. Franke, E. Kudeki, J.Urbina, M. Kelley, and S. Collins, Joint Observations of Sodium Enhancements and Field-Aligned Ionospheric Irregulatities, *Geophys. Res. Lett.*, 28(7), 1375-1378, 2001.

She, C. Y. Remote Measurement of Atmospheric Parameters: New Applications of Physics With Lasers. *Invited Paper, Contemp. Phys.* 31, 247-260 1990.

She, C. Y., H. Latifi, J. R. Yu, R. J. Alvarez II, R. E. Bills, and C.S. Gardner, Two-Frequency Lidar Technique for Mesospheric Na Temperature Measurements *Geophys. Res. Lett.* 17, 929-932 1990.

She, C. Y., J. R. Yu, and H. Chen, Observed thermal structure of a midlatitude mesopause, *Geophys. Res. Lett.* 20, 567-570 1993.

She, C. Y., and J. R. Yu, Simultaneous three-frequency Na lidar measurements of radial wind and temperature in the mesopause region, *Geophys. Res. Lett.*, 21, 1771-1774, 1994.

She, C. Y., J. R. Yu, D. A. Krueger, R. Roble, P. Keckhut, A. Hauchecorne, and M. L. Chanin, Vertical structure of the mid-latitude temperature from stratosphere to mesopause (30 - 105 km), *Geophys. Res. Lett.*, 22, 377-380, 1995.

Thomas, G. E., Is the polar mesosphere the miner's canary of global change? *Adv. Space Res.* 18(3), 149, 1996.

White, M. A. PhD dissertation: A Frequency-agile Na Lidar for the Measurement of Temperature and Velocity in the Mesopause Region, Colorado State University, 1999.

Chapter 2 Basic Theory of Na-Lidar

As mentioned earlier in chapter 1, metallic elements, like sodium, are deposited in the mesopause region by meteors disintegrating as they enter the atmosphere. This forms an atomic element layer. Among these metallic elements layers, atmospheric sodium is the most widely used of the alkali metal layers in the atmosphere for lidar measurements because it is relatively abundant, larger cross section and the required transmitter frequency is easy to generate. Another alkali metal lidar is potassium lidar [von Zahn, 1996]. Sodium exists in its ionized form, and it exists as chemical compounds (such as sodium oxide) below this layer.

The CSU sodium lidar takes advantage of the atomic sodium in this region by transmitting laser pulses of precise frequencies and analyzing the signal scattered by the sodium atoms through laser-induced fluorescence (LIF). Each laser pulse, transmitted through the atmosphere, has an energy of about 20mJ, which corresponds to roughly 5×10^{16} photons. The number of return photons, collected by a 35cm diameter telescope, is about 50 for each shot (with the future replacement of 70cm diameter telescope, the number of return photons collected could be 4 times larger). It looks like a huge loss, but it repeats 50 times per second and the photon counting process employed is free from electronic noise, so very useful data can be collected within a few minutes. Based on the assessment of the backscattered sodium spectra's thermal broadening and Doppler shifting, the height-dependent kinetic temperature and radial wind velocity of the sodium atoms (and therefore the surrounding air) are obtained.

To understand how the Na fluorescence lidar in Colorado State University detects mesopause parameters (like temperature and wind), the fluorescence spectrum of sodium must studied first, along with its temperature and velocity dependence. Since many of the quantum-mechanical details of sodium excitation have been studied and presented before, both in the general literature (e.g. Corney, 1977) and in dissertations and papers of previous developers in the CSU lidar group [J. Yu, 1995; H. Chen, 1996; S. Chen, 1999 and M. White, 1999], this chapter will focus only on quantities and concepts necessary to understand and reproduce the 3-frequency lidar measurement.

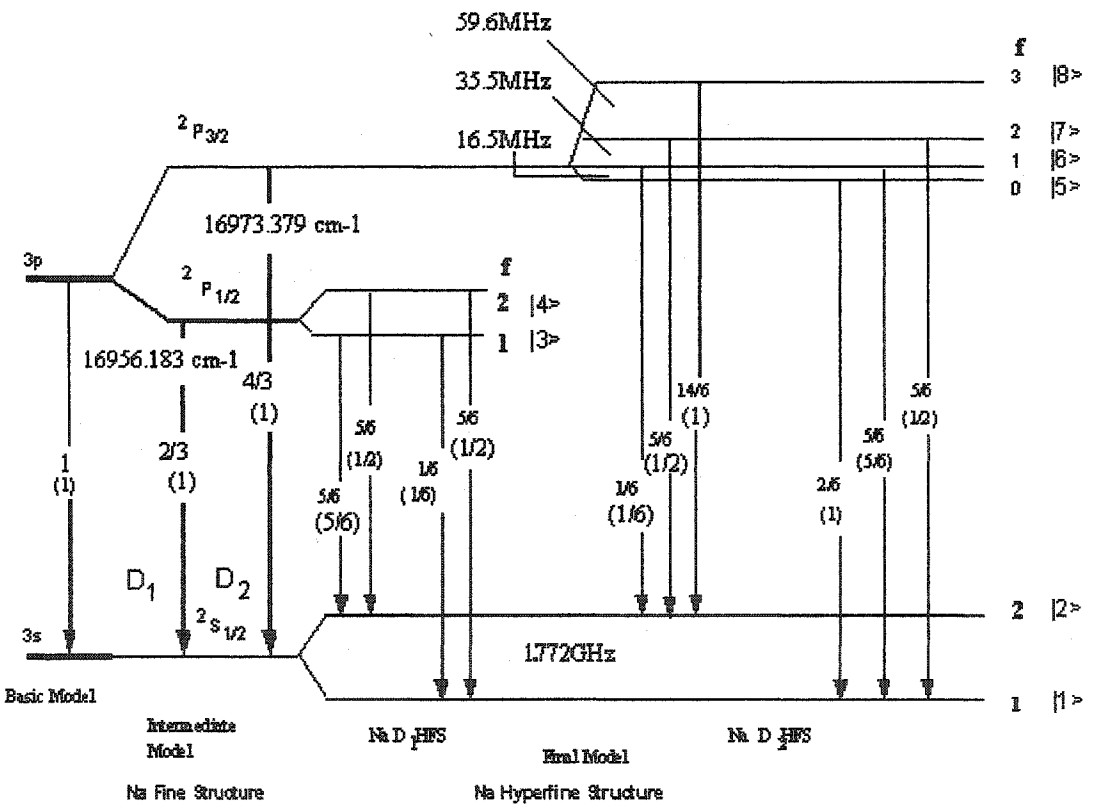

Fig 2-1 Sodium D Transitions (energies are not to scale)

The spectroscopic region of primary interest to the operation of 3-frequency Na lidar is in the vicinity of D_2 electric dipole transition near 589nm (Fig 2-1). From D_2 transition,

hyperfine splitting separates the D_{2a} and D_{2b} groups, each associated with one of the two lower energy levels in the D_2 transition ($3S^2_{1/2}$), and each allowing excitation to three of the four upper energy levels ($3P^2_{3/2}$).

As shown in Fig 2-1, the D_2 transition actually consists of six discrete resonance lines, though the spectrum is continuous due to various line-broadening mechanisms. The numbers with the bracket of each transition represent the relative linestrengths. The energy difference of each excited state of the D2 transition is also written down in the figure [Steel and McFarlane, 1983]. Among these broadening mechanisms, lifetime broadening is about 10MHz (full-width-half-maximum is given by $1/2\pi\tau$, where τ is the lifetime of the excited state), which comes from the finite lifetime of the excited state (in the case of Na, $\tau = 16.4ns$). Another source is collisional broadening. However, because of the low pressure in the mesopause (typically less than 0.01mbar), its contribution is negligible to the overall line width of atmospheric Na atoms [Yu, 1995]. The most significant broadening here for the sodium spectroscopy is Doppler broadening, which arises from the thermal velocity of the sodium atoms. For sodium at 200K, which is typical in the mesopause region, the Doppler width is about 1GHz, making Doppler broadening the dominant source of the transition linewidths of the atmospheric sodium.

With the random thermal motion of atoms, those atoms traveling towards the detector with the velocity V will have transition frequencies that differ from those of atoms at rest by the Doppler shift. The atoms' distribution of velocities can be found from the Maxwell-Boltzmann distribution. For a gas at temperature T, the number of atoms with line-of-sight velocity between V and $V+dV$ is given by:

$$n(V)dV = N\sqrt{\frac{m_0}{2\pi k_B T}}e^{-m_0 V^2/2k_B T}\,dV$$

N = total number of atoms

m_0 = atomic mass

k_B = Boltzmann's constant (2-1)

Since the thermal velocities are non-relativistic, the Doppler shift in the transition frequency for atoms moving at a velocity V is given by the simple form

$$\nu = \nu_0\left(1 \pm \frac{V}{c}\right) \tag{2-2}$$

where ν_0 is the transition frequency relative to an atom at rest, and c is the speed of light in vacuum. Substituting (2-2) into (2-1) gives

$$I(\nu) = I_0 \exp\left[\frac{-m_0 c^2(\nu_0 - \nu)^2}{2k_B T \nu_0^2}\right] \tag{2-3}$$

This is a Gaussian line shape with the center frequency at ν_0, and the full width at half-maximum is given by

$$\Delta\nu_{Doppler} = \frac{2\nu_0}{c}\sqrt{\frac{2k_B T}{m_0}\ln 2} \tag{2-4}$$

Clearly, as the temperature goes up, the Doppler broadening increases.

However, the atmospheric atoms are not only in the thermal motion, in which the center of mass of the volume of gas remains fixed, but are also being carried with the wind speed in the mesopause. Thus, they exhibit collective motion. The effect of such motion is not line broadening, since the motion does not belong to any instantaneous distribution of random velocities, but rather an overall Doppler shift of the Gaussian transition lineshapes. The frequency shift for a given collective velocity V_{wind} is:

$$\Delta \nu = \pm \frac{V_{wind}}{\lambda_0} \tag{2-5}$$

The sign depends on the whether this wind is blowing towards the laser + or away - from it, and the λ_0 is the vacuum wavelength for the atom at rest.

So, the atmospheric sodium fluorescence spectrum must include the thermal broadening and Doppler-shift together, and it is given by

$$g(\nu, T, V_{wind}) = \left(\frac{D}{\pi T}\right)^{1/2} \exp\left(\frac{-D(\nu - \nu_0 - V_{wind}/\lambda_0)^2}{T}\right) \tag{2-6}$$

where $D = m\lambda_0/2k_B = 497.6165K\ (ns)^2$ for sodium atoms with λ_0 = 589.2nm, and $g(\nu, T, V)$ is the probability distribution in frequencies[Sherman 2002]. V_{wind} is positive for line-of-sight winds toward the laser.

As mentioned earlier, the sodium D_2 transition consists of six lines, and each and every transition must be considered, giving the final sodium D_2 lineshape shown below [She et. al., 1992].

$$g_{Na}(\nu,T,V_{wind})=\left(\frac{D}{\pi T}\right)^{1/2}\sum_{n=1}^{6}A_n\exp\left(\frac{-D(\nu-\nu_n-V_{wind}/\lambda_n)^2}{T}\right) \quad (2\text{-}7)$$

where the coefficients A_n are the relative linestrengths (Einstein coefficients from every energy levels of $3P^2_{3/2}$ to $3S^2_{1/2}$ states. See Fig. 2-1) of the hyperfine transitions, and the sodium D_2 transition fluorescence spectrum is shown below.

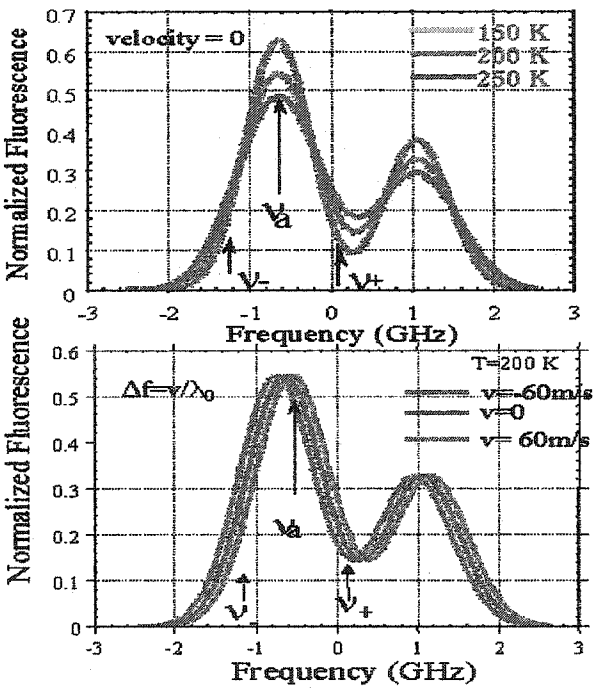

Fig 2-2.

(a) Sodium atom D_2 transition fluorescence spectrum at different temperaturess (175K, 190K, 210K, and 450K), illustrating the effect of thermal broadening.

(b) Sodium atom D_2 transition fluorescence spectrum at different wind speeds, illustrating the effect of Doppler shifting. Also shown are the three transmitting frequencies of the CSU sodium lidar, ν_-,ν_a, and ν_+.

Fig (2-2) shows the spectrum changes (broadening and shift) due to temperature and wind velocity. From this graph, it is clear that certain frequencies in the fluorescence spectrum are more sensitive to the change in the sodium temperature than others, and certain frequencies are more sensitive to a collective velocity than others. In the case of no collective velocity (a), it is possible to determine the temperature of a given spectrum by comparing the relative fluorescence at each transmitting frequency in the LIF (laser induced fluorescence) spectrum. For example, as the temperature increases the line

becomes broader and the fluorescence of the two off-peak frequencies increases compared to that at the peak frequency. Similarly, in the case of constant temperature (b), it is possible to determine the collective velocity of a given spectrum by comparing the relative fluorescence at, for example, the right and left wings of the left peak. When there is a frequency shift due to atmospheric wind, the florescence of one of the off-peak frequencies increases while the other off-peak one decreases (again, compared to the peak frequency), depending on the wind direction. Of course different frequencies have different sensitivities to the variations of temperature and velocity. The frequencies, which yield the highest sensitivity to temperature, do not necessarily have good sensitivity to velocity. So properly choosing the operation frequencies is necessary for the lidar mesopause observation.

Two ratios will be generated from the different combinations of the same three fluorescence response levels, and it is necessary that both the temperature and velocity information be derivable from just these three values. However, each ratio should not be very sensitive to both temperature and wind to minimize the interdependence of the measurements. Fortunately, the response to a change in temperature is nearly symmetric about the D_{2a} peak, while the response to velocity has an opposite sign on each side of D_{2a} peak. So, by sampling three points from the fluorescence spectrum, it is possible to determine both the temperature and the radial wind velocity corresponding to a given spectrum. This is the basic idea of the 3-frequency lidar measurement. Also, for reasons inherent to the 3-freqency lidar, its frequency locking system, and frequency-shifter--AOM (Acoustic-Optic Modulator) design, the choice of operating frequencies is limited

to include the Doppler-Free D_{2a} peak, and any equal amount of shift up or down from the D_{2a} peak. That is: ν_{D2a} and $\nu_{D2a} \pm \Delta\nu_{shift}$.

From the analysis conducted by Papen et al. [1995], an optimum shift frequency of 630MHz was determined, finalizing the lidar's three relative operating frequencies at $\nu_a \equiv$ 0MHz for the D_{2a} peak frequency (corresponding to a laser wavelength around 589.16nm), ν_+ = 630MHz, and ν_- = -630MHz. The pulsed laser beams, which are amplified by PDA (Pulse Dye Amplifier) and transmitted by the lidar, are intended to be centered at these frequencies sequentially.

Then, two ratios for the temperature and wind measurement are generated based on the discussion above.

$$R_{temp} = \frac{g_{Na}(\nu_+,T,V)+g_{Na}(\nu_-,T,V)}{2g_{Na}(\nu_a,T,V)}$$

$$R_{wind} = \frac{g_{Na}(\nu_+,T,V)-g_{Na}(\nu_-,T,V)}{g_{Na}(\nu_a,T,V)} \qquad (2\text{-}8)$$

where ν_+, ν_- and ν_a are the three operating laser frequencies. R_{temp} and R_{wind} are relatively more sensitive to temperature and collective velocity, respectively. By using the sodium fluorescence spectrum, along with the measured pulsed laser lineshape, which is discussed in Chapter 4, high accuracy numerical calibration can be achieved, which yields a high-resolution 2-dimensional calibration curve, and thus, any measured pair of R_{temp} and R_{wind} may be converted into an equivalent temperature and radial velocity pair (Fig2-3). For daytime data analysis, the Faraday Filter transmission lineshape, also taken

by experimental measurement, has to be included in the numerical calibration also. It gives another 2-dimensional calibration curve. The detailed numerical calculations and data-processing algorithm will be presented in Chapter 4 of this dissertation.

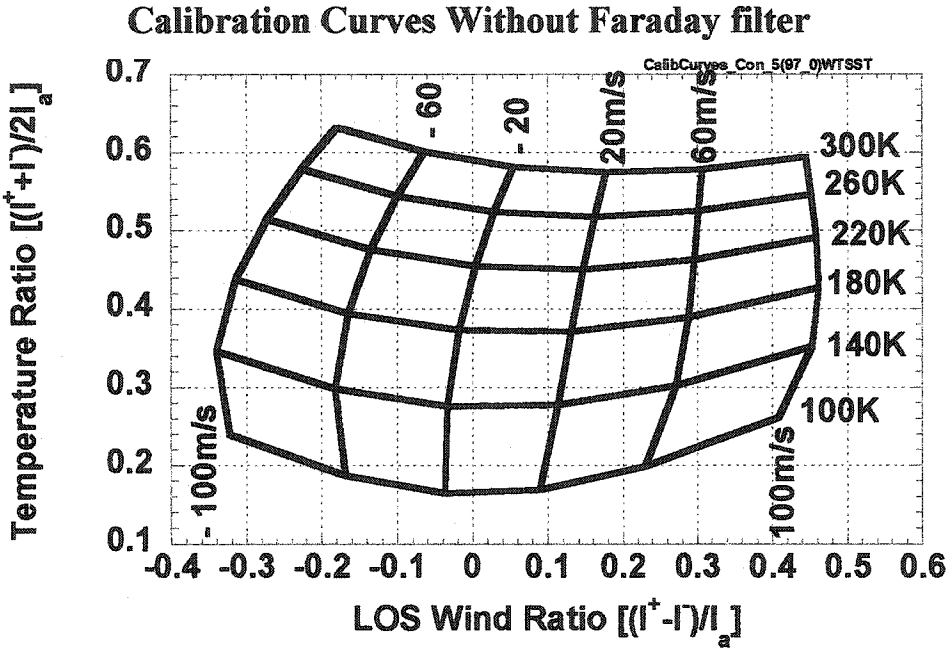

Fig 2-3 The 2-dimensional field of calibration curves for mapping points of known ratios (R_{temp}, R_{wind}) into temperature and radial wind velocity. The curves arise from theoretical spectra of sodium fluorescence.

The current CSU lidar system (with 35cm telescope) can resolve a wind speed of a few meters per second with 1km height and 15 minutes temporal resolution for nighttime observation. Without hardware improvements, better spatial resolution requires sacrificing temporal resolution. Resolution during daytime measurement is not as good as that during the nighttime due to sky background and the use of a Faraday Filter, which will be discussed in Chapter 3.

Reference:

Chen, S., PhD dissertation: Sodium/Potassium Faraday Filter for daytime Lidar Temperature Observations and Study of tidal Waves in the Mesopause region of the Atmosphere, Colorado State University. 1999.

Chen, H., C. Y. She and Eric Korevaar, "Na Vapor Dispersive Faraday Filter", *Opt. Lett. 18*, 1019-1021 (1993).

Chen, H., M. A. White, D. A. Krueger et al., Daytime mesopause temperature measurements using a sodium-vapor dispersive Faraday filter in lidar receive. *Opt. Lett. 21*, 1003-1005, 1996.

Corney, A., Atomic and Laser Spectroscopy, Chapter 4 (Oxford: Clarendon Press, Oxford, 1977).

Papen, G.C., C.S. Gardner, and W.M. Pfenninger, Analysis of a potassium lidar system for upper-atmospheric wind-temperature measurements, *Appl. Optics, 34 (30)*, 6950–6958, 1995.

She, C. Y., and J. R. Yu, Simultaneous three-frequency Na lidar measurements of radial wind and temperature in the mesopause region, *Geophys. Res. Lett., 21*, 1771-1774, 1994.

She, C. Y., J. R. Yu, H. Latifi, and R. E. Bills, High-Spectral-Resolution Fluorescence Lidar for Mesopheric Sodium Temperature Measurements, *Appl. Opt. 31*, 2095-2106, 1992.

Sherman, J., PhD dissertation: Mesopause Region Thermal and Dynamical Studies Based on Simultaneous Temperature, Zonal and Meridional Wind Measurements with Upgraded Sodium Fluorescence Lidar. Colorado State University, 2002.

von Zahn, U., J. Höffner, Mesopause temperature profiling by potassium lidar, *Geophys. Res. Lett., 23(2), 141-144*, 1996.

Steel, D. G. and R. A. McFarlane, Collisional destruction of four-wave-mixing signals in sodium in the presence of low-pressure buffer gas, *Phy. Rev. A, Vol. 27, No. 3, 1983.*

White, M. A., PhD dissertation: A Frequency-agile sodium Lidar for the Measurement of Temperature and Velocity in the Mesopause Region, Colorado State University. 1999.

Yu, J. R. and She, C. Y., Climatology of a mid-latitude mesopause region observed by a lidar at Ft. Collins, CO (40.6°N, 105°W), *J. Geophys. Res.*, 100, 7441-7452, 1995.

Yu, Jirong, PhD dissertation: A sodium wind/temperature lidar and observed mesopause thermal structure over Ft. Collins, CO, Colorado State University 1994.

Chapter 3 CSU Na-Lidar System

In this chapter, we describe the basic hardware required for the CSU Na-lidar. Like most other lidar systems, sodium resonance florescence lidar in Colorado State University can be separated into transmitter and receiver. The transmitter, which consists of four lasers and AO frequency modulator and precision frequency control system, generates laser pulses and directs them into the atmosphere. The receiver collects and processes the scattered laser light and then directs it onto a photodetector. It includes a pair of telescopes, each aligned with the one of the two laser beams, PMTs (photo-multiplier tube), Faraday filters (for daytime use only) and photon counting electronics.

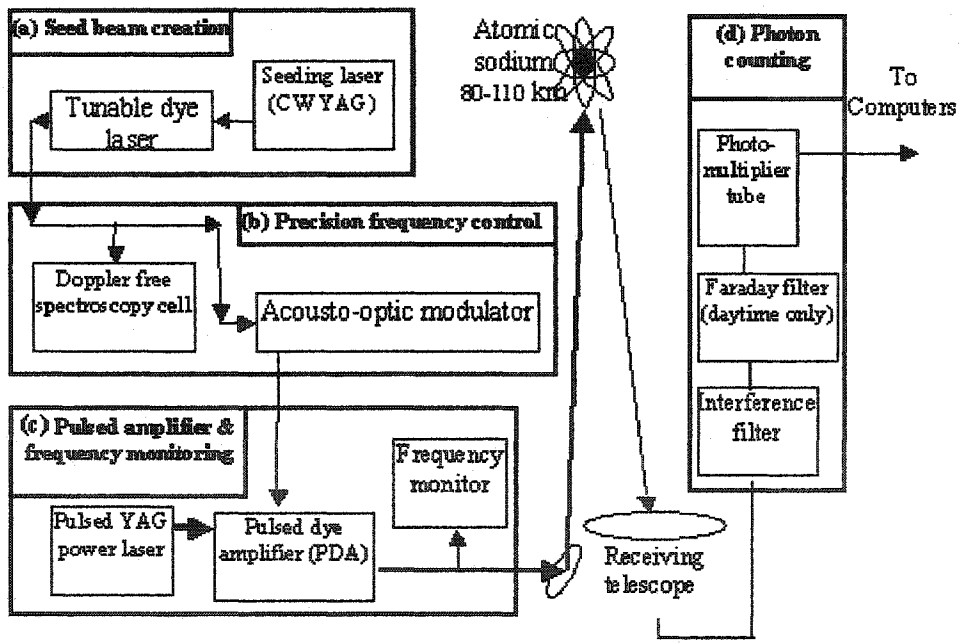

Fig. 3-1 Schematic diagram with major components of the Colorado State University sodium lidar, including (a) beam creation, (b) precision frequency control, (c) pulsed amplification, transmission, and frequency monitoring, and (d) receiving system for photon counting. The arrows indicated the path the light takes through the system. From Arnold and She 2003.

3-1 Transmitter

The transmitter of Na temperature-wind lidar consists of three laser systems, one pulsed dye amplifier, an acoustooptic frequency shifter and a Doppler-free spectrometer for absolute frequency determination and control. Each of these units is described below.

3-1 a The single-mode tunable ring dye laser for initiating CW seed beam

The heart of the transmitter system is the Ring Dye laser (Coherent Model-899 from Coherent Inc.), which is pumped by the Spectra Physics made Millennia-V CW YAG laser, operating at 532nm. Working as the seed beam of the Lidar transmitter and depending on the pump power, the Ring Dye laser can provide over 450mw (with the CW YAG pump power of 4.0W) of widely tunable (>20GHz), narrow band (< 1MHz) output.

During the data acquisition, the Ring Dye laser is actively locked to the deepest Doppler-free (Lamb-dip) structure of the D_{2a} transition at ~589.16nm. The Doppler-free structure will be discussed later.

3-1.b. Acoustic optical modulator for seed frequency shifting

Following the CW seed beam, the laser beam goes through the collimating optics and into the Acoustic Optic (AO) Modulator (see Fig. 3-2) and its frequency may be shifted by ±630MHz on command. The AO unit consists of, in order, a polarizing beam splitter, imaging lenses with each AO crystal located at one of the two image positions, a quarter wave plate, and a back mirror to achieve double-pass frequency shifting by either AO crystal so that the laser beam at each of the three frequencies (unshifted and shifted by ±

630MHz) propagates along the same direction as it comes out of the unit (Fig. 3-2 c) to seed the pulsed dye amplifier (PDA).

The basic theory for the operation of the AO unit is Bragg Diffraction theory. One simple way to explain the interaction and to determine the parameters of the diffracted beam in terms of those of the incident beam and the sound wave is to use the particle picture and treat the traveling sound wave as a series of acoustic phonons with momentum $p_s=\hbar k_s$. These phonons interact with the incident laser photons with momentum $p_i=\hbar k_i$. Depending on the interaction cross-section, an incident photon and a traveling wave phonon will be converted into a diffracted photon with the final wave vector $\boldsymbol{k}_f = \boldsymbol{k}_s + \boldsymbol{k}_i$, and the final frequency $\nu_f = \nu_s + \nu_i$, by conservation of energy and momentum. Since $\nu_s << \nu_i$, $|\boldsymbol{k}_f| \approx |\boldsymbol{k}_i|$, the vector addition forms an isosceles triangle with $\boldsymbol{k}_s$ as the base (Fig. 3-2 a, b). The diffraction angle is then given as: $\sin\theta = \lambda_i/2\lambda_s$ by the well-known first-order Bragg diffraction. By specific design, the incident beam and diffracted beam can overlap and interact for a substantial length, the higher order Bragg scattering are suppressed and 80% single path efficiency (60% for double path) is easily achieves for this AO unit.

There is another key part inside this AO unit. It is a mechanical chopper wheel placed in front of the back mirror, which selects the beam (shifted or unshifted) that is allowed to travel through the AO system, and into the PDA. Also, this chopper provides the command for synchronization, to switch microwave power on and off the AO crystals and to trigger the pulsed YAG laser at the precise moments through associated custom logic circuit.

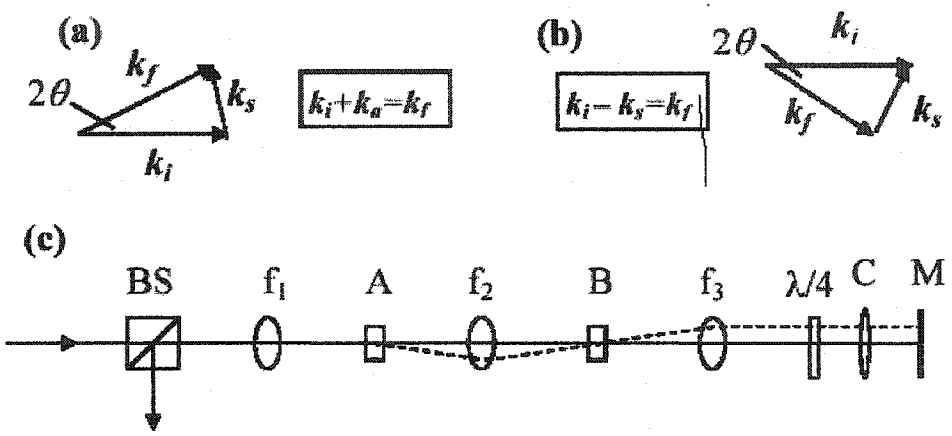

Fig 3-2 A diagram for vector addition of the incident photon (k_i), phonon (k_s), and the final photon (k_f) of a (a) frequency raising and (b) frequency lowering acousto-optic interaction. k_s is exaggerated in this diagram. (c) A schematic diagram of the tandem acousto-optic modulator unit used by the CSU sodium lidar. **From Arnold and She, 2003**

3-1. c. Doppler-free spectroscopy for absolute frequency monitor

At the same time, a small fraction of seed beam, which is partially reflected by the beam splitter in the AO system, is sent into the Doppler-Free Spectroscopy unit to monitor the frequency of the seed beam (see Fig. 3-3). This Doppler-Free Spectrum subsystem mainly consists of a sodium cell heated at 70°C and a PMT at a right angle to the interrogating laser beam to collect the fluorescence signal.

The sample laser light goes through the sodium cell and gets reflected by a mirror at the other side of the cell to reflect it back along the same path as it goes into the cell. These two counter propagating sample beams interact with the sodium atoms in the cell to generate the Doppler-free saturation spectrum containing sharp features, which can be used in a feedback loop to control the output frequency of the laser and to lock the seed

laser at the desired D_{2a} frequency. The physics behind the Doppler-free spectrum will be discussed below.

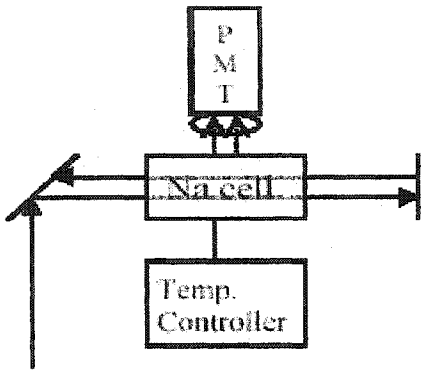

Fig. 3-3 Schematic diagram of Doppler free saturation spectroscopy experiment. The laser beam of tunable frequency ν enters from the left, transmits through the cell, is reflected by the mirror, and transmits through the cell in the other direction. A PMT (photo-multiplier tube) is placed to the side of the cell to measure laser -induced fluorescence. In front of the PMT is a lens to gather a larger signal. From Arnold and She, 2003.

In CSU's lidar lab, the sodium cell is heated to 70°C to provide a healthy vapor density, and the absorption spectrum of Na can be easily detected. But this spectrum, with a FWHM of about 1.4GHz is too broad to be used as a frequency marker with MHz accuracy to lock the laser. To get the Doppler-free saturation spectrum, the power of the sample beam must be large enough to induce the fluorescence saturation, but low enough to avoid power broadening of the natural line-width and the saturation of the PMT. We typically use ~150μW of power for the sample beam. The beam path in this subsystem must also be carefully aligned to get the two counter propagating beams mentioned earlier. Only then, the Doppler-Free saturation spectrum of sodium can be achieved with the sharp features. This Doppler-free spectrum actually provides three features that offer the possibility for laser locking (Fig 3-4a): D_{2a}, D_{2b} transitions and crossover. Among them, the deepest narrow (about 40MHz) "Lamb dip" spectral feature at the frequency located at D_{2a} transition is chosen to be the locking position. With the help of this Doppler-free subsystem, we can lock the laser to within 2MHz for lidar operation.

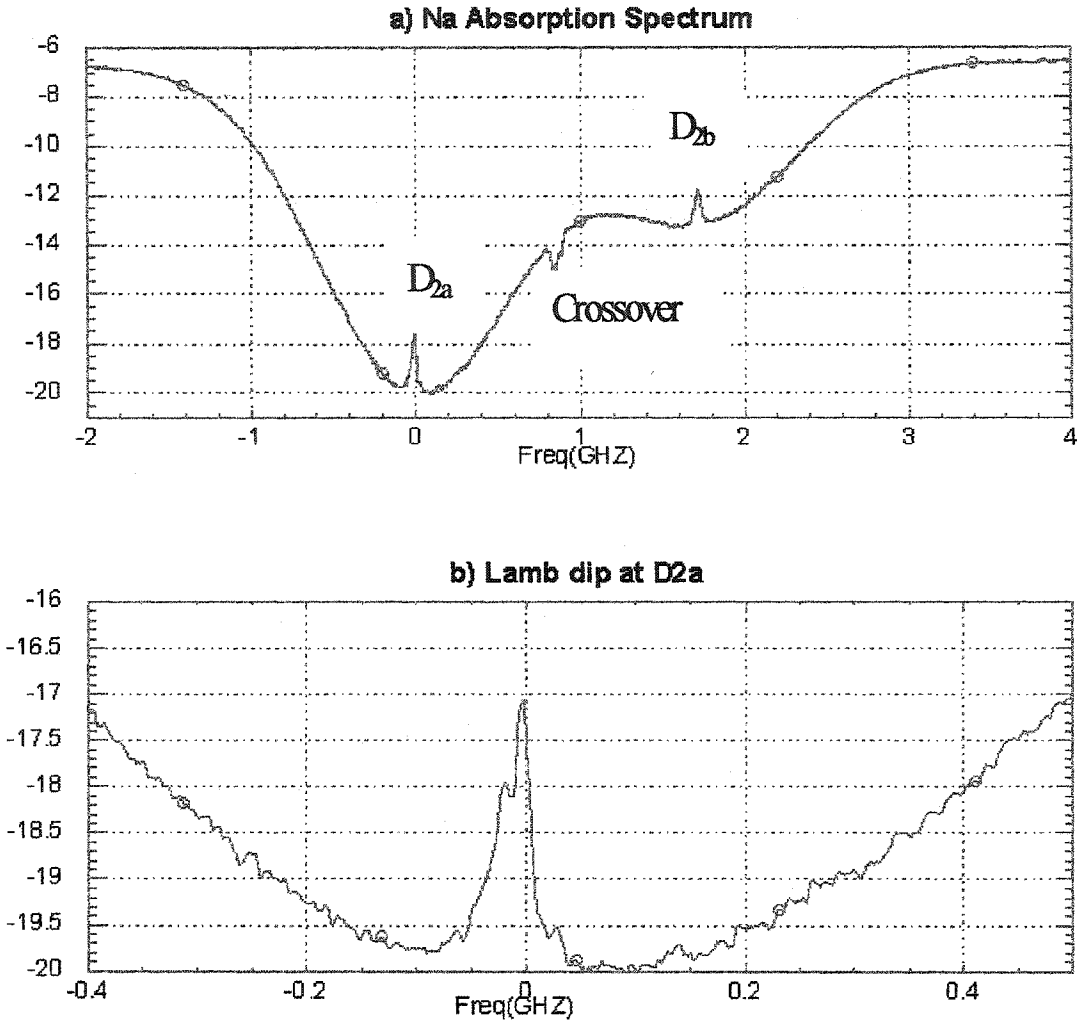

Fig3-4 Doppler -Free Spectrum, D2a Lamb dip used for CW Seed beam locking

The measured inverse Doppler-Free spectrum containing all 3 Doppler-free features, and the Lamb dip at the D_{2a} transition at a higher resolution are shown, respectively, in Fig. 3-4a and Fig. 3-4b. If we look at the Lamp dip at D_{2a}, we can see that there are actually two strong peaks about 16MHz apart. The location of the active locking of the Ring Dye laser is at the highest peak, designated as the D_{2a} frequency at –651.4MHz relative to the center of mass of the Na D_2 transition [She and Yu, 1995].

It is necessary to discuss the Lamp dip a little bit more. First, in thermal equilibrium for temperature T, the probability of finding an atom moving at the velocity between V_z and $V_z + dV_z$ along the sample beam direction, z, is given by Maxwell- Boltzmann velocity distribution:

$$p(V_z)dV_z = \left(\frac{m}{2\pi k_B T}\right)^{1/2} e^{-mV_z^2/2k_B T} dV_z \qquad (3\text{-}1)$$

Consider a two-level system with the energy difference $h\nu_0$, and a laser beam traverse from one side of the cell with frequency ν. The laser beam will only interact with the group of atoms with specific velocity so that the atom sees the laser at $\nu_{ap} = \nu_0$. According to the Doppler effect.

$$\nu_{ap} = \left(1 - \frac{V_z}{c}\right)\nu_o \qquad (3\text{-}2)$$

As, the laser intensity increase, LIF (Laser Induced Fluorescence) increases as well, but less than linearly. This saturation arises because the ground state population is reduced as the laser intensity increases, and more excitation occurs. Since we set up a back reflection mirror in the Doppler-Free unit, the incident laser beam actually travels in two opposite direction, so it interacts with two groups of atoms, which are opposite propagating, to generate LIF (laser induced fluorescence). That is: if the frequency $\nu < \nu_0$, the beam propagating from the left will interact with the atoms moving to the left, and the beam propagating from the right will catch the atoms moving to the right. For frequency $\nu > \nu_0$, it goes to the opposite. As long as the laser frequency is not equal to ν_0, the two opposite propagating laser beams interact with separate groups of atoms, and the LIF intensity is

doubled that with only one direction beam. However, if the laser frequency is right at ν_0, the two opposite traveling beams will interact with the same group of atoms with velocity $V_z = 0$. Then, the ground state population reduction gets doubled, causing the intensity of LIF at ν_0 to decrease (or enhance saturation). This dip at ν_0 in the spectrum is called a Lamb dip.

Since the Na atom has two ground levels, two Lamb dips (D_{2a} & D_{2b}) occur, both of which can clearly be seen in Fig 3-4a. The other interesting special feature in the Na Doppler-Free spectrum is the Crossover spike. This is due to the optical pump effect. Because of this effect, there is a reduction of the LIF from that of a two-level system. The atoms in one of the ground state after the fluorescing temporarily cannot return to the original ground level, thus is out of the original loop of interaction with laser beam. However, the atoms pumped out of the original interaction circuit automatically join in another group of atoms to interact with the laser beam traveling in the opposite direction, if the laser frequency is at the middle to transitions from the same upper state to the two ground stated, i.e., at this crossover frequency ν_c; the recycling of the atoms moving at the correct velocity manifests itself as a sharp enhancement peak in the measured LIF spectrum. The optical pump effect becomes more severe at higher incident intensity, so the crossover peak grows with laser intensity. With the help of Na Doppler-free saturation spectroscopy, we can measure the LIF by the accuracy of ~1MHz. This is discussed in the first publication on the CSU Na lidar [She et al., 1990].

The above briefly and qualitatively discusses the Doppler-Free unit and some of the interesting features of the Na spectrum, which is the key of the laser locking system. The Lamb dip and crossover features in sodium saturation spectroscopy were first described

by Hänsch *et. Al.* (1971), and that paper remains an illuminating reference. Real sodium atoms consist of four sublevels in the excited state, separated by 15 to 60MHz, and six allowed transitions to the two ground sublevels. For each pair of allowed transitions, there exists a crossover feature. The natural linewidth for each transition is about 10MHz and thus of the same order as the separation of the excited sublevels; therefore the transitions within the D_{2a} and crossover are not resolved. For further detail of sodium's hyperfine structure and Doppler-free spectroscopy, see She and Yu (1995).

3-1. d. Pulsed dye amplifier for generating transmitter pulses

The PDA (Pulsed Dye Amplifier), which is pumped by a Quantum-Ray seeded Pulsed YAG laser (λ *=532nm, Power =16W*) from Spectra Physics, is the final stage of the transmitter. The locked c.w. seed beam is amplified about 10 times to ~1W averaged power and is sent into the atmosphere. At 50Hz repetition rate, the energy of each pulse is ~200mJ. Since the pulse width is ~7ns, the pulsed power is ~3MW, giving a pulse amplification of ~3 x 10^7. Since the pulse shape is not symmetric in time, and the frequency marker is provided by spectroscopy based on single-frequency dye laser, there exists a frequency difference between the frequencies of the c.w. seed laser and the frequency of the amplified pulses. Thus there is a need to measure this frequency bias, resulting from the distortion of the pulse spectrum due to the nonlinear effect in the PDA gain. This frequency (bias) monitor in Fig. 3-1, often called incorrectly as "chirp monitor" compares in real time the transmissions of pulse outputs at the three frequencies through an iodine cell maintained at 80°C to those of the three c.w. frequencies. The comparison provides information for the line-of-sight wind speed correction in real time.

The method of "chirp" correction has been studied in great detail by former students, Mike White [1999] and Jim Sherman [2002]. In the process, we display the laser output pulses by an oscilloscope, from which the operator is provided real time information on the status of ring laser, YAG laser, AOM and PDA.

3-2 Receiver

The first stage is a 14-inch diameter Schmidt-Cassegrain telescope of commercial, amateur-astronomical quality, which can be rotated and pointed to the direction desired. In normal operation we use two channels, one is pointing 30° from zenith to the east; the other is pointing 30° from zenith to the north. The east beam measures the zonal wind, the north beam gives the meridional wind and both give the temperature of the mesopause region. The telescope can be rotated to pointing zenith sometimes for vertical beam testing, which is necessary for checking the effectiveness of Faraday filter and wind bias monitor, and is discussed later.

The signal from each telescope is then transmitted through an optical fiber, optimally coupled to match the diameter and numerical aperture of the telescope. The interference filters (~3nm FWHM) are used to reject much of the background light, but it is not sufficient for daytime operation. So a pair of ultra narrow band (~ 0.002nm) Faraday filters are put in front of the PMT to block the daytime sky background during observation under sunlit conditions. The details of this Faraday filter will be described in Section 3-3a.

Finally, the optical signal traverses the optical fiber to the photon counting electronics, consisting first of a red-sensitive PMT and discriminator. To prevent overloading by the very strong scattering in the troposphere (Mie scattering from clouds and aerosol), the gain of the PMT must be reduced by a factor of 10^8 during the first $50\mu s$ after the laser has fired, and turned back on electronically. The discriminator converts the low-level (few tenths of volt) PMT pulses to logic level pulses (1.5 volts), so that they can be counted using conventional high-speed digital circuitry. Thereby, the return photons are converted into well-behaved voltage pulses, which continue via bnc to the counter for counting, time-of-flight binning, and summing over the selected integration time. The counter is triggered by the Q-switch output of the pulsed YAG laser in the transmitter system to initiate the clock for the time-of-flight binning. The counting electronics sorts the data associated with each pulse according to the operating frequency, so that summing of the signal in a given duration is done separately for each frequency. Because the signal from a single laser pulse is too noisy to construct a complete profile, the photon counts from many pulses are accumulated over time periods ranging from tens of seconds to several minutes depending on the desired measurement accuracy. Fig 3-6 shows a typical nighttime raw data files taken in October both without and with Faraday filters. The beam was pointing zenith at that night. The peak around 10km corresponding to the PMT gain turn to the full strength that we mentioned earlier and the signal from about 20km to 45 km is due to Rayleigh scattering. The presence of Na layer between 80 and 110km is evident from the raw data, with signal strength at D_{2a} a factor of 2-3 (3-4) stronger than those at 630MHz shifted frequencies without (with) Faraday filter.

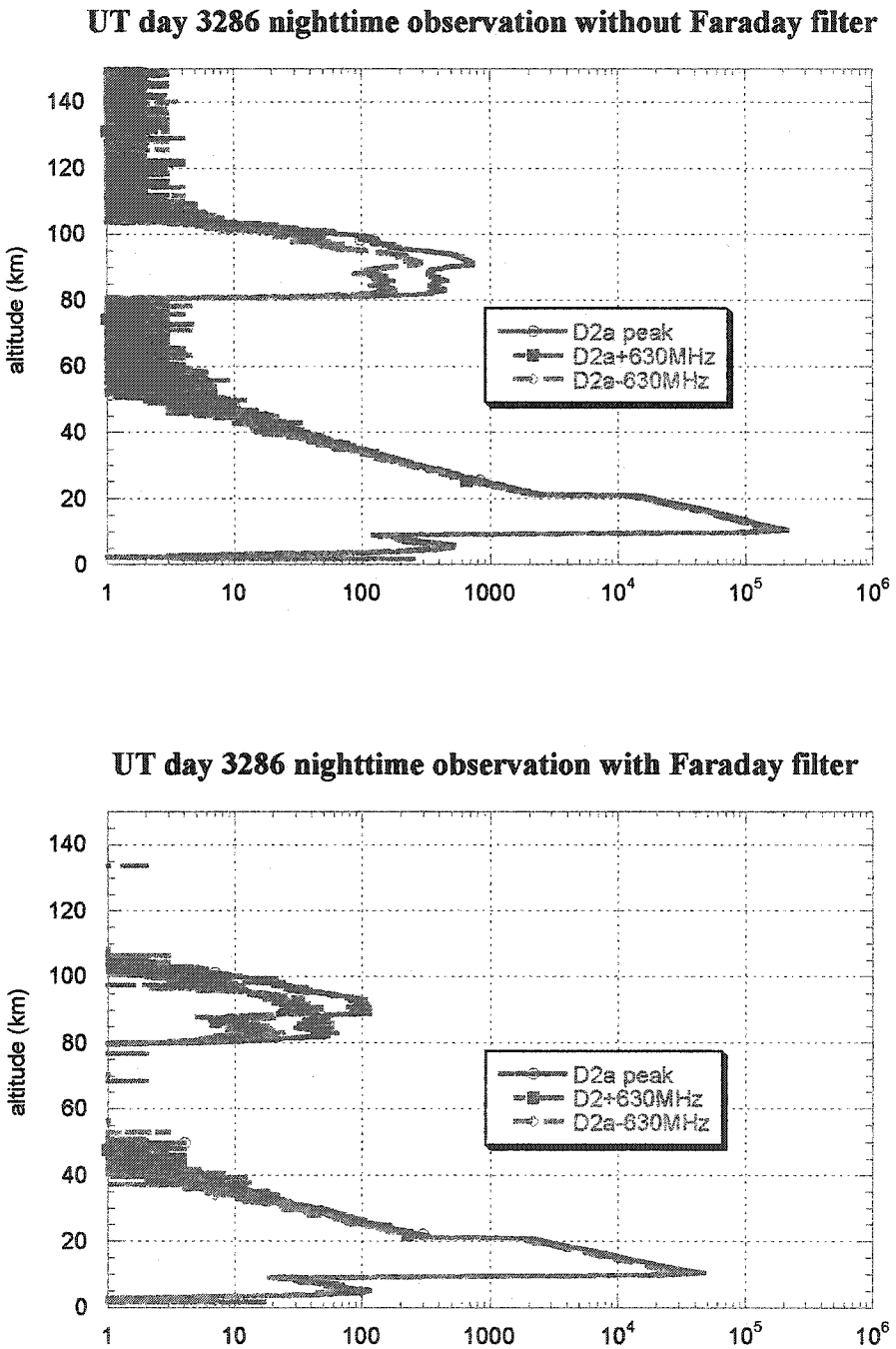

Fig 3-5 The raw data file (2-minute) of CSU Na-Lidar zenith beam observation without Faraday filter (top) and with Faraday filter (bottom). Horizontal scale is: photon counts/150m-2min between 21 to 150km, and photon counts/750m-2min below 21km

The Rayleigh signal from the "clean air" scattering region, containing few constituents with sizes comparable to the laser wavelength, can be used in two capacities, which is discussed in Chapter 4. First, the total counts from the region 20km to 40km are used as a monitor of the laser power transmitted through the changeable lower atmosphere at each of the lidar operating frequencies. Used in this way, the specific Rayleigh returns at each altitude are not important but rather a statistically well-determined sum from the entire range best establishes the relative laser power for each frequency. Second, the Rayleigh signal from a single reference altitude is necessary as a standard for determining the sodium density at range bins in the mesopause region. Used in this way, a range-resolved Rayleigh profile is necessary to accurately determine the Rayleigh return from a single altitude at which the air density is referenced to a standard atmosphere. Below 30km, particles and aerosols in the atmosphere scatter light in the ways that are difficult to predict and thus we use the Rayleigh return at 30km or 40km for normalization in the determination of Na density.

In addition to the lidar transmitter and receiver, two sky-monitoring radars survey the beam path for air traffic.

3-3 Na Faraday Filter

To achieve daytime lidar observation, a narrow band filter to block out the skylight, or broadband background noise is necessary. Conventional interference filters cannot provide extremely narrow bandwidths (0.001-0.01nm) with highly stable transmission peak and reasonably large field of view. Atomic resonance filter provides almost all what we ask for: wide field of view, high background rejection ratio and stable transmission.

So a pair of Faraday filters, based on anomalous dispersion, was used in CSU Na-lidar. Its fast time response and near- unity peak transmission make it even better.

The idea of using a circularly birefringent, dichotic medium between crossed polarizers to build the atomic resonance filter was first introduced by Ohman (1956), and the first filter of this kind was built in 1975 [Agnelli,G. et. al., 1975]. Then, it has been revived [Dick, et. al., 1991] and pursued for various laser-based application [Memders et. al., 1991; Yin. and Shay, 1991]. The Na Faraday filter in CSU Na-lidar system, which represents the first modern application in Na wavelength [Chen, H. et al., 1993; Chen, S. et. al., 2000], has achieved peak vapor transmission (apart from the losses arising from the optical components) of 85% at the line center of Na D_2 transition (λ=589.0nm) under a 1850G axial magnetic field, with a FWHM linewidth of 0.002nm (or 1.9GHz) and a background transmission of 2×10^{-5}.

3-3a Basic Theory of Faraday Filter

The Faraday anomalous dispersive optical filter consists of a heated sodium cell (at specific chosen temperature), housed in permanent magnets, and between two crossed polarizers. Basically, the sodium signal, which is on sodium resonance, was transmitted through the first polarizer and then through the sodium cell in an axial magnetic field. The magnetic field modifies the medium with Zeeman splitting and anomalous dispersion, leading to transmission and rotation of the plane of the polarization. For judicious choice of cell length the rotation is 90 degrees. Therefore, the sodium fluorescence signal can pass through the second polarizer with minimum loss. The polarization of the off-resonance sky background is not rotated and thus blocked by the

two crossed polarizers. In reality, there is still some sky background noise that is passed through due to the finite extinction of the polarizers. The operational principle of the Faraday filter may be understood by investigation of the refractive index of the Na cell at temperature T and in an axial magnetic field B.

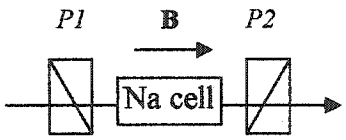

Fig. 3-6 Schematic of the Faraday anomalous dispersion optical filter (Faraday filter) design. Crossed polarizers P1 and P2 absorb all the light except that for which the polarization is rotated by the sodium vapor. From Arnold and She, 2003.

The index of refraction of the diluted vapor, like sodium vapor inside the cell, can be written as

$$n = \sqrt{1 + \chi} = \sqrt{1 + N_{vapor}\,\alpha} \qquad (3\text{-}1)$$

where χ, N_{vapor} and α are electric susceptibility, vapor density and frequency-dependent atomic polarizability. When the frequency is far away from resonance, the polarizability is zero, so the index of refraction ~1. As the frequency approaches resonance, the polarizablity changes (see the Fig. 3-7). It is considerably greater than zero when it is close to resonance, then drops dramatically below zero within the resonance. As the frequency increases far from resonance, the polarizability returns to zero. These features of polarizability contribute to the index of refraction of the vapor and thus a frequency dependent phase change of the propagating light.

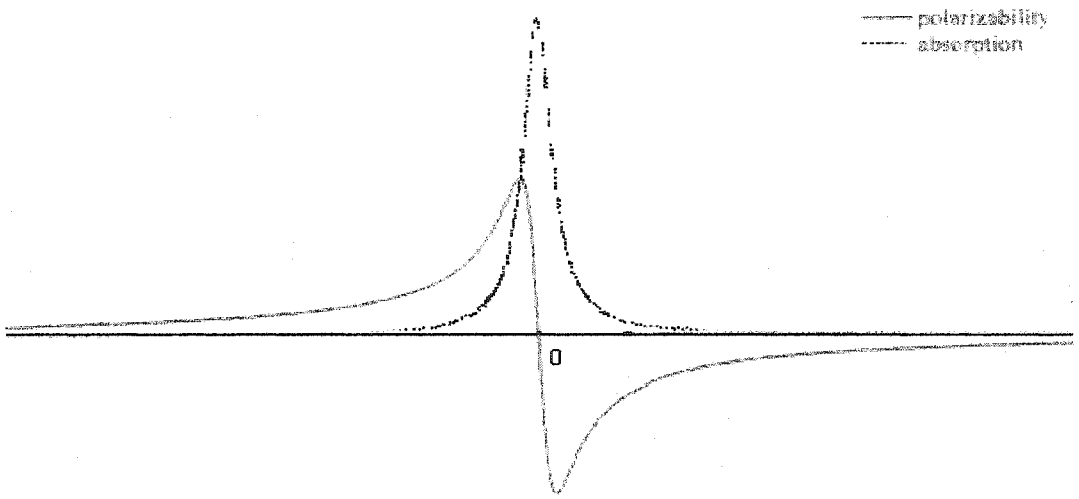

Fig 3-7 Theoretical Lorentzian absorption curve and atomic polarizability of a vapor in the neighborhood of a resonance frequency. The zero in frequency is at the center of the resonance line.

The first polarizer makes the random polarization light linearly polarized. Also, the eigenmodes of a beam propagating through the cell under an axial magnetic field are right and left circularly polarized light. So the linearly polarized beam, after the first polarizer, can be decomposed into a linear superposition of the right-circularly polarized and left-circularly polarized eigenmodes we mentioned above. For simplicity, we treat the sodium atom as two-level system with resonance frequency ν_0. Due to the strong axial magnetic field, the Zeeman effect splits the upper (and/or lower) level into two levels with resonance frequencies ν_0^+ and ν_0^-, and the Zeeman broadening is considerably larger than Doppler broadening of the Na spectrum. Because of the selection rules of quantum mechanics, each shifted level only interacts with one circularly polarized light. The right-circular light sees atoms with resonance at ν_0^-, and the left-circular light sees the ones at ν_0^+.

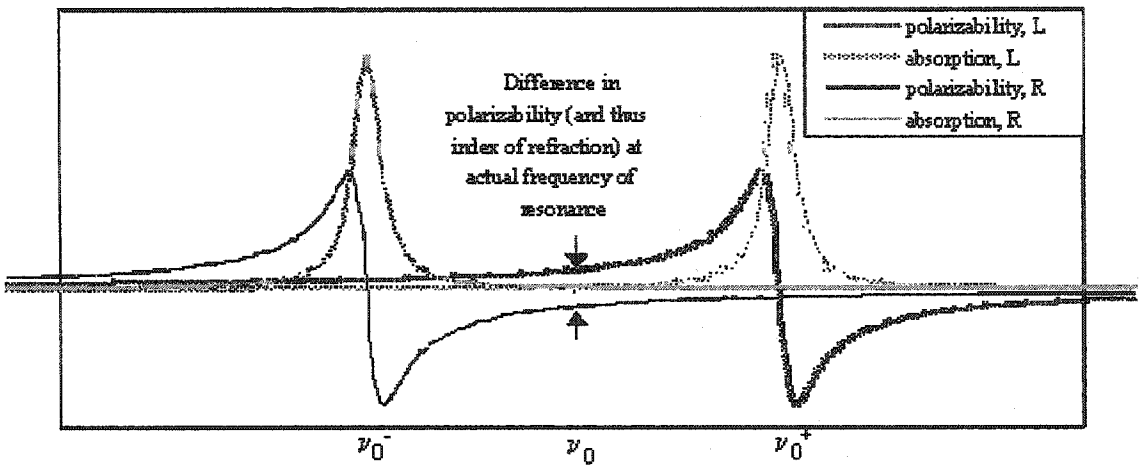

Fig3-8 With axial magnetic field, the resonance line v_0 splits into two due to Zeeman effect. Right-circularly beam interacts with v_0^- resonance line, and left-circularly beam interacts with v_0^+ resonance line.

If the magnetic field is strong enough, thus the Zeeman split is much larger than Doppler-broadening (to account for ensemble of atoms in thermal equilibrium) of the resonance line, and the absorptions at v_0 for both circularly polarized beams are zero. But they experience different polarizabilites, thus different indices of refraction (see the Fig 3-8, where the two arrow are pointing). This causes the relative phase between these two circularly polarized beams to change as they propagate through the cell. In other words, the polarization plane changes its direction along the cell. The change in relative phase, $\Delta\Phi$, is:

$$\Delta\Phi = 2\pi\frac{l}{\lambda}\Delta n = 2\pi\frac{l}{\lambda}\left(n^+ - n^-\right) \tag{3-2}$$

The index of refraction also depends on sodium density inside the cell, which is temperature dependent (see Section 3-3b). For fixed cell length and magnetic field, if we properly choose the cell temperature, we can achieve relative phase change equal to π. That gives the beam polarization plate rotation of 90 degree from its initial direction, so

that the signal at v_0 can pass the second polarizer without much absorption. The measured transmission function is shown below.

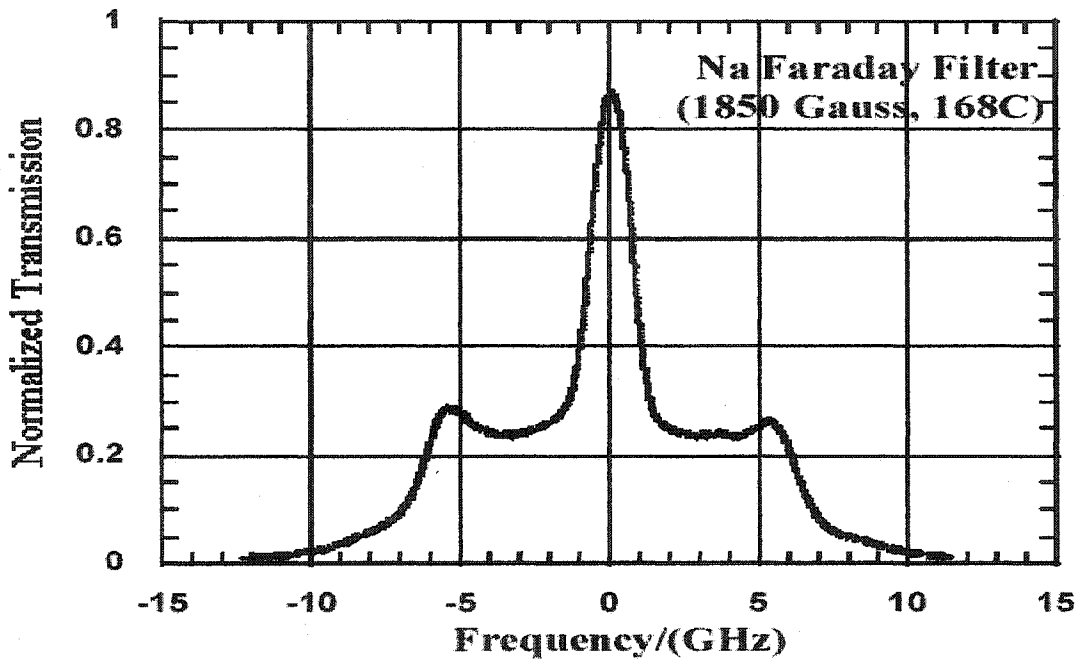

Fig3-9 Normalized transmission function of Na Faraday Filter at 168 C° with 1850G axial magnetic field. From Arnold and She, 2003

The LIF (laser induced fluorescence) back from the sky is randomly polarized, so the first polarizer cuts 50% of the light. The other half gets into the Faraday Filter, and theoretically, the peak transmission should reach 50%.

There are some very interesting features in this transmission function. The first one is the plateau around ± 3GHz in the figure above, Fig. 3-9. Comparing with Fig3-8, we notice that at v_0^- (or v_0^+), the right (or left) circularly-polarized beam is totally absorbed, but the left (or right) circularly-polarized beam at v_0^-(or v_0^+) experiences no absorption at all, so that it can propagate uninhibited through the cell. Then, half of it passes through the second polarizer, giving rise to 25% transmission. Considering the loss at each optical surface, the use of Faraday Filters reduces the signal by roughly 5, although it reduces the

skylight background about 6000. For detail calculation and discussion, consult Yeh (1982) and Chen *et al.* (1993).

3-3b The Structure of Faraday Filter

As mentioned above, the relative phase change $\Delta\Phi$ can be controlled by sodium density inside the cell, which is dependent on temperature and pressure. Our Na cell in the Faraday has a tip-off region which is the reservoir containing metallic Na; its temperature controls the vapor pressure. In order to control both temperature and pressure of the Na cell, we independently control the temperatures of the cell and the tip-off region. There is no background gas in the Na cell we use here.

According to ideal gas law,

$$\begin{aligned} P_{cell} V &= N k_B T_{cell} \\ P_{cell} &= \rho_{cell} k_B T_{cell} \end{aligned} \tag{3-3}$$

where, P_{cell} is the pressure inside the sodium cell, k_B =1.3806503 × 10^{-23} m^2 kg s^{-2} K^{-1} is Boltmann constant and ρ_{cell} is the sodium density. So, the precise controls of the pressure and temperature of the cell are the key factors of this filter as Na density, ρ_{cell} must be kept constant. The P_{cell} is determined by the sublimation of the sodium in the tip-off part of the cell. The relationship between P_{cell} and tip temperature can be expressed as following

$$\log_{10} P_{vapor} = -\frac{0.05223\, a}{T_{tip}} + b \tag{3-4}$$

P_{vapor} is in *mm* of mercury, which is the same as P_{cell} in our case, and T_{tip} is in *Kelvin*, $a=103300$ and $b=7.553$, are constants associated with sodium. Fig 3-10 gives us the idea how the cell pressure changes with tip temperature.

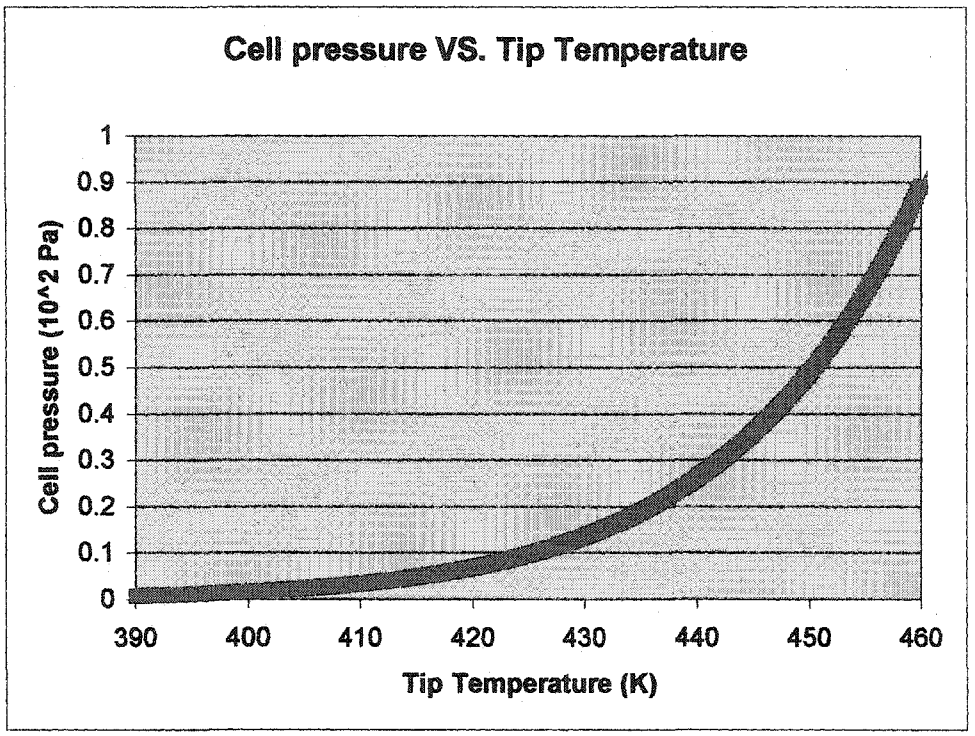

Fig3-10 Cell pressure as a function of Temperature at the tip part

Since the transmissions of the Faraday filters must stay constant during the data observation, proper control of the filters temperatures is very necessary. The two temperatures, T_{cell} and T_{tip}, play different roles in modulating the density inside the cell. The stabilities of them are both required, but which one is more critical, or in other words, which temperature's stability is more important to achieve stable transmission function of the Faraday Filter, thus must be more carefully controlled. To understand this, equations (3-3) and (3-4) are studied in detail below.

Let $A=0.05223\times a$, according to (3-4), we can get

$$\frac{dP_{vapor}}{dT_{tip}} = -P_{vapor}\frac{A}{T_{tip}^2} \Rightarrow \frac{dP_{vapor}}{P_{vapor}} = -\frac{A}{T_{tip}}\frac{dT_{tip}}{T_{tip}} \tag{3-5}$$

From (3-3), the ideal gas law, for fixed T_{cell}:

$$dP_{vapor} = k_B T_{cell} d\rho_{cell} \tag{3-6}$$

Put (3-6) into (3-5),

$$\frac{d\rho_{cell}}{\rho_{cell}} = \frac{A}{T_{tip}}\frac{dT_{tip}}{T_{tip}} \tag{3-7}$$

At normal operation tip temperature, which is about 148°C, A/T_{tip} roughly equals to 12.8. Also from (3-3),

$$\frac{d\rho_{cell}}{dT_{cell}} = -\frac{P_{vapor}}{k_B}\frac{1}{T_{cell}^2} \Rightarrow \frac{\partial\rho_{cell}}{\rho_{cell}} = -\frac{\partial T_{cell}}{T_{cell}} \tag{3-8}$$

From (3-7) and (3-8), we can see that, due to the factor of A/T_{tip}, it is obvious that the variation of tip temperature is more critical for the sodium density inside the cell than the cell temperature. That is the same amount of change in tip temperature can induce ~13 times bigger effect in density than the same change in cell temperature does under normal operation temperature (170°C for cell, and 148°C for tip). Therefore, we must precisely control the tip-off region temperature to achieve reasonably stable transmission function, which is quite important for the wind measurement.

The following picture is a simple diagram of the Faraday filter used in CSU Na-Lidar system at present. Notice that there are two aluminum ovens inside, heating and stabilizing the cell and tip respectively. Two temperature controllers, both of which can

reach accuracies of ± 0.1°C, modulate their temperatures. The coated optical windows on both side of the oven completely seal the sodium cell inside the oven, and minimize the effects of outside temperature fluctuations. The aluminum oven is covered by the Teflon pieces, which can stand high temperature, and are a very good insulation layer between sodium cell and magnets (high temperature may cause the permanent magnet losing magnetic field, so the insulation layer must separate the oven and the permanent magnet). To work properly, the two polarizers (Melles Griot Glan Thompson Prism-03 PTH 016/A has the maximum operation temperature of 75°C) must avoid the high temperature from the oven, so they are also wrapped with the Teflon insulation, which is not shown in Fig 3-11. The two filters are then put inside a box on plastic base to reduce the effect of the surrounding temperature fluctuations. The plastic base has groove, so that the Faraday Filters can be moved in and out of the beam path very conveniently.

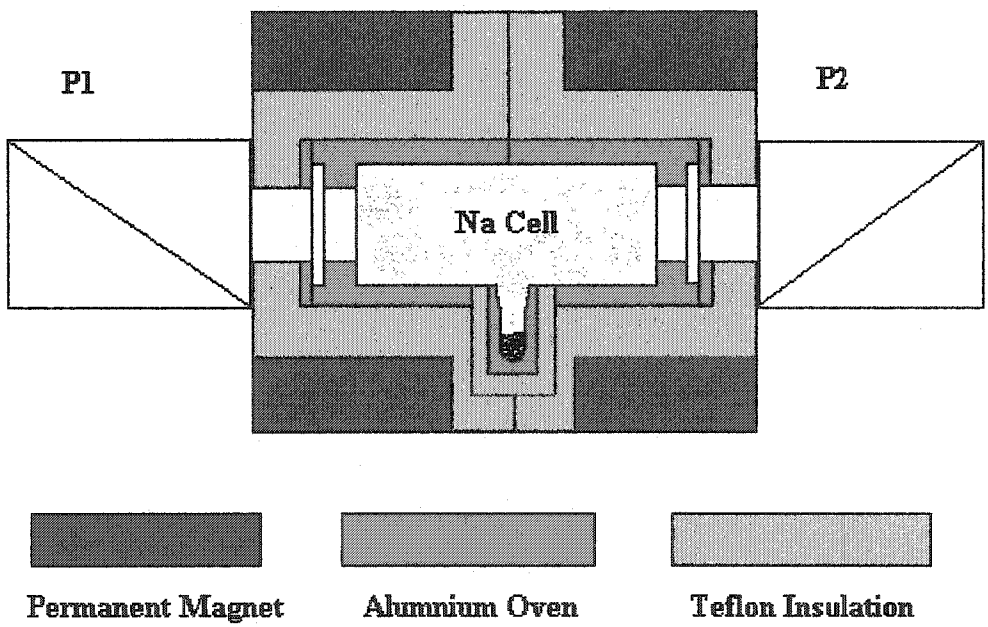

Fig3-11 The Cross-section diagram of Na Faraday Filter used in CSU Na-Lidar system

3-3c The reliability and stability of the Faraday filters

Reliability and stability of the Faraday Filter's transmission function are essential for the daytime lidar observation. Although, compared with the wind measurement, the stability problem would not bring much trouble for the temperature measurement, it is extremely important for the wind speed detection, due to the formation of the wind ratio (2-8). We will discuss it later in this section.

Therefore, periodic measurement of the transmission function and a vertical beam test are necessary. The vertical wind speed should be close to zero. So, if the lidar is running with the Faraday Filter in the receiver, the total result of the vertical wind speeds for a few hours should be bunched together, and also close to zero. In the following, we will discuss these two kinds of measurements in detail separately.

One-way to check the stability of the Faraday filters is to measure the normalized transmission function of this pair of Faraday filters every a couple of month, under the same temperature setting. The measurement setup is shown below in Fig (3-12). The tunable laser beam used as the light source is divided into three channels. One goes through a Fabry-Perot interferometer, which works as a frequency marker. Remember, the Ring Dye laser's scan is not at uniform speed. One is detected by a photo diode (Diode2) directly as intensity reference channel. The other beam is coupled by a multimode optic fiber (same as the fiber used to collect the signal photons from the telescope), and sent into the Faraday Filter. When scanning the laser, each diode records the light intensity simultaneously, and the ratio of I_1 / I_2 gives the transmission function.

Of course, the diodes background noises are measured, and subtracted in the analysis program.

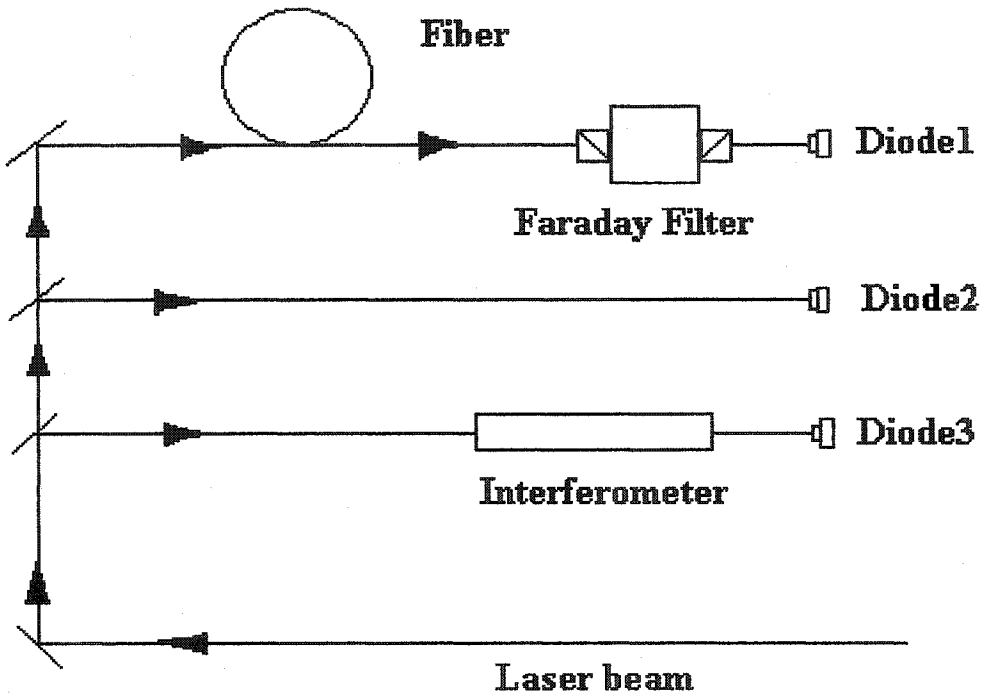

Fig 3-12 Faraday Filter Normalized Transmission function measurement: The interferometer is working here as a frequency calibration instrument of the laser scans, because the Ring Laser's frequency scanning is not quite linear.

The graph below (Fig3-13) shows a typical 20GHz scanning profile. The red line is the signal passing through the Faraday Filter and recorded by Diode1. To normalize the signal with the power fluctuation, the blue line shows power variation detected by the reference intensity channel, which is almost the constant during the scan, but it does show some variation. The green line indicates the inverse sodium Doppler-free spectrum. In this figure, the "0" frequency point of the horizontal axis is centered at the D_{2a} peak. The other sharp features in the Doppler-Free spectrum are D_{2a}, D_{2b} peaks, and the Crossover can also be seen between these two peaks.

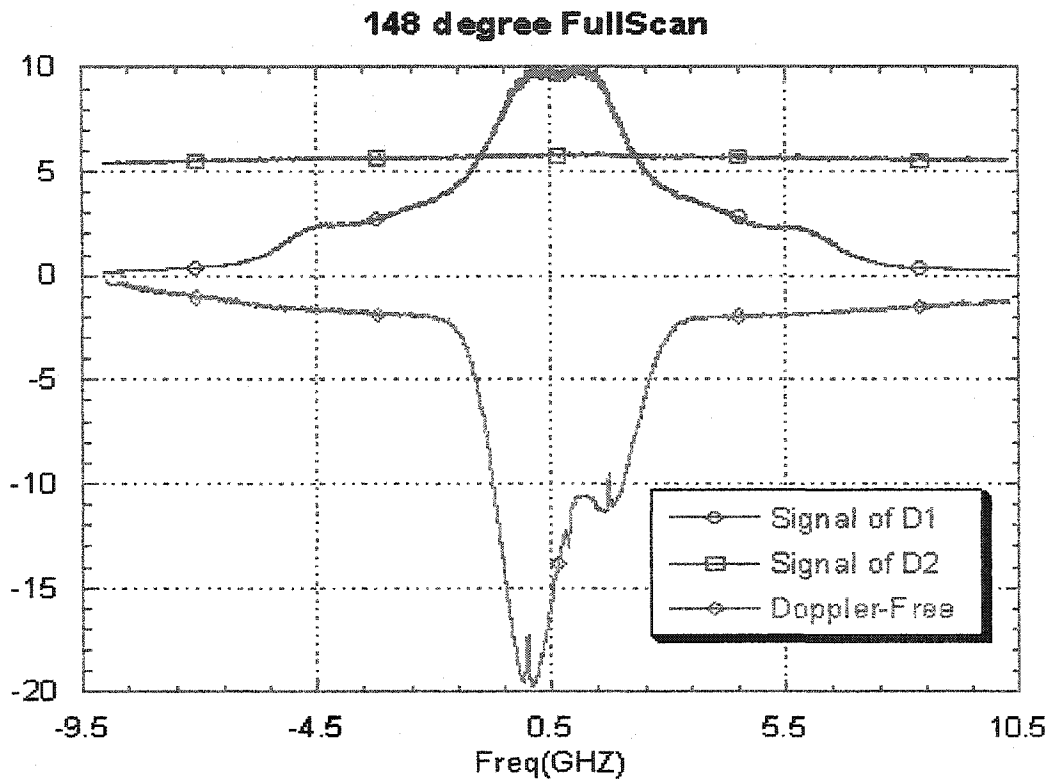

Fig3-13 20GHz Scan of the Faraday Filter at 148°C tip temperature and 170°C cell temperature, in red. Also shown are diode 2 signal, in blue, giving laser power reference, and inverted Doppler-free spectrum in green.

When choosing the operation temperature of the filters, not only should we consider the decent transmission, but also the lifetime of the sodium cell. Since sodium is one of the most active elements in the world, its demise due to atom and cell wall collision is inevitable. So, under the condition of getting decent total transmission, we want to run the Faraday Filter at lowest temperature possible. The temperature setting we are using right now is: $T_{cell} = 170°C$ and $T_{tip} = 148°C$, for both filters, and the resulting transmission spectra of the two different filters are very similar. If for the same temperature setting, the transmission function keeps getting broader, and every time the scanning measurement is taken, the sodium cell must be replaced. So far, the two sodium cells inside the Faraday Filters have been operating for 20 months. This excellent lifetime is only possible when

an operation routine is developed. In our case, we leave the Faraday filter on a standby setting when not in use, with oven at 50°C and tip-off at zero. Originally it was design to avoid the sodium condensation on the cell wall as the filters cooled off. We then prepare the Faraday filter operation by first turning on the oven to 170°C, then the tip-off to 148°C. The Faraday filter is left in this condition for ~2 hours before use.

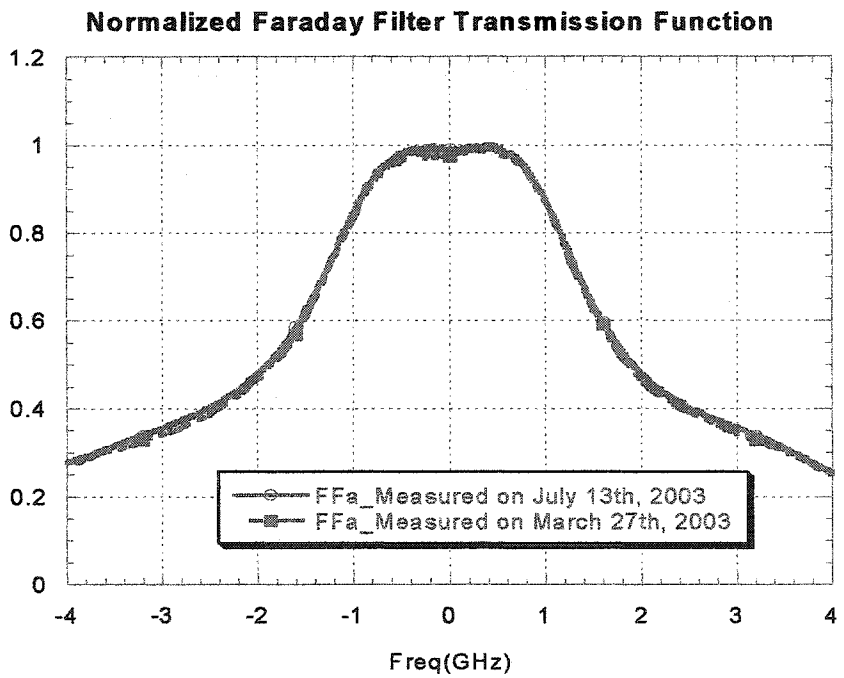

Fig3-14 Normalized Transmission functions comparison

Fig3-14 shows the comparison of two transmission functions, which were measured at different time in 2003, one on March 27th 2003; the other on July 13th. Notice that the zero on the horizontal axis is no longer D_{2a}, but the center of mass of the Na D_2 spectrum. This change of zero frequency is to be consistent with the data analysis program.

Overall, the two functions show good similarities, though there are small differences on the shoulders, which could induce ±1m/s difference in wind measurement, but hardly any noticeable variation in temperature calculation, due to less sensitivity in temperature ratio R_{temp} than in wind ratio, R_{wind}.

Before we declare the success of the Faraday Filter, we also need to test its use in the real situation. The way is to measure the vertical wind, which theoretically should be close to zero for all altitudes when averaged over duration longer than 1 hour, with the Faraday Filter in and out. If these two vertical wind speeds are very close to each other and reasonably close to zero, we ensure the validity of Faraday Filter. Fig. 3-15 gives the results of this measurement taken at the night of UTday 203 in 2003. Each resulting curve is the observed vertical wind profile average for 4-hour. The vertical structures of these two situations are a little bit complicated, but they show the similar results and bunched together at 0m/s line. The dramatic increase in green error bars below 83km indicates the lack of photons passing through the Faraday filter, inducing large error. The vertical speed at the sodium peak region, where the sodium atoms are most abundant and therefore has the least error bar, shows the difference between these two measurements is about 1m/s, which is smaller than the error bar (The error bar in the temperature and wind measurement here comes from the photon noise, which is calculated by the square root of the total signal, including background noise). It should be pointed out that there exists a small wind bias, of 2-3m/s, and this was removed by the use of real time frequency bias monitor. The wind bias correction was made for the vertical wind profile taken without Faraday filter. This is not done for the profile with the Faraday filter in, because the bias is smaller than the error bar in this case.

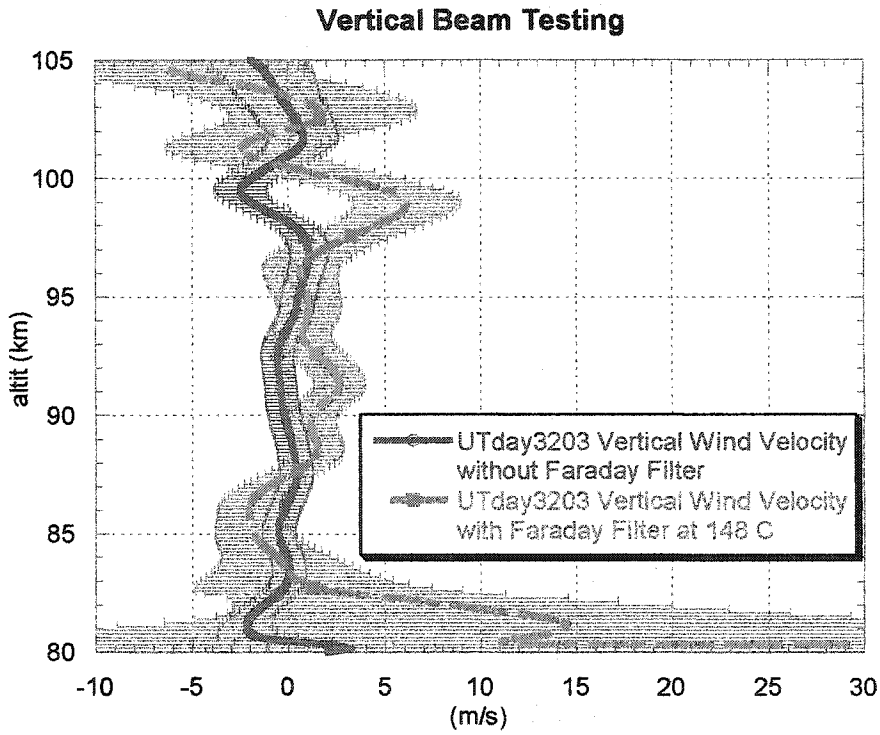

Fig 3-15 Vertical Wind Measurement with Faraday Filter in and out. Wind bias correction of about 3m/s was applied for the profile without Faraday filter, while the wind bias was not applied for data with Faraday filter as it is smaller than the error bar.

After all these stability and reliability tests, we can finally claim this design and construction of Faraday Filter is successful, and it represents another significant milestone of CSU Na-Lidar system. Faraday filter were used for 24-hour continuous temperature measurement between 1997 and 1999 [Chen et al., 2000]. This was followed by simultaneous measurements of temperature and line-of-sight wind off and on in 2000 and 2001. However, the stability was not good or robust enough for long-period wind measurements. It was only after the implementation of two ovens with independent temperature controls in Feb-Mar 2002, one for the Na cell and the other for the tip-off region as a part of this thesis, that the Faraday became stable and robust enough for long-

period wind measurements under sunlit conditions. Another improvement of the Faraday Filter operation is maintaining the cell at lower temperature (50°C) when it is not in operation. This was originally designed to avoid condensation of the Na on the cell wall when the cell is cooled down, but it turns out to be very helpful for increasing the cell lifetime. Till now, the two Na cells have not been replaced for more than one and a half years. It took more than one year's improvements and testing to reach a point when a continuous multiple day campaign can be executed. Our current record is 9 days terminated only by weather.

3-3d Limitation

Although daytime observation has become routine for CSU Na-Lidar using Faraday Filter since May 2002, the filters reduce the daytime signal to about one fifth of the nighttime. The main shortcoming of this Faraday Filter design is that the first polarizer of the Faraday Filter cut the signal by 50%, making the daytime data quality in the summer poor when compared with those in the winter. If we can save this 50% loss, which is quite possible, we can double our signal in the daytime. Fortunately, a new generation of Faraday Filter that will do this is under construction. This new design picks up that 50% loss, and seeds through the Na cell. This way, it should increase the signal level by the factor of two, though the signal-to-noise of the daytime measurement, especially near local noon, is mainly determined by how much sky background passing though the Faraday filter, which is limited by the extinction ratio of the two crossed polarizers as discussed below.

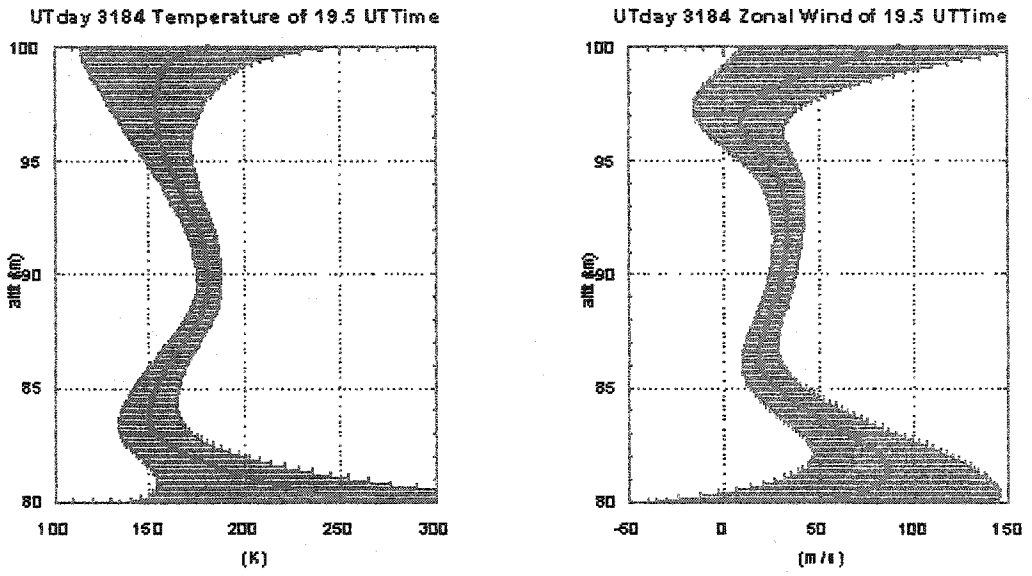

Fig3-16 Average Zonal Wind and Temperature of UTTime 19.5 (12:30am LST) on July 3rd 2003

Even thought the extinction ratio of the two cross polarizers is about 10^{-5}, there are still considerable skylight background getting into the PMT, which is especially problematic near local noon. This limits the daytime affective range of the lidar in summer (especially during the June and July when the sodium density in the mesopause drops to its minimum of the year ~$10^{8} m^{-3}$) to between 83 and 100km. Furthermore, due to low signal-to-noise ratio, the maximum error of the hourly wind measurement could reach over ±15m/s and ±10K for the temperature at sodium peak, with larger value near the edge of the sodium layer. To improve this, not only the new Faraday Filter design is required, but also a bigger telescope is needed. Fig3-16 shows the zonal wind and simultaneous temperature measurements at noon on July 3rd, 2003. Due to the low Na density and high sky background, from the two plots above, people can see that the error bars for temperature and wind measurements at the sodium peak region (92km) are about 15K and 15m/s respectively, whereas in the winter midnight, those error bars could be 1K and 1-2m/s.

Reference:

Arnold, K. S. and C. Y. She, Metal fluorescence lidar (light detection and ranging) and the middle atmosphere. *Contemporary Phys. Vol. 44*, No. 1, 35-49, 2003.

Agnelli, G., A. Cacciani, and M. Fofi, The magneto-optic filter, *Solar Phys.* 44, 509, 1975.

Chen, H, C. Y. She and Eric Korevaar, Na Vapor Dispersive Faraday Filter *Opt. Lett. 18*, 1019-1021, 1993.

Chen, S., PhD dissertation: Sodium/Potassium Faraday Filter for daytime Lidar Temperature Observations and Study of tidal Waves in the Mesopause region of the Atmosphere, Colorado State University. 1999.

Chen, S. S., Z. L. Hu, M. A. White, D. A. Krueger, and C. Y. She, Lidar observations of seasonal variation of diurnal mean temperature in the mesopause region over Fort Collins, CO (41N, 105W), *J. Geophys. Res.,105*, 12371-12379, 2000.

Dick, D. J. and Shay, T. M., Ultrahigh-noise rejection optical filter, *Opt. Lett. 16*, 867 1991.

Menders, J., Benson, K., S. Bloom, H., Liu, C. S. and Korevaar, E., Ultranarrow line filtering using a Cs Faraday filter at 852 nm *Opt. Lett. 16*, 846 1991.

Ohman, Y. *Stockholm Obs. Ann.* 19, 3, 1956.

Sherman, J., PhD dissertation: Mesopause Region Thermal and Dynamical Studies Based on Simultaneous Temperature, Zonal and Meridional Wind Measurements with Upgraded Sodium Fluorescence Lidar. Colorado State University, 2002.

White, M. A., PhD dissertation: A Frequency-agile sodium Lidar for the Measurement of Temperature and Velocity in the Mesopause Region, Colorado State University. 1999.

Yeh, P., Dispersive magneto-optic filer, *Appl. Opt., 21*, 2069, 1982.

Yin, B. and Shay, T. M., Theoretical model for a Faraday anomalous dispersion optical filter, *Opt. Lett.16*, 1617, 1991.

Chapter 4 CSU Na-Lidar Diurnal Observation

After showing the basic theory and important components of the CSU Na-Lidar system in the previous three chapters, we discuss some numerical methods used in CSU Na-Lidar, and some scientific results from the diurnal observations. First, the data analysis process, which includes the general lidar equation and the related data-processing algorithm, is presented and discussed. Then, the mean temperature and wind field based on the CSU lidar diurnal observation, along with the detected tidal signatures in the temperature and winds will be presented.

4-1 Lidar Equation and Data-Processing Algorithm

The data processing converts the photon counts into the atmospheric temperature and winds. We start from the general lidar equation, and then present the necessary data processing algorithm for the CSU Na-lidar system. It should be noticed that, although we define the range of sodium layer from 70km to 120km, accurate temperature, radial wind and sodium density are only achieved from around 80km to 105km for most of the months due to poor signal-to-noise ratios at the lower and upper boundaries of the sodium layer.

4-1a Lidar Equation

The theoretical performance of any lidar system is governed by the lidar equation. The expected received photon count is equal to the product of the system efficiency, the number of transmitted photons, the probability that a transmitted photon is scattered and

the probability that a scattered photon is received. For resonance fluorescence systems the lidar equation is given approximately by [Gardner, 1989]

$$N(z) = (\eta T_A^2)\left(\frac{P_L \tau}{hc/\lambda}\right)(\sigma_{Na} n_{Na}(z)\Delta z)\left(\frac{A_R}{4\pi z^2}\right) T_{up} T_{down} + N_B R \tau \qquad (4\text{-}1)$$

where

$N(z)$ = expected number of sodium backscattering photons detected in the range interval $(z-\Delta z/2,\ z+\Delta z/2)$

$n_{Na}(z)$ = Na density at range z (m^{-3})

N_B = expected photocount per range interval Δz per pulse due to background noise and dark counts

σ_{Na} = effective Na backscatter cross section (m^2)

Δz = receiver range bin length (m)

A_R = receiving telescope aperture area (m^2)

λ = optical wavelength (589.16nm)

h = Planck's constant (6.63×10^{-34} J/s)

c = speed of light (3×10^8 m/s)

P_L = laser power (W)

T_A = one-way extinction of the lower atmosphere ($z < 70km$)

T_{up} = upward traveling beam extinction through the sodium layer

T_{down} = downward traveling beam extinction through the sodium layer

R = laser pulse rate (s^{-1})

τ = integration time (s)

η = lidar efficiency

Equation (4-1) includes both the upward and downward extinctions of the laser beam as it propagates through the layer, and it is also assumed here that the power densities of the beam within the layer are small enough to ignore the effects of stimulated emission from the Na atoms.

The first factor in parenthesis in (4-1) is the overall system efficiency. The lidar efficiency η includes the optical efficiencies of the fiber coupling, beam splitters, mirrors, lenses, and optical filters in the laser transmitter and the receiving telescope as well as the quantum efficiency of the PMT. The dominant parts of η are the optical filter transmittance and the detector quantum efficiency. At the sodium D_2 frequency, PMTs with GaAs photocathodes have quantum efficiencies between 10 and 20 percent. Wideband optical interference filters with bandwidths greater than 3nm FWHM, which are usually put between the end of coupling fiber and the PMT, also cause some optical loss. The Faraday filter, which is one kind of narrowband filter (FWHM: 2GHz) that is required for daytime observation, has transmittances of about 20 percent under current design. Therefore, the system efficiency for the CSU Na-lidar ranges between 1 and 5 percent, with smaller values corresponding to narrowband systems operating during daytime and the larger values for nighttime observation.

The atmospheric transmittance T_A depends on the wavelength and clarity of the lower atmosphere and must be calculated. Absorption by ozone at near UV wavelengths and by water vapor and carbon dioxide at near IR wavelengths can significantly reduce the atmospheric transmittance. However, CSU Na-lidar has the advantage of being located over 5000 feet above sea level, and under excellent seeing conditions, at the Na wavelength, T_A, under clear sky, can be approximately 80 percent for zenith observations.

The second factor in the lidar equation is the number of transmitted photons. The factor $P_L\tau$ gives the total laser energy for a given integration time τ, and hc/λ is the photon energy. The third factor in parenthesis is the probability that a transmitted photon is

scattered by an Na atom, and this probability is equal to the product of the effective Na backscatter cross section σ_{Na}, the Na density $n_{Na}(z)$, and the scattering layer thickness or a range interval Δz. The fourth factor is the probability that a scattered photon is collected by the receiving telescope. For isotropic scattering, this probability is equal to the telescope area A_R divided by the area of a sphere with radius = z, which is $4\pi z^2$. Here, z represents the distance from the scattering source to the telescope, not altitude.

The last term of the lidar equation represents PMT dark counts or counts from light sources such as stars, moonlight, city lights, and sky background, etc. It is assumed that the signal counts above sodium layer all come from the background sources. Therefore, this term ($N_B R\tau$) can be easily experimentally determined by averaging the detected counts in range bins between 120-150 km.

When the laser beam is ascending through the sodium layer in the mesopause, some of the photons it carries are absorbed by the atmospheric sodium and re-emitted in other directions. Although this provides the backscattering fluorescence signal essential for a lidar, it also causes an attenuation of the laser beam as it travels upward. Similarly, the backscattering fluorescence signal from an altitude range in the sodium layer must also travel through several kilometers of sodium gas in which it can be absorbed and re-emitted, and thus attenuating the signal on its way back to the lidar receiver. The term ($Tup \cdot Tdown$) in the lidar equation shows these two effects, and details of each will be discussed below.

First consider the extinction of the ascending photons. Since the attenuation of the laser beam is caused by laser light being absorbed by the sodium and scattered in all directions,

it is the total absorption cross section which governs this interaction. This transmission of the beam as it ascends from an altitude z_L (designating the bottom of the observed sodium layer) to a given range bin at z may be written:

$$T_{up} = \exp\left[- \int_{z_L}^{z} n_{Na}(z') \, \sigma_{Na}(\nu_L, T) dz' \right] \tag{4-2}$$

where the ν_L represents the laser frequency. It is important to know that this calculation starts from the bottom of mesopause sodium layer, so any attenuation below it is counted elsewhere, i.e. in T_A.

After the transmitted photons are absorbed and back scattered from a give range bin to be detected by the lidar receiver, the journey of the emitted backscattered photons is subject to attenuation by the sodium layer below. Compared with ascending extinction, the descending extinction is more complicated, because the backscattered light is no longer at a single frequency, but arises from ten fluorescence pathways (in six different frequencies) available in the sodium D_2 transition and can be written as

$$T_{down} = \sum_{j=0}^{10} P_j \exp\left[- \int_{z_L}^{z} n_{Na}(z') \, \sigma_{Na}^{j}(\nu_j, T) dz' \right] \tag{4-3}$$

where P_j represents the fraction of the total scattered photons which are excited from the j^{th} of the ten fluorescence pathways. As in T_{up}, the integral starts from the bottom of the mesopause sodium layer z_L. For the daytime data analysis the Faraday filter transmission is also included.

In addition to the beam attenuation in the atmospheric sodium layer, the laser beam extinction and scattering below 80km is required for the transmission T_A before the laser beam reaches the sodium layer, and thus to complete the discussion of the lidar equation (4-1). Although particles and aerosols exist in the lower atmosphere, they scatter the light in ways that are difficult to predict, and the well-studied Rayleigh scattering from the "clean air" provides much information on the atmosphere below sodium layer. We discuss two approximations. One is to assume that the atmosphere between about 20km and the bottom of sodium layer is perfectly transmitting. The second is regarding the scattering above 30km as purely Rayleigh scattering. The expected photon count at Rayleigh scattering altitudes is given by

$$N_R(z) = (\eta T_R^2)(\frac{P_L}{hc/\lambda})[\sigma_{Ray} n_{air}(z)\Delta z]\left(\frac{A_R}{4\pi z_{Ray}{}^2}\right) + N_B R\tau \qquad (4\text{-}4)$$

For small laser frequency shifts (on the order of gigahertz) the Rayleigh scattering (non-resonant) cross-section can be treated as constant here. T_R, which represents the round-trip transmission through the complicated lowest 30km of the atmosphere, is way too complicated and changeable due to the Mie scattering by large particles and aerosols to be numerically calculated. But, by using the relationship

$$T_A^2 = T_R^2 \exp\left[-2\int_{z_{Ray}}^{z_L} n_{air}(z',t)\sigma_{Ray}\, dz'\right] \qquad (4\text{-}5)$$

and a simple approximation that the atmosphere is in hydrostatic equilibrium, so that the total Reyleigh crosssection is almost constant from the z_{Ray} to z_L.

Further more, the air density change is so small in the region (35-70km) that

$$\exp[-2\int_{z_{Ray}}^{z_L} n_{air}(z',t)\sigma_{Ray}\,dz'] \approx 1$$

then, we can easily form a ratio between the Rayleigh signal and sodium signal to get rid of the complicated transmittances. Our signal is given as

$$\frac{N(z)-N_B R\tau}{N_R(z)-N_B R\tau} = \frac{N_{Na}(z)}{N_{Ray}(z_{Ray})} = \sigma_{Na}(\nu_L,T,V)\frac{n_{Na}(z,)T_{up}T_{down}}{\sigma_{Ray}n_{air}(z_{Ray},t)}\frac{z_{Ray}^2}{z^2} \qquad (4\text{-}6)$$
$$\left(hc/\lambda_L\right)$$

The equation above also shows that the Rayleigh signals can be used to normalize the sodium signals to the laser power, if a proper reference altitude can be found. For the CSU lidar, 30km is chosen as the reference altitude, because this altitude is too high to be contaminated by the complex Mie scattering, but it is also low enough to get decent Rayleigh signal. From now on, the signals (Rayleigh and Na) we talk about are all background-subtracted signals. Using (4-4) and replacing z_{Ray} with z_{ref} = 30km, we get

$$\eta T_R^2\left(\frac{P_L}{hc/\lambda_L}\right)\left(\frac{A_R\Delta z}{4\pi}\right) = \frac{z_{ref}^2 N_{Ray}(z_{ref},\nu_L)}{i2_{ref}N_{Ray}(z_{ref}Ray} \qquad (4\text{-}7)$$

Substituting this into (4-1), we achieve the main result

$$\frac{N_{Na}(z,t,T,V)}{N_{Ray}(z_{ref},\nu_L)T_{up}T_{down}} = \sigma_{Na}(\nu_L,T,V)\left(\frac{z_{ref}^2 n_{Na}(z,t)}{z^2 n_{air}(z_{ref},t)\sigma_{Ray}}\right) \qquad (4\text{-}8)$$

This relation will be discussed and used in the next later in this section to configure the temperature and wind ratios. Notice that there is no frequency dependence in the parenthesis on the right side of the equation (4-8).

We already discussed the basic idea of how to get mesopause temperature and wind speed by using two simple ratios in Chapter 2. We now present the details of data-processing algorithm on how to determine the atmospheric parameters of interest from photon count profiles.

The temperature and wind information is contained in the sodium D_2 differential backscattering cross-section, which for isotropic scattering between two levels is [Sherman, 2002]

$$\frac{d\sigma_{Na}}{d\Omega}=\frac{\sigma_{Na}}{4\pi}=\left(\frac{g_2}{g_1}\right)\frac{\lambda_L^2}{2}A_{21}\cdot g(\nu,T,V) \tag{4-9}$$

where A_{21} is the Einstein A coefficient and g_2/g_1 is the degeneracy ratio. For sodium D_2 transition, they are $6.289\times10^{7}s^{-1}$ and 2, respectively. The absorption cross-section for this transition is $\sigma_{Na}= 9.5 \times 10^{-16}$ m^2.

In Chapter 2, we have already discussed the sodium fluorescence spectrum. There, we did not include the effect of the laser lineshape. However, since we cannot get a laser with delta function laser lineshape, we must include the actual laser lineshape (Both the Coherent Ring Laser and the Pulse Dye Amplifier's laser lineshape functions) into the data processing algorithm to get realistic results. Then, the sodium fluorescence spectrum induced by a laser with normalized (to unit area) lineshape $L(\nu-\nu_L)$ is given by the

correlation of the laser lineshape with the Doppler-broadened Na fluorescence lineshape, (2-7) [*She, et. al, 1992*],

$$g(\nu_L,T,V) = L(\nu-\nu_L)\otimes g_{Na}(\nu,T,V) \tag{4-10}$$

where ν_L is the central frequency (i.e. the center of "mass") of the pulse laser spectrum. Since all three frequencies are within the Doppler-broadened D2 transition lineshape, (2-6) should be written as

$$\begin{aligned} R_{temp} &= \frac{g(\nu_+,T,V)+g(\nu_-,T,V)}{2g(\nu_a,T,V)} \\ R_{wind} &= \frac{g(\nu_+,T,V)-g(\nu_-,T,V)}{g(\nu_a,T,V)} \end{aligned} \tag{4-11}$$

Combined with (4-9), the two ratios become

$$\begin{aligned} R_{temp} &= \frac{\sigma_{Na}(\nu_+,T,V)+\sigma_{Na}(\nu_-,T,V)}{2\sigma_{Na}(\nu_a,T,V)} \\ R_{wind} &= \frac{\sigma_{Na}(\nu_+,T,V)-\sigma_{Na}(\nu_-,T,V)}{\sigma_{Na}(\nu_a,T,V)} \end{aligned} \tag{4-12}$$

From (4-8), we can replace σ_{Na} by the ratio of the sodium signals to the Rayleigh signals at the reference altitude, and some frequency independent term. By inserting (4-8) into the temperature and wind ratios (4-12), the frequency independent term will be cancelled out, and the temperature and wind ratios for each laser operating frequency will be represented by ratios of sodium signals that are normalized by the Rayleigh signals of the relative frequency at some reference altitude.

$$R_{temp} = \frac{\dfrac{N_{Na}(\nu_+)}{N_{Ray}(z_{ref},\nu_+)T_{up}(\nu_+)T_{down}(\nu_+)} + \dfrac{N_{Na}(\nu_-)}{N_{Ray}(z_{ref},\nu_-)T_{up}(\nu_-)T_{down}(\nu_-)}}{2\cdot\dfrac{N_{Na}(\nu_a)}{N_{Ray}(z_{ref},\nu_a)T_{up}(\nu_a)T_{down}(\nu_a)}}$$

$$R_{wind} = \frac{\dfrac{N_{Na}(\nu_+)}{N_{Ray}(z_{ref},\nu_+)T_{up}(\nu_+)T_{down}(\nu_+)} - \dfrac{N_{Na}(\nu_-)}{N_{Ray}(z_{ref},\nu_-)T_{up}(\nu_-)T_{down}(\nu_-)}}{\dfrac{N_{Na}(\nu_a)}{N_{Ray}(z_{ref},\nu_a)T_{up}(\nu_a)T_{down}(\nu_a)}} \qquad (4\text{-}13)$$

Then, given the backscattered sodium signals at altitude z, the Rayleigh scattering signals at some reference height z_{ref}, the air density at the reference range, and the sodium layer transmission from z_L to the height z (T_{up} & T_{down}), the temperature and wind for an altitude z can be iteratively calculated beginning at the bottom of the sodium layer. Both backscattered signals (Na LIF and Rayleigh) can be measured experimentally, but the sodium layer transmittances (T_{up} & T_{down}) must to be deduced from the sodium density (see 4-2 & 4-3) from z_L to the height z. According to (4-8), the sodium density can be written as:

$$n_{Na}(z,t) = \frac{N_{Na}(z,\nu_L)}{N_{Ray}(z_{ref},\nu_L)}\cdot\frac{n_{air}(z_{ref},t)\sigma_{Ray}z^2}{\sigma_{Na}(\nu_L,T,V)T_{up}(z,\nu_L)T_{down}(z,\nu_L)z_{ref}^2} \qquad (4\text{-}14)$$

Here, we assume that the extinction from air and aerosol above z_{ref} = 30 km is to be negligible. The first term of the above equation can be experimentally measured. Rayleigh and sodium backscattering cross-sections are well known, and z_{ref} is chosen as 30km. The air density for 30km is 3.2490×10^{23} /m^3) from the US standard atmosphere.

Right now, we are ready to calculate the temperature, wind and sodium density in the sodium layer. From the expression of T_{up} and T_{down} (4-2 & 4-3), at the first bin of sodium layer ($z = z_L = 70$km), both T_{up} and T_{down} equal to unity. By using (4-13), the temperature and wind ratios for the 1st range bin can be easily achieved. These two ratios are then compared to the ratios from the theoretically generated calibration curves (for example, Fig2-3) to get T and V for the 1st bin. After we know the temperature and wind for the 1st bin, we can use (4-9) to calculate the sodium backscattering cross-section, and thus to obtain the sodium density for the 1st bin by putting the σ_{Na} into (4-14) along with other known factors. This completes the calculation of the first range bin, and these results will be used for the 2nd bin calculation. This 1st bin sodium density then is used to calculate the T_{up} and T_{down} for the 2nd range bin. Once again, by using (4-13), the normalized sodium fluorescence from the 2nd bin gives the R_{temp} and R_{wind} for this altitude range. This process is iterated upward until it reaches the top of the sodium layer (defined at120km), and altitude-resolved profiles of T, V, and n_{Na} are obtained for the entire sodium layer.

4-1b Data Processing Algorithm

Each raw data file of the CSU Na-Lidar is the total photon count profile over two minutes and contains four columns. The first column is the range bin altitude, the other three are the total photon counts for each of the three operating frequencies in every range bin (150m). Based on some set diagnostic criteria, the analysis program, which was written by Professor David Krueger of CSU, will detect and eliminate the bad files, which arise from clouds, lost of laser–frequency locking, a stray trigger pulse, or other error-inducing mechanisms, so that they would not contaminate the resulting data. These diagnostic tests include trend tests, ratio tests, and minimum count tests. The trend tests

compare the total sodium counts from 83 to 105 km, also the total Rayleigh counts from 25 to 35 km, of each laser operating frequency to the mean counts of the three files before and after, and discard the files whose counts differ by more than some reasonable predefined amount (usually around 20%) from the mean value. Ratio tests compare the temperature and wind ratios, and eliminate any files that produce physically unrealistic ratios. Minimum tests get rid of the files whose counts do not meet to minimum acceptable value, and thus the files with poor signal to noise characteristics won't be counted in. There is also some test that can kick out the files with high background, which may give high optical noise. Due to the high background noise in daytime data, it is difficult to set up criteria and get rid of the bad data file, so it must be done by manual selection by displacing photo files at all three frequencies on the computer screen for visual inspection from one file to the next.

In the earlier part of this chapter, we discussed the use of Rayleigh scattering at certain altitude (30km) to determine the sodium density (4-14). Another usage of the Rayleigh scattering is for power normalization, which is used to account for the variations in transmitter power and the quite changeable transmission below 20km of the atmosphere, which may be different at the dwell times of the three operating frequencies. The sum of Rayleigh backscattering signals for each operating frequency from 20km to 40km is chosen as its normalization factor to minimize the noise introduced by division.

The integration time in this data-processing algorithm is usually one hour, for both daytime and nighttime data analysis. It could be reduced to as short as 10 minutes for nighttime data analysis, depending on the purpose of the study, for example to study the

short period gravity wave activity with an attendant increase in the uncertainties due to increased photon noise.

Before these selected, background subtracted and power normalized profiles are used to calculate the temperature and wind ratios, it is necessary to smooth them in altitude first by using a Hanning window. The FWHM of the Hanning window is 2 km for nighttime data and 4 km for daytime data. The wider daytime FWHM is due to the Faraday Filter used in the lidar receiver cutting the signal to one fifth of regular the nighttime counts. There is also a systematic error that can generate a wind-bias in the wind data analysis [White, M.A., 1999]. This wind-bias must be corrected in the data processing [Sherman, J., 2002] by using the Chirp correction. Usually, this offset is about 1-3m/s, under normal condition. But, with the PDA (Pulse Dye Amplifier) dye getting old (over 24-hour), along with the dropping of PDA output power, this wind-bias could increase to over 5m/s, so the PDA dye must be changed every 24 hours. Along with this wind-bias correction, this powerful Chirp system can also help us to monitor the locking situation of the seed beam, PDA operation status and AO alignment simultaneously in real time.

4-2 Temperature and Wind mean fields based on the diurnal cycle Observation

Due to the atmospheric tidal wave activity, the daytime and nighttime mean fields may show considerable differences in both mean values and vertical structure. Also, to study long period tidal wave activities, such as diurnal and planetary waves, long data sets (longer than 24-hour) are needed. Therefore, diurnal cycle observation is necessary not only to get the "real" mean fields, but also in the tidal wave signature detection.

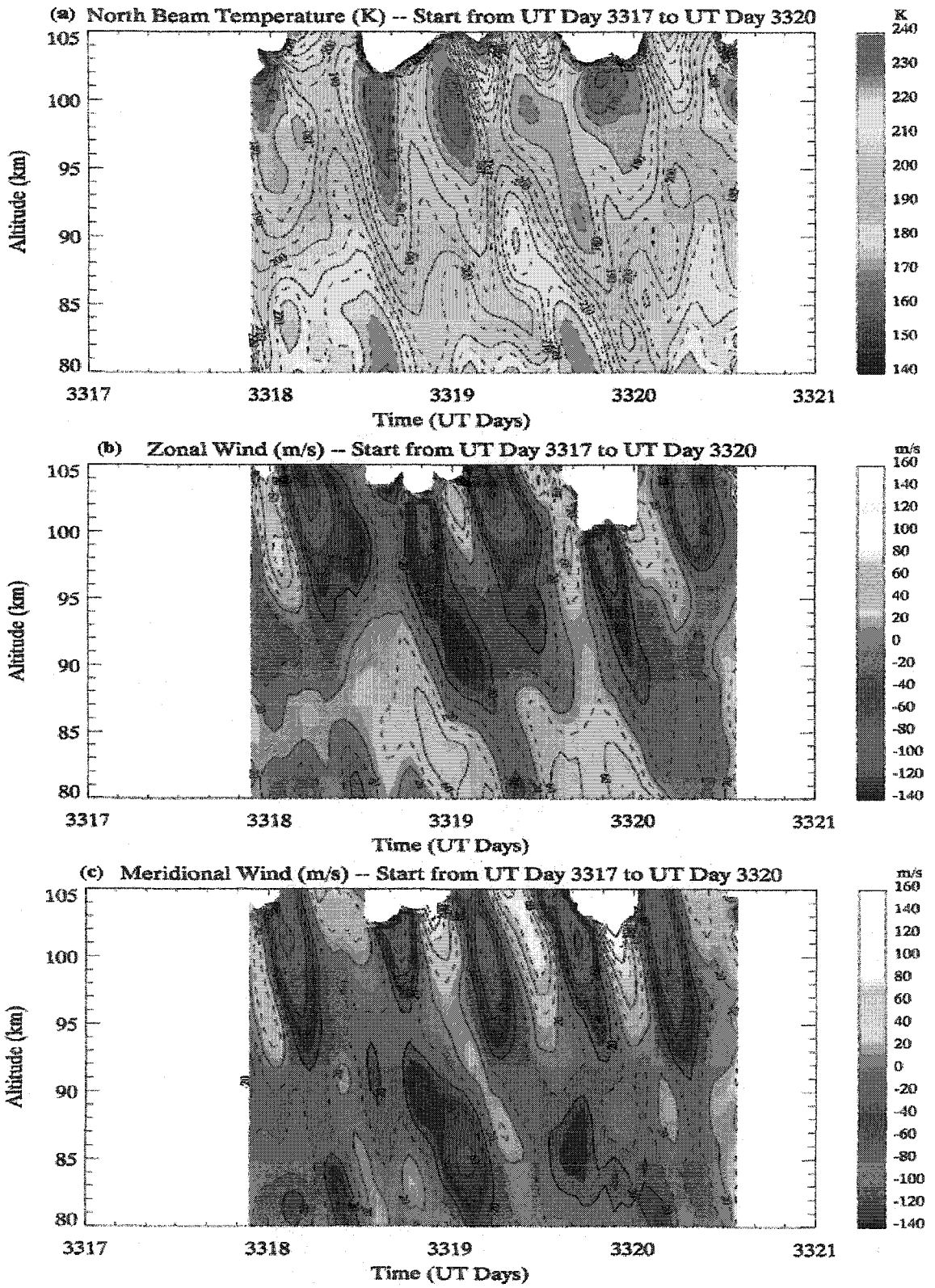

Fig 4-1 November CSU Na-Lidar Campaign From 13th to 16th (65-hour)
(a) Temperature (b) Zonal Wind (c) Meridional Wind

Most of the fluorescence lidar stations around the world are operating in the nighttime, and this makes CSU lidar diurnal cycle observation unique and valuable. With this unique diurnal observation, we can measure the daytime and nighttime mean fields (temperature, zonal and meridional winds) difference. Also we can monitor some periodic modulations of the mean fields, of particular interest are 24-hour and 12-hour periods modulations. These periodic oscillations, as mentioned before, are due to the solar thermal tidal wave activity. Sometimes, there are modulations of other period, like 10-hour or 36-hour, if the campaign is long enough, which may be related to the nonlinear interaction between tidal waves and planetary wave (2-day, 5-day and 16-day periods) [Hagan and Roble, 2001].

Fig 4-1 above shows the contours of the CSU lidar data set (temperature, zonal wind and meridional wind) from November 13th to 16th in 2003. The 12-hour and 24-hour oscillations in temperature and zonal and meridional wind fields are obvious. The white holes above 100km in some areas of the contour plots occur because of the low signal level resulting high optical noise, which is due to the Faraday filters limiting transmission for daytime observation, and thus low signal-to-noise ratio, especially near the edge of the sodium layer.

Based on these raw data above, once we separately average all the local daytime data (avg. 6-18), which means the average value from local time 6:00 to 18:00, and nighttime data (avg. 18-6)—the average value from 18:00 to 6:00 the next day, of this 65-hour campaign (Fig 4-2), the differences between daytime and nighttime mean fields can be clearly seen. The left panel in Fig. 4-2, which shows nighttime temperatures above 85km warmer than daytime temperatures by nearly 10K, may be attributable to chemical

heating at night in the mesopause region [Mlynzak and Solomon, 1993]. It is interesting to see that, not only do they differ in values, but also, especially in the wind fields, have different vertical structures. The red lines (avg.14-78) are the "real" mean values, which are the average values of the whole campaign, starting from local time 14:00 of the UT day 3317. These mean values are almost same as the constant terms in the fitting algorithm of the tidal analysis, which is studied later in this chapter.

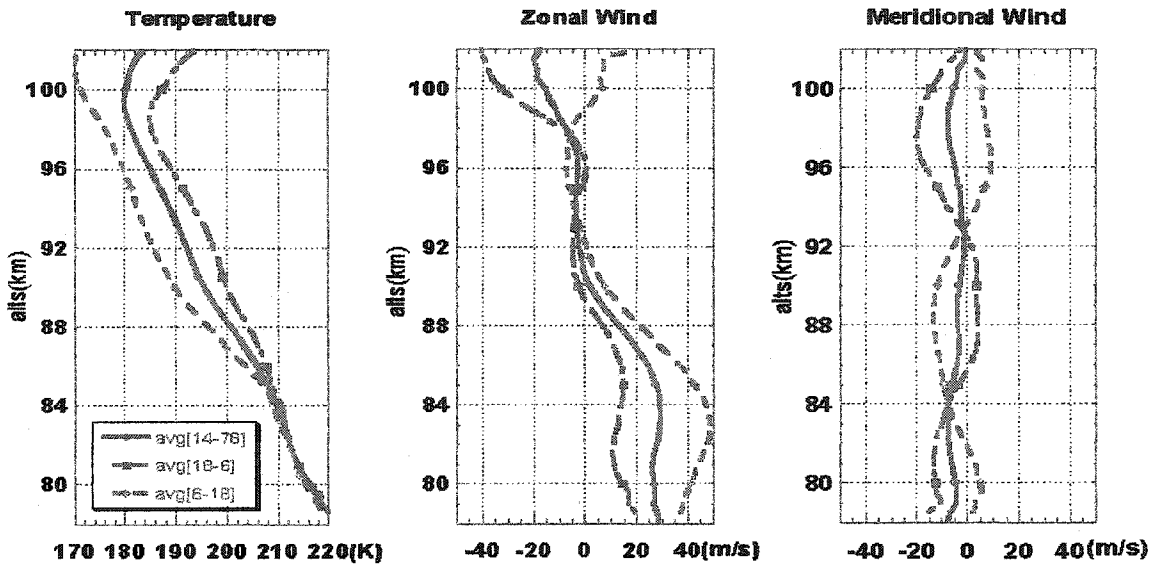

Fig 4-2 daytime and nighttime mean fields comparison (UTday 3317-3320). Red: the average value of the whole campaign (65 hours), Blue: nighttime average value, and Green: daytime average.

In short, the diurnal cycle lidar observation is quite necessary to measure the real mean fields and the tidal wave activity. For long period planetary wave (2-day, 5-day, and 16-day) study, the campaign must not be less than the wave period, which is quite difficult for ground base stations due to the weather limitation or system failure. The typical length of the CSU lidar campaign is about 2-3 days with data breaks of less than 2-hour. However, thanks to the unusual weather cooperation, the longest campaign of CSU Na-Lidar was achieved from September 21st to 29th in 2003, which gives us a great chance to study the planetary wave activity.

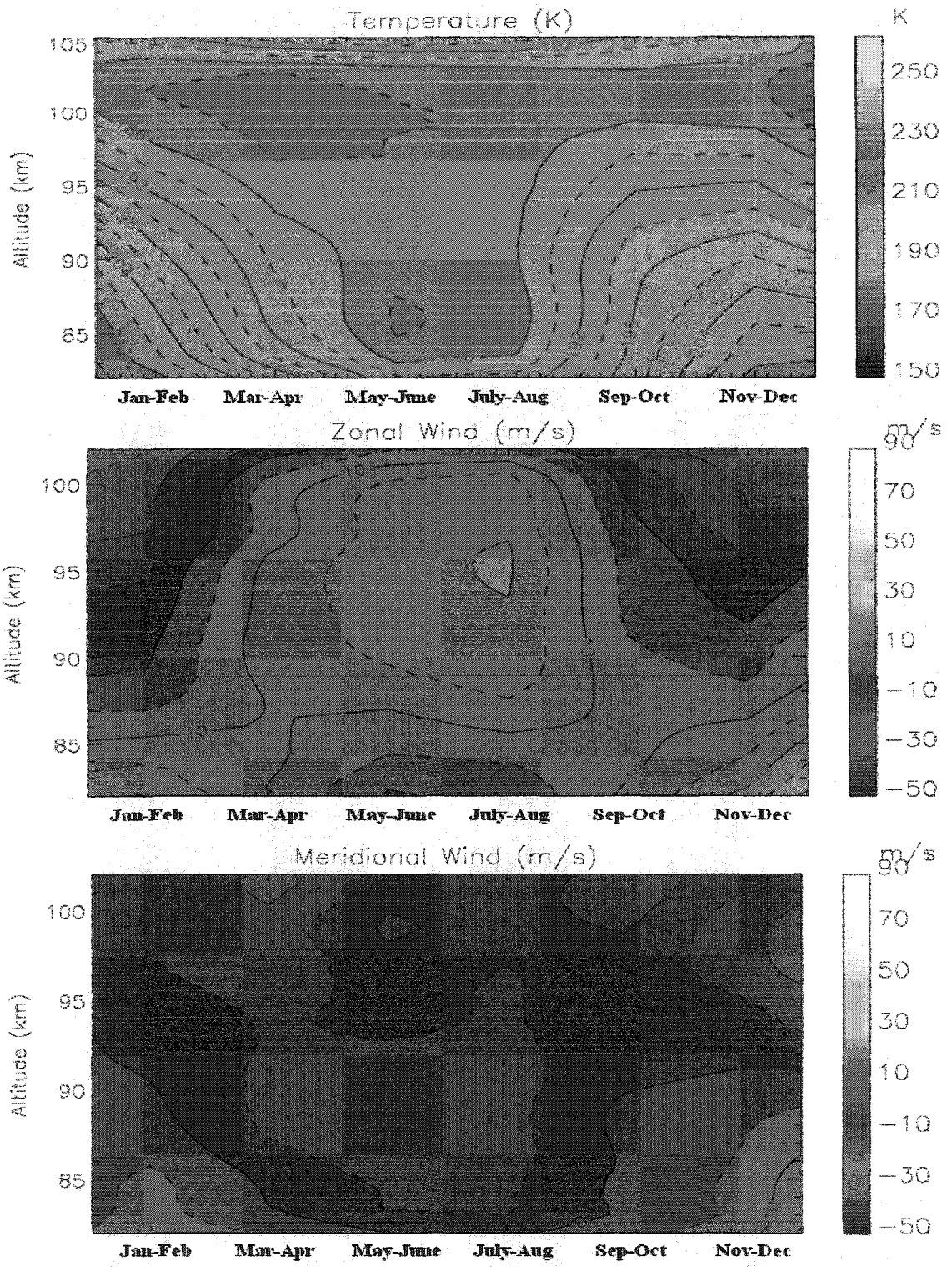

Fig 4-3 Contour plots for yearlong Bi-monthly mean fields (a): Temperature, (b):Meridional winds and (c): Zonal wind

Ever since the start of this capability of daytime observation, CSU lidar station has been running the diurnal cycle observation for about two years. This thesis mainly focuses on the data period from May 2002 to April 2003, observation of the mesopause region temperature, zonal and meridional wind. During this 12 months yearlong period, we have a total of 1491 hours observation, among which there are 659 hours daytime data. Among this yearlong data set, we choose 29 data sets of complete diurnal cycle coverage to determine the mean fields seasonal variations, which are shown below in Fig.4-3. The data after April 2003 can be used for the consistency study of this diurnal observation. This, along with the detail of the tidal wave study will be discussed in Chapter 6.

The mean temperature field shows typical mesopause transition (at lower during the summer around 84km, and higher altitude during the winter around 102km). Though 29 sets of diurnal observations are not plentiful, the altitude-month temperature contours reveal the two-level mesopause structure, first observed based on nighttime data only [She and von Zahn, 1998]. The winter eastward jet reverses at 95km, and the summertime westward jet reversal happens near 82 km. The southward flow in the summer also starts around 82km, where the summer eastward jet begins. All these results show great similarities, when they are compared with MFR (medium frequency radar) results at Platteviles station (40°N, 105°W) [Manson, 2003].

The bi-monthly diurnal-mean temperature and winds results are also shown in the Appendix 1, where the diurnal mean temperature is also compared with CSU lidar 8-year nocturnal bimonthly temperature data without Pinatubo warming effect [She, 1998, 2000]. The TIME-GCM (Thermosphere Ionosphere Mesosphere Electrodynamic General

Circulation Model) predictions are also shown along with these plots for comparison. The difference between the nocturnal temperature and diurnal mean temperature is obvious, though the variation along the altitude appears the same. These fine points will be discussed in Appendix I.

4-3 CSU Na-Lidar Tidal Analysis

The tidal waves that we are studying here are also called thermal solar tides, because they are excited by the variation in the solar heating input within a day. They include one-day period (diurnal) tide, and its harmonics, such as 12-hour (semidiurnal) tide, 8-hour (ter-diurnal) tide, and 6-hour (quad-diurnal) tide. This thesis focuses on diurnal and semidiurnal tides. Since the maximum solar heating is at (or near) ground level, tidal waves essentially propagate upwards. All the upward-propagating waves amplitudes tend to grow considerably because of the exponential density decrease with height, and the conservation of wave energy. This growth stops when dissipation dominates, or waves break (like sea waves break on the shore).

Tidal waves are global scale waves of two types. Migrating solar tides, which propagate relative to the surface of the earth with the sun and thus oscillate with the local sun time. Non-migrating tides, which do not travel with the sun. A station at one point on the earth's surface, like the CSU lidar station, which can only detect tidal-period oscillations, therefore cannot tell whether these oscillations are global (migrating or non-migrating), local or a combination of both. But, with the comparison to both GSWM models (GSWM00 & 02) we can tell the weight of the mid-latitude mesopause responses to the migrating and non-migrating tides. Although ground-based local time observations at a

fixed location provide properties of tidal oscillations, which are essential for the studies of dynamics and chemistry imbedded in the global models, observations at a number of locations with radar, lidar, other optical instruments, and cooperation with satellites (such as TIMED--The Thermosphere, Ionosphere, Mesosphere, Energetics and Dynamics) observations will reveal the longitude and latitude dependence of the tidal oscillations.

The dynamic behavior during a given day as observed from a single station may be described in terms of three related field variables: temperature, zonal and meridional winds as a function of altitude and time. With lidar observation covering multiple full diurnal cycles with hundreds of hours of data, we can decompose our hourly data over the campaign into a sum of mean, amplitude and phase of the tidal components and a residual, representing variations with all periods shorter than one day [She, 2004]:

$$\Phi^{T,U,V}(z,t) = \overline{\Phi^{T,U,V}} + \sum_j A_j^{T,U,V}(z)\cos\left[\frac{2\pi j}{24}(t-\theta_j^{T,U,V})\right] + R^{T,U,V}(z,t) \qquad (4\text{-}15)$$

In this manner, each term is independent from other as an observed quantity. Even under this assumption, the mean state and tidal amplitudes and phases will still vary from one day to the next as they are modulated by longer period planetary waves or shorter period gravity wave breaking. This interaction, on one hand, may perturb the observed mean state and tidal amplitudes and phases, and, on the other hand, produce new periods via nonlinear interaction, such as 10-hour and 16-hour waves.

Because the air density is decreasing as the altitude increase, and most of the tidal sources are in the lower atmosphere (H_2O in the troposphere, O_3 in the stratosphere), the

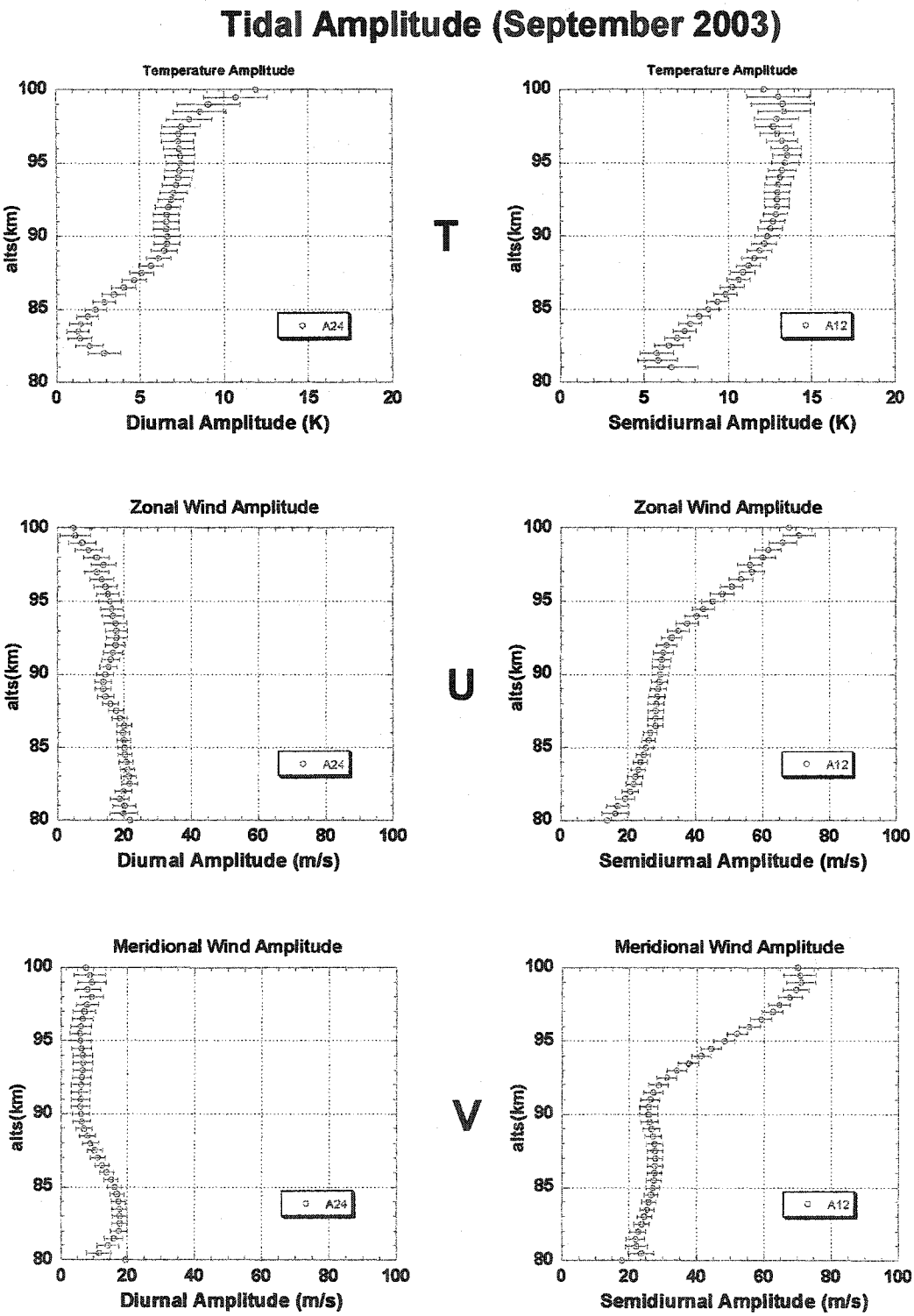

Fig 4-4a Tidal Amplitude (Diurnal-left side and semidiurnal-right side) results for September 2003 (T, U, V represent Temperature, Zonal wind and Meridional wind respectively)

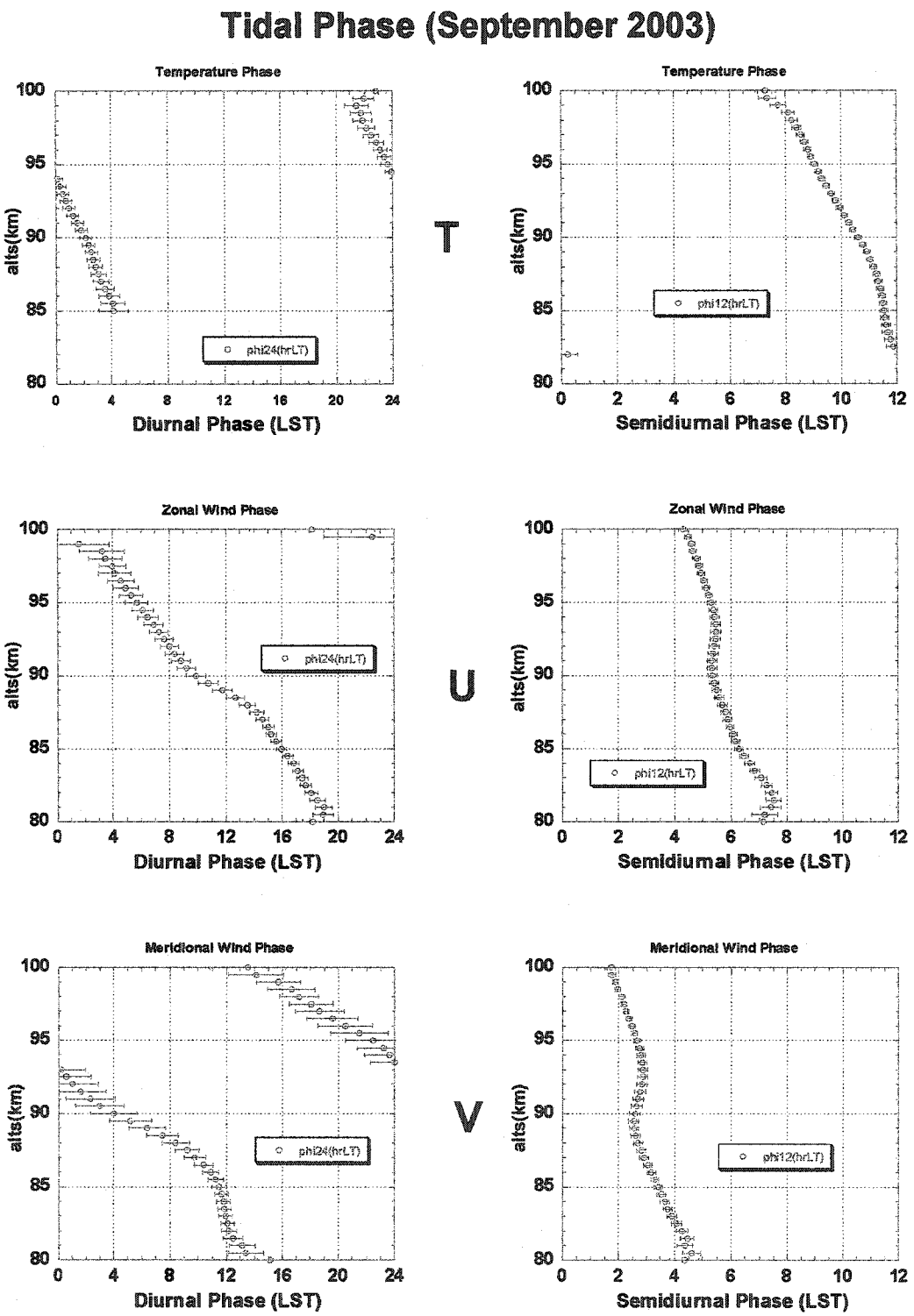

Fig 4-4b Tidal Phase (Diurnal-left side and semidiurnal-right side) results for September 2003 (T, U, V represent Temperature, Zonal wind and Meridional wind respectively). The downward phase progression is typical of tidal wave behavior.

wind and temperature tidal amplitudes are expected increase with the altitude, and the relative tidal phases would be downward progressing. Details of the tidal classical theory will be discussed in Chapter 5. Here, some tidal analysis results are presented for both diurnal and semidiurnal tides.

The plots above show the tidal analysis results of September 2003. In this September campaign, continuous nine-day lidar data was collected, and from statistical point of view, it should be long enough to represent the tidal perturbation behavior of September. The error bars in the tidal amplitude results are the standard deviation between the lidar data (temperature, winds) and the tidal fitting (4-15). The upward propagating waves are quite obvious, and the increasing amplitudes, downward phase progression agree with the tidal theory. But the Zonal and Meridional wind diurnal amplitudes appear to be constant with the altitude, which is not like the theoretical prediction. This may due to some interaction between tides and wave, which is less studied so far.

Along with the linear fit algorithm of the tidal analysis, we also run a frequency identification program called Lomb normalized periodogram (spectral power as a function of angular frequency), which is a special spectral analysis method of unevenly sampled data, to measure the significance of each possible tidal wave [William H. Press, et.al.]. This spectral power is identical to that one obtains by estimating the harmonic content of a data set, at a given frequency ω, by linear least squares fitting to the model.

$$h(t) = A\cos\omega t + B\sin\omega t \qquad (4\text{-}16)$$

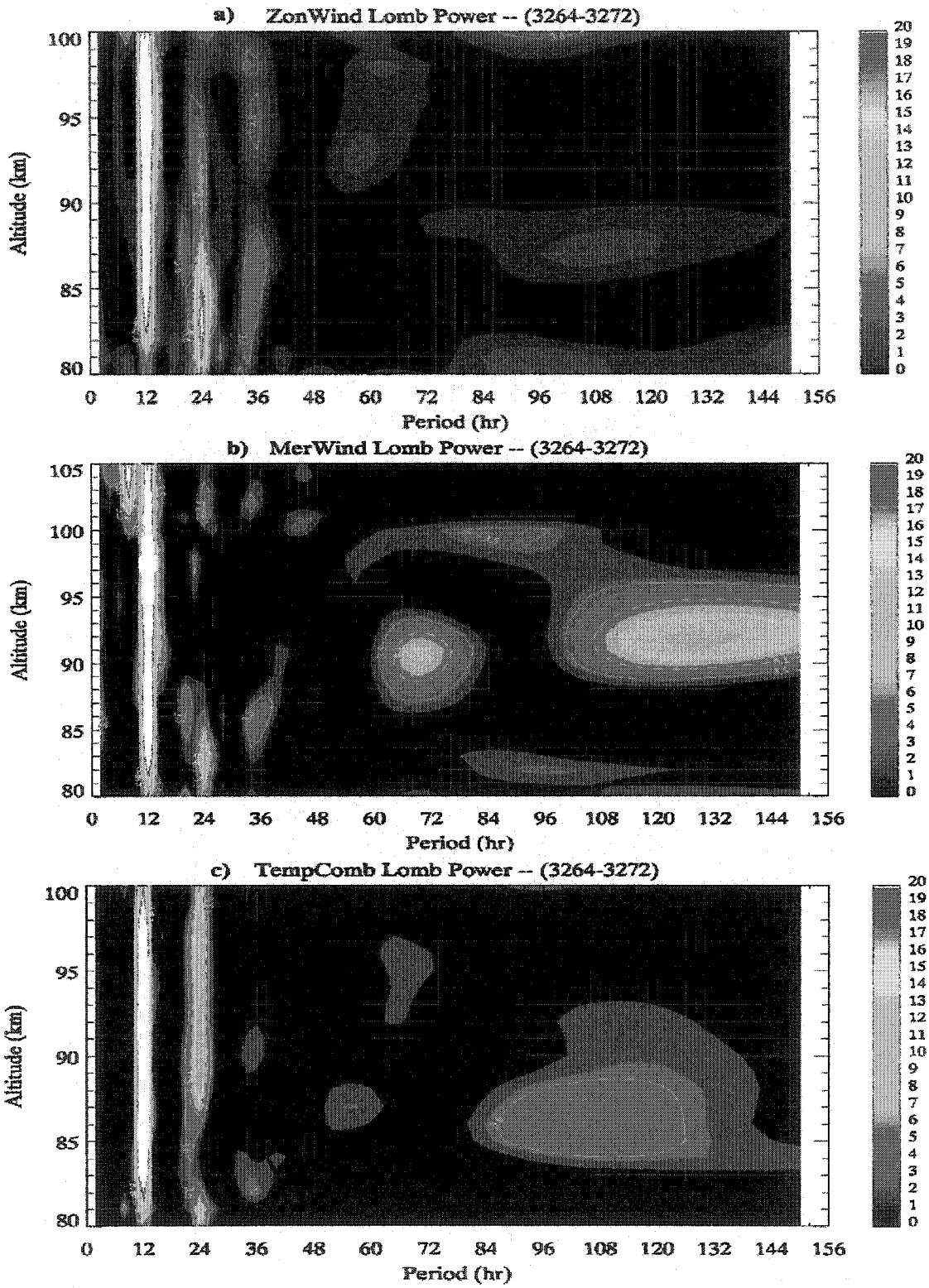

Fig 4-5 Contour plots for the Lomb periodogram of the September Campaign (Sep 21st – 29th, 2003) for (a) the Zonal wind field (b) the Meridional wind field and (c) Temperature

The Lomb method evaluates data, and sines and cosines, only at times t_i that is actually measured, so it does not need interpolation to fill in the missing data gaps, which always occurs in practice for ground based atmospheric observations. It gives the same results as the traditional FFT method (Fast Fourier Transforms), if the data set is continuous without break over an integral number of periods. Because it assigns a weight for the data on a "per point" basis instead of on a "per time interval" basis, it renders results superior to FFT method when dealing with uneven sampling, which can generate serious error in the latter. To understand the detail of this Lomb periodogram, see: Numerical Recipes in C-The Art of Scientific Computing, 2nd Edition. Whenever we run this Lomb calculation on our diurnal cycle data set, the diurnal and semidiurnal period signals always give the stronger power than other periods. Figure 4-5 is an example of this Lomb periodogram.

The contour plots above shows the Lomb periodograms for the 2003 September campaign. In Fig 4-5b, the huge hump peaking at 93km with 132-hour period is the "alias" due to the limited length of the campaign, even though this campaign lasted over 200 hours. In both of these plots, the semidiurnal tide is so strong that it even saturated the set color bar. The diurnal tide is also quite obvious and is the second significant wave. This (semidiurnal tides and relative weaker diurnal tides) is consistent with the tidal theoretical prediction for mid-latitude region, which is presented in Chapter 5. There are also some 16-hour and 36-hour periods showing up in both winds and temperature fields, possibly due to the wave-tide nonlinear interaction mentioned earlier. The most interesting phenomenon in the meridional wind Lomb contour plot is the significant 72-hour (3-day) wave, which is really unusual for this latitude. The cause of this 3-day wave

is beyond our knowledge right now. Cooperation with the atmosphere theorists is under way, and hopefully, will some insight of this mysterious atmosphere.

Since CSU Na-Lidar observation is limited by weather condition and sometimes system failure, only a few days' observations can be achieved in one month, and it could not possibly represent the climatological tidal behavior for this month. To minimize this statistical error, and also be able to capture the seasonal tidal variations, in this dissertation, we will present the bi-monthly tidal analysis (Diurnal diurnal and semidiurnal) and compare with tidal models (GSWM00&02, and TIME-GCM 2002 simulation). Below is a list of the total number of hours of the first yearlong diurnal cycle data set and the complete diurnal cycle data. The blue column represents the total number of observation hours, and the brown one represents the complete diurnal cycle observation hours.

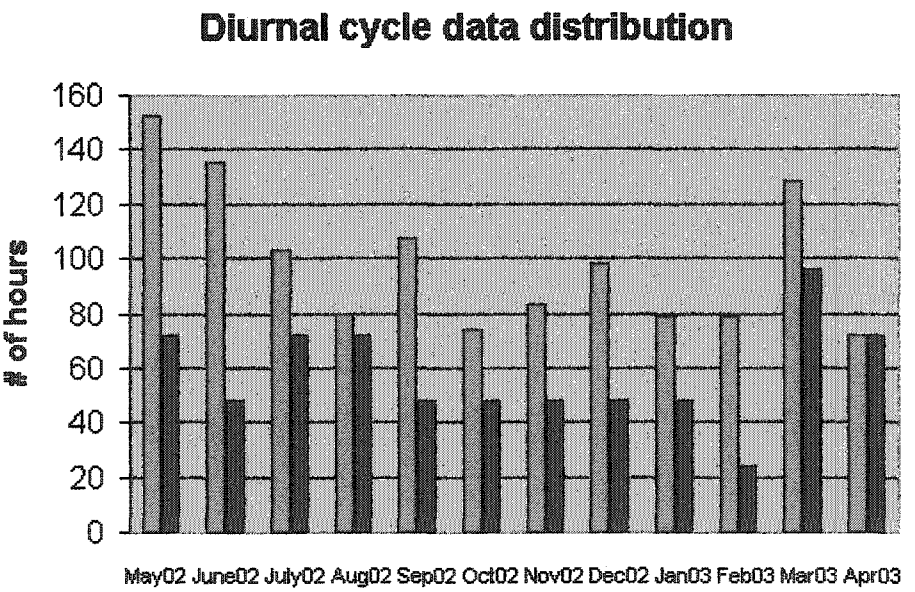

Fig 4-6 Diurnal cycle data distribution of the first yearlong data set of CSU Na-lidar: a total of 1,491 hours observation (Blue bar), in which there is 29 complete diurnal cycle data sets (Brown bar)

Reference:

Gardner, C.S., Sodium Resonance Fluorescence Lidar Applications in Atmospheric Science and Astronomy., *Proceedings of the IEEE*, Vol. 77, NO. 3, March 1989.

Hagan, M. E., Roble, R. G., Modeling diurnal tidal variability with the National Center for Atmospheric Research thermosphere-ionosphere-mesosphere-electrodynamics general circulation model. *J. Geophys. Res. 106*, 24, 869-624,882, 2001.

Manson, A. H. and C. E. Meek. Longitudinal and Latitudinal Variations in Dynamic Characteristics of the MLT (70 - 95 km), *J. Geophys. Res.* Vol. 108, No. D13, 4398, 2003.

She, C. Y., J. R. Yu, H. Latifi, and R. E. Bills, High-Spectral-Resolution Fluorescence Lidar for Mesopheric Sodium Temperature Measurements. *Appl. Opt. 31*, 2095-2106, 1992.

She, C. Y., S. W. Thiel and D. A. Krueger, Observed episodic warming at 86 and 100 km between 1990 and 1997: Effects of Mount Pinatubo eruption, *Geophys. Res. Lett., 25*, 497-500, 1998.

She, C. Y., S. S. Chen, Z. L. Hu, J. Sherman, J. D. Vance, V. Vasoli, M. A. White, J. R. Yu, and D. A. Krueger, Eight-year climatology of nocturnal temperature and sodium density in the mesopause region (80 to 105 km) over Fort Collins, CO (41°N, 105°W), *Geophys. Res. Lett.*, 27, 3289 - 3292, 2000.

Sherman, J, PhD dissertation: Mesopause Region Thermal and Dynamical Studies Based on Simultaneous Temperature, Zonal and Meridional Wind Measurements with Upgraded Sodium Fluorescence Lidar. Colorado State University, 2002.

White, M. A., PhD dissertation: A Frequency-agile sodium Lidar for the Measurement of Temperature and Velocity in the Mesopause Region, Colorado State University, 1999.

William H. Press, Saul A. Teukolsky, Wiliam T. Vetterling, Bran P. Flannery, Numerical Recipes in C – *The Art of Scientific Computing, Second Edition. 13.8, 1992.*

Yu, Jirong, PhD dissertation: A sodium wind/temperature lidar and observed mesopause thermal structure over Ft. Collins, CO, Colorado State University 1994.

Chapter 5 Tidal Wave Theory

5-1 Introduction of Solar Tide

Atmospheric solar tides are global-scale waves with periods that are harmonics of a solar day, such as diurnal tides (24-hour) and semidiurnal tides (12-hour). They can be excited by the absorption of solar radiation, by large-scale latent heat release associated with deep convective activity in the troposphere, and can be modified by nonlinear interactions between global-scale waves [e.g., Miyahara and Miyoshi, 1997; Hagan and Roble, 2001; McLandress, 2001], by interaction between gravity waves and tides [e.g., McLandress and Ward, 1994], and to a lesser extend by the gravitational pull of the sun. Its signatures can be easily seen in temperature, wind, density, and pressure in the mesopause region.

There are two major sources, which drive the migrating tides: The UV (Ultra Violet radiation) energy, which is absorbed periodically by stratospheric O_3 and released as heat, and IR (Infer Red radiation) energy absorbed by tropospheric H_2O. Another thermal driver is the latent heat, which is stored in water vapor and transported by complex meteorological activity, to be released again in other regions of the globe when the vapor liquifies. Because of its longitude dependence, this source is less important influence for migrating tides, and more significant for non-migrating tides [Hagan and Forbes, 2002].

Tidal damping may come from many strong and weak mechanisms. Other short-term or small-scale waves that originate by winds blowing over topography, convection and

wind shear etc. [Fritts, 2003], called gravity waves, tend to disrupt tidal components by causing turbulence, and at times accelerate the air motion along with the global-scale tide. Tides and gravity waves increase in amplitude with altitude exponentially due to the decreasing density of the atmosphere. Between 80-100km, at the mesopause, gravity waves become large enough to interfere with diurnal tides by "dragging" the background atmosphere to the phase speed of the tide, and by causing eddy flows that disrupt energy propagation.

Above about 90-100km in the lower thermosphere, the decreasing density of the air causes wave motion to be dominated by molecular diffusion rather than fluid flow, decreasing the efficiency of energy transfer, and further damping the tides. Above the thermosphere, tides are dissipated by the radiation of energy into space (Newtonian cooling), and tidal winds accelerate charged particles in the ionosphere (ion drag).

Two components of solar tides are defined: migrating tides, which propagate with the apparent motion of the sun (westward), and non-migrating tides, which can be standing, or propagate either westward of eastward. By far, the largest components are migrating tides, and the existing evidence suggests these to be the dominant wave components in the mesosphere and lower thermosphere [Forbes, 1995].

5-2 Classical Tidal Wave Theory

The general dynamical equations governing atmospheric motions are nonlinear and contain a variety of dissipative terms. These equations are often linearized, leading to coupled equations describing mean states and perturbations of the atmosphere. If the

mean or background atmosphere is assumed to be vertically stratified, the mean winds are zero and the equations for the mean states and perturbations are decoupled. Assumption of an isothermal background atmosphere leads to further simplification without loss of instructional value. The linearized equations for perturbations on a spherical isothermal atmosphere are [Chapman and Lindzen, 1970]:

X momentum:

$$\frac{\partial u}{\partial t} - 2\Omega v \sin\theta + \frac{1}{a\cos\theta}\frac{\partial \Phi}{\partial \phi} = 0$$

Y momentum:

$$\frac{\partial v}{\partial t} + 2\Omega u \sin\theta + \frac{1}{a}\frac{\partial \Phi}{\partial \theta} = 0$$

Energy:

$$\frac{\partial}{\partial t}\left(\frac{\partial \Phi}{\partial z}\right) + N^2 w = \frac{\kappa J}{H}$$

Continuity:

$$\frac{1}{a\cos\theta}\left[\frac{\partial u}{\partial \phi} + \frac{\partial}{\partial \theta}(v\cos\theta)\right] + \frac{1}{\rho_0}\frac{\partial}{\partial z}(\rho_0 w) = 0$$

(5-1)

Where

u	eastward velocity
v	northward velocity
w	upward velocity
Φ	perturbation geopotential
N^2	buoyancy Frequency Square (equals to $\kappa g/H$)
Ω	angular velocity of Earth
ρ_0	basic state density, which is proportional to $exp\ [-z/H]$
z	altitude
ϕ	longitude
θ	latitude
κ	$R/C_p \approx 2/7$
J	heating per unit mass

a	radius of Earth
g	gravity acceleration
H	constant scale height
t	time

Assume the perturbations consist of longitudinally propagating waves of zonal wavenumber s and angular frequency σ:

$$\{u, v, w, \Phi\} = \left\{\hat{u}, \hat{v}, \hat{w}, \hat{\Phi}\right\} \exp\left[i(s\phi - \sigma t)\right] \tag{5-2}$$

where

s is zonal wavenumber (s = 0, 1, 2 ....)

$\sigma = 2\pi/T$; following Forbes [1995], S is taken to be always positive, we indicate direction of propagation by the signs of frequency ($\sigma > 0$ eastward propagating waves; $\sigma < 0$ westward propagating waves)

Though these equations, neglecting background winds, meridional and zonal temperature gradients, and dissipative terms, are over-simplified, solving the simplified equations can provide insight into many tidal wave phenomena. In this simplified case, separable solutions do exist, and the problem can be reduced to an eigen-value problem. Then the separable solution for Φ in z and θ is

$$\hat{\Phi} = \sum_n \Theta_n(\theta) G_n(z) \tag{5-3}$$

Also, the thermal excitation can be expand to

$$\hat{J} = \sum_n \Theta_n(\theta) J_n(z) \tag{5-4}$$

The differential equations are then converted to dimensionless form, with solutions for the horizontal winds given by

$$\hat{u}(\theta,z)=\frac{\sigma}{4\Omega^2 a}\sum_n U_n(\theta)G_n(z)$$
$$\hat{v}(\theta,z)=\frac{-i\sigma}{4\Omega^2 a}\sum_n V_n(\theta)G_n(z) \qquad (5\text{-}5)$$

where

$$U_n=\left(\frac{1}{f^2-\sin^2(\theta)}\right)\left(\frac{s}{\cos(\theta)}+\frac{\sin(\theta)}{f}\frac{d}{d\theta}\right)\Theta_n(\theta)$$
$$V_n=\left(\frac{1}{f^2-\sin^2(\theta)}\right)\left(\frac{s\cdot\tan(\theta)}{f}+\frac{d}{d\theta}\right)\Theta_n(\theta) \qquad (5\text{-}6)$$

and $\Theta_n(\theta)$ are Hough functions, which are the solutions to LaPlace's tidal equation. We also have defined: $f=\sigma/2\Omega$.

For a given s, the LaPlace's tidal equation describes the Hough function behavior in the meridional direction, and it has the form of

$$\frac{d}{d\mu}\left[\frac{(1-\mu^2)}{(f^2-\mu^2)}\frac{d\Theta_n}{d\mu}\right]-\frac{1}{f^2-\mu^2}\left[\frac{-s\left(f^2+\mu^2\right)}{f\left(f^2-\mu^2\right)}+\frac{s^2}{1-\mu^2}\right]\Theta_n+\left[\frac{(2\Omega a)^2}{gh_n}\right]\Theta_n=0 \qquad (5\text{-}7)$$

in which $\mu = sin(\theta)$, and h_n are the eigenvalues (unit: meters), referred to as atmospheric equivalent depths. The Hough function form a complete, orthogonal basis set of solutions over θ and satisfy the requirement of boundary condition at the poles, which require that the Hough functions go to zero at the poles.

On the other hand, the vertical structure equation, which yields the z-dependent $G_n(z)$, has the form of

$$i\sigma H\left[\frac{1}{\rho_0}\frac{\partial}{\partial z}\rho_0\frac{\partial}{\partial z}G_n\right]+\frac{1}{\rho_0}\frac{\partial}{\partial z}(\rho_0\kappa J_n)=-\frac{i\sigma\kappa}{h_n}G_n \qquad (5\text{-}8)$$

and $G_n(z)$ has the form of $\sim exp(z/2H)\times exp(i\alpha_n z)$. It associated with the Hough function $\Theta_n(\theta)$ with the same mode index, n, by

$$\alpha_n^2 = \frac{\kappa H}{h_n} - \frac{1}{4}. \qquad (5\text{-}9)$$

When $\alpha^2_n > 0$, $G_n(z)$ is an upward propagating mode, in which the wave energy propagates upward into the atmosphere. Otherwise, it is trapped near the height of excitation, where $\alpha^2_n < 0$, and the energy decays along the altitude. Thus, for each pair of (s, n), there exist an eigensolution, representing one normal mode, and the negative h_n and related n index must represent a trapped mode. These modes of waves perturb and modulate the temperature and wind in the atmosphere.

Diurnal tidal modes (24-hour period tidal wave) have s = 1 and $\sigma = \Omega$, and the semidiurnal tidal modes (12-hour period tidal wave) have s = 2 and $\sigma = 2\Omega$. Study shows that the diurnal (1, -2) mode receives the greatest thermal input, while the semidiurnal (2, 2) propagating mode receives the biggest input of all semidiurnal modes. [Forbes, 1984]

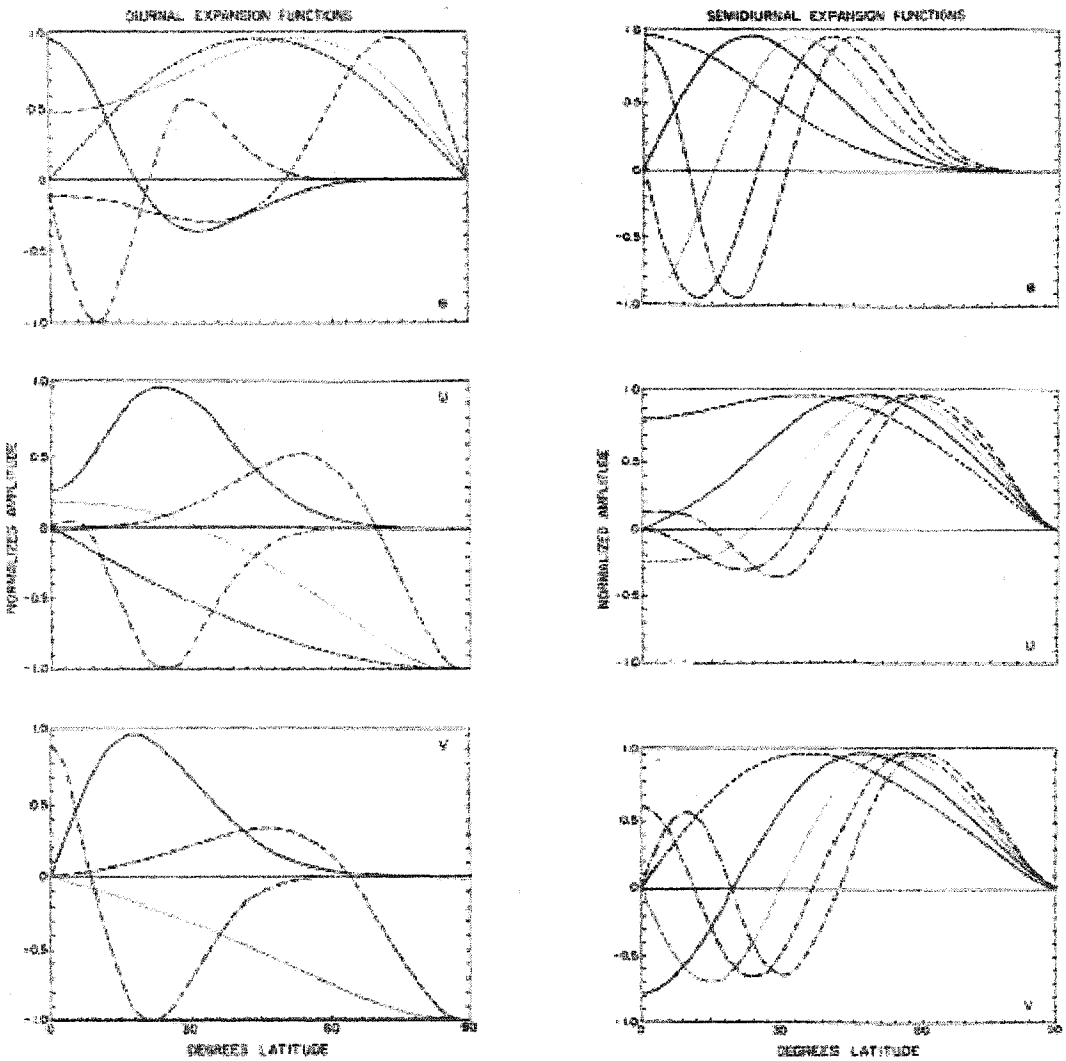

Fig.5-1 Normalized expansion functions for the solar diurnal (left) and semidiurnal (right) tide. Top: Hough function. Middle: Eastward wind expansion function. Bottom: Northward wind expansion function. For diurnal tide (left): Solid line, (1, 1); dot, (1, -1); dashed-double dot, (1, 2); dashed-dot, (1, -4). For semidiurnal tide (right): Dashed line, (2,2); solid, (2,3); dotted (2,4); dashed-dot, (2,5); dashed-double dot, (2,6). From Forbes [1982].

Therefore, they are the dominant modes of their relative classes. Below (Fig.5-1) is the plot of normalized expansion functions for the solar diurnal (left) and semidiurnal (right) tide of Hough function, Zonal wind and Meridional wind.

By studying the Hough function expansions (Fig.5-1), the diurnal propagating modes ($h_n > 0$) have amplitudes concentrated at low latitudes and the trapped modes ($h_n < 0$) have amplitudes concentrated at higher latitudes. Due to the lack of absorbing molecules in the mesopause region (Fig.5-2), the propagating diurnal tides show dominant influence at low latitude, whereas, at mid-latitude, the diurnal tides are relatively weaker. The propagating semidiurnal tidal modes, however, have large amplitudes between 30-60° latitudes. This explains why, at mid-latitude, the temperature and winds measurements of the mesopause region show dominant semidiurnal tides effects.

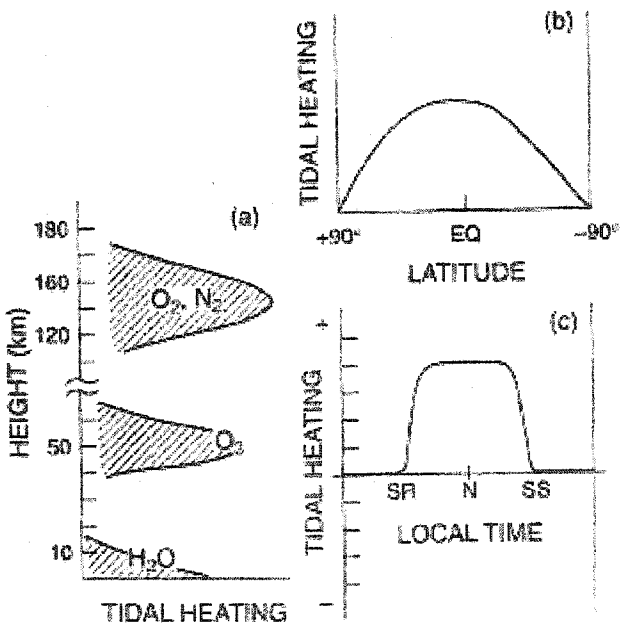

Fig.5-2 Schematic of (a) vertical (left), (b) latitudinal (top), and (c) diurnal (bottom) variations in tidal heating. From Forbes [1995].

Another important characteristic of the solar tide is their upward energy propagation, which is consistent with the heating source below and upward propagating group velocity, also called radiation condition. Due to the air density exponentially decreasing along the altitude, the tidal wave amplitude would increase with the altitude, with related downward progression of the vertical tidal wave phase, due to atmospheric dispersion relation [Forbes, 1995].

5-3 Global Scale Wave Model (GSWM00&02)

Some basic features of the diurnal and semidiurnal tidal components can be described by classical tidal theory [e.g. Chapman and Lindzen, 1970], but for a more quantitative understanding, a realistic background atmosphere as well as an appropriate parameterization of tidal forcing and dissipation have to be taken into account. Based on the classical linear tidal modeling [Chapman and Lindzen, 1970], scientists started to describe modification to those solutions that are associated with non-classical effects, including those attributable to zonal mean zonal winds, latitudinal temperature gradients, and dissipation [Kato, 1980; Volland, 1988; and Forbes, 1995]. In all those non-classical models, the Global Scale Wave Model (GSWM) is a two-dimensional, linearized, steady state numerical tidal and planetary wave model, which extends from the ground to the thermosphere [Hagan et al., 1993, 1995, 1999, and 2001]. The GSWM tidal and planetary wave predictions are solutions to the linearized and extended Navier-Stokes equations for perturbation fields with characteristic zonal wave numbers and periodicities that are specified along with the zonal mean background atmosphere.

From the ground to the upper thermosphere GSWM-00 background temperatures and densities are specified by the MSISE90 empirical model [Hedin, 1991]. Below ~20km the background winds are from the semi empirical model of Groves [1985, 1987], but the strato-mesospheric jets and mesopause region winds are based upon Upper Atmosphere Research Satellite (UARS) High Resolution Doppler Interferometer (HRDI) climatologies [Hagan et al., 1999]. Above ~125km, zonal mean zonal winds are from the 1993 horizontal wind model [Hedin et al., 1991, 1996].

The GSWM includes tidal forcing schemes, which account for all known sources of thermal excitation. The tropospheric H_2O absorbs solar radiation in the near infrared (IR). Stratospheric and lower mesospheric O_3 absorbs solar radiation in the ultraviolet (UV), and lower thermospheric O_2 absorbs solar radiation in the Schumann-Runge bands and continuum. This thermal excitation gives rise to both evanescent (trapped) and propagating components of the diurnal and semidiurnal tide from the ground through the thermosphere.

In the GSWM00 model configuration, only migrating sources excited by the absorption of solar radiation are specified. These include the tropospheric IR heating parameterization based on Groves [1982], which is only available for (January, April, July, October), representing 4 seasons. The GSWM00 model uses latitude and altitude-dependent ozone concentrations and the parameterization scheme of Strobel [1978] to calculate ozone (UV) forcing in the stratosphere and lower mesosphere. The same scheme and MSISE90 molecular oxygen densities account for the absorption of radiation in the Schuman-Runge band and continuum in the lower thermosphere.

GSWM02 model, available in 2002, is an extension of GSWM00. It includes another important tidal forcing-latent heating associated with deep convective activity (rain drop formation in the deep clouds) in the troposphere, which is the most significant non-migrating tidal source. Hagan and Forbes (2002, 2003) discuss the details of this non-migrating tidal source and its effects on the diurnal, semidiurnal tides.

Tidal wave increases its amplitude when it propagates upward because of the decreasing of the atmospheric density. However, wave dissipation effects become important in the middle and upper atmosphere. Both GSWM00 and GSWM02 also consider the tidal dissipation occurring throughout the atmosphere resulting from the three effects briefly discussed below.

1) Gravity waves deposit momentum in the mesosphere and lower thermosphere as they grow and break. Their net effect is to "drag" or "stress" the winds at these altitudes. There are significant mean wind and diurnal tidal effects, due to the comparatively short vertical wavelength of the diurnal tide.

2) The turbulence generated by breaking or dissipating gravity waves causes diffusion effects, which are felt by all tidal fields.

3) Newton cooling, latitude-dependent thermal conductivity, and ion drag effects are also accounted for.

Since migrating solar tides are dominant and have been studied for quite a long time, we briefly discuss some of their basic features. There are diurnal (24-hour) tide, semidiurnal (12-hour) tide, terdiurnal (8-hour) tide and quadiurnal (6-hour) tide etc. Most of the

shortter period tidal waves are weak and only the diurnal and semidiurnal tides will be focused in this thesis. The main thermal forcing for diurnal migrating solar tide, are IR and UV heatings. The largest (smallest) diurnal tidal amplitudes result from calculations that include IR (UV) forcing only. However, because the diurnal components associated with these sources are out of phase (i.e., shifted by ½ the tidal period), their combined effect results in diurnal tidal amplitudes that are, for the most part, the difference between the two (Fig. 5-2). Of course, these tidal sources also have strong seasonal variability. For

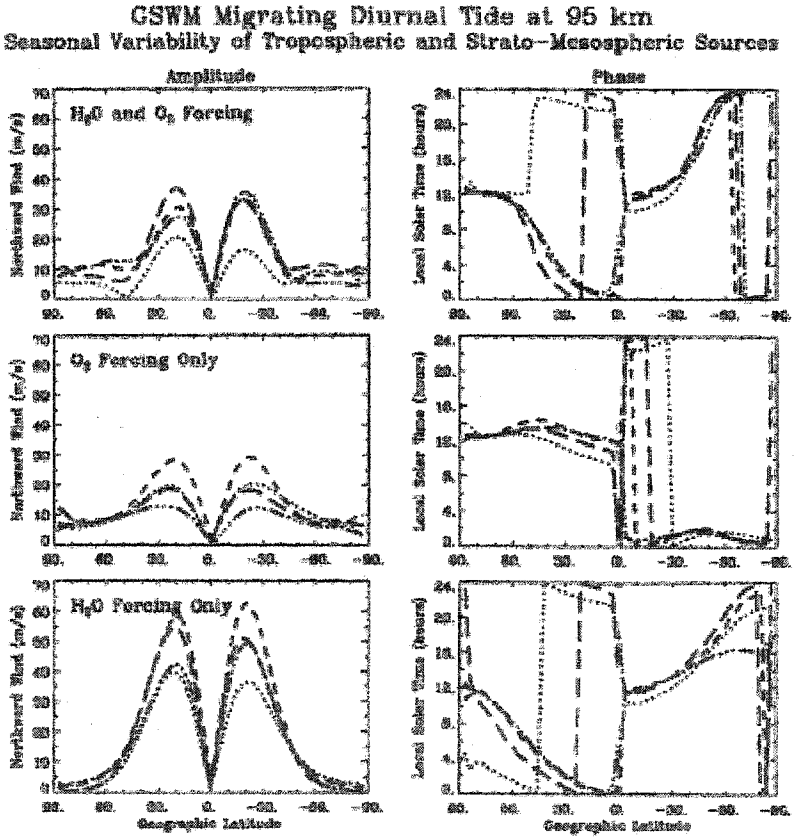

Fig. 5-3. (left) Amplitude in m/s and (right) phase in local solar hours of the meridional wind component of the diurnal tide at 95 km for GSWM runs forced (bottom) by H_2O only, (middle) by O_3 and O_2 only, and (top) with both sources during January (dotted curve), April (short-dashed curve), July (dotted-dashed curve), and October (long-dashed curve). From Hagan [1996].

example, the H_2O source produces amplitudes of about 60m/s near 100km during April and October, but O_3 and O_2 forcing produces peak amplitudes some 40% smaller during October as compared with April. Therefore the total tidal field is weaker during April. It interacts with Gravity Waves in the Mesosphere and this further reduces its amplitude in the lower Thermosphere. The peak amplitude occurs in middle to low latitudes, which is also seasonal dependent as shown in Fig. 5-3 for 95km. The vertical wavelength of the diurnal is ~ 25km.

Compared with diurnal migrating solar tide, semidiurnal tide has smaller perturbations (tidal amplitudes) in Mesosphere, but longer wavelength (usually ~ 50km). Although the semidiurnal tidal sources are same as diurnal tide, their contributions are lot more complicated (Fig5-4), mainly due to the phase difference between IR and UV forcings, which vary depending on the season. While the strongest MLT signatures are driven by O_3 and O_2 forcing, the effects of H_2O on both amplitude and phase are profoundly different between seasons. For example, below about 105km, amplitudes resulting from IR heating are larger than those of UV. However, the associated phases are within 2 hours of each other during January and approach 6-hour differences during July. The net effect is that the components add (subtract) during January (July). O_3 and O_2 forcing dominates the MLT response above 105-110km. Its peak amplitude occurs at middle to high latitude, also seasonal dependent. Its highest amplitude should be found in lower thermosphere (115 to 120km). Of course, the amplitude will eventually decreases eventually as the altitude increase, due to the tidal force dissipation, such as ion drag and thermal diffusion in the thermosphere.

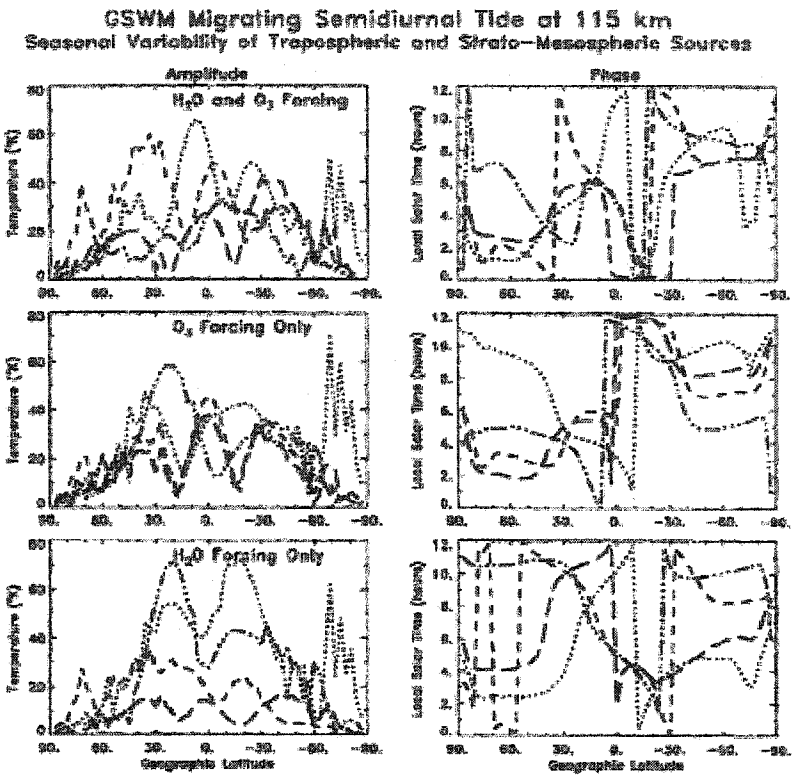

Fig.5-4. (left) Amplitude in Kelvins and (right) phase in local solar hours of the temperature component of the semidiurnal tide at 115km for GSWM runs forced (bottom) by H_20 only, (middle) by O_3 and O_2 only, and (top) with both sources during January (dotted curve), April (short-dashed curve), July (dotted-dashed curve), and October (long-dashed curve). From Hagan [1996].

5-4 Thermosphere Ionosphere Mesosphere Electrodynamic General Circulation Model (TIME-GCM)

Thermosphere Ionosphere Mesosphere Electrodynamic General Circulation Model (TIME-GCM) is an extension of the TGCM's: Thermospheric General Circulation Models [*Dickinson et al.*, 1981], developed by NCAR (National Center for Atmospheric Research) [*Roble and Ridley*, 1994]. It is a three-dimensional, time-dependent model of the earth neutral atmosphere. The model uses a finite differencing technique to obtain a self-consistent solution for the coupled, nonlinear equations of hydrodynamics, thermodynamics, and continuity of the neutral gas and for the coupling between the

dynamics and the composition. The output of the TIME-GCM consists of 30 fields on a three-dimensional latitude, longitude, and pressure grid. Geographic longitude begins at -180 degrees west and continues around the globe with a 5 degrees resolution. Geographic latitude resolution is also 5 degrees, from -87.5 south to +87.5 north. The vertical dimension is in a log pressure scale ($ln(p_0/p)$) from -17.0 at the bottom (approximately 30 km) to 5.0 at the top (varying in altitude up to about 500 km). The vertical resolution is 0.5, for a total of 45 pressures.

TIME-GCM solves for global distributions of neutral and plasma temperatures, velocities, and compositions, including all of the species that are photochemically important in the mesosphere, thermosphere, and ionosphere. The TIME-GCM includes all of the processes incorporated into the earlier TIE-GCM: Thermosphere Ionosphere Electrodynamic General Circulation Model [*Richmond et al.*, 1992]. It is unique in its range of altitude coverage (30-500 km), with the critical mesosphere/lower thermosphere region in the center of its numerical grid, allowing dynamical, chemical, radiative, and electro-dynamical couplings between the thermosphere and mesosphere to occur without major boundary influences. This model has been used in a number of studies made to analyze various ground- and satellite-based data.

Here, we introduce the hourly mean profiles of temperature, zonal and meridional wind fields from the 2002 TIME-GCM realistic simulation, into the same tidal analysis program as used for the CSU Na-Lidar data to get relative tidal amplitudes and phases of TIME-GCM predictions for comparison. The 2002 version of TIME-GCM is a more "realistic" simulation, in that it includes the signatures of solar geomagnetic variations by applying 3-hour *Kp* index (indication of geomagnetic activity), and/or nonlinear

interactions between the migrating tide and the planetary waves that are generated in the model with inclusion of the NCEP (National Centers for Environmental Prediction) lower boundary forcing to accounts for gravity wave and planetary wave effects from lower than 30km. The model results still depend intimately on gravity wave parameterization, and evidences resulting from comparison with seasonal variation in lidar and OH temperatures suggest that the gravity wave forcing for this version of TIME-GCM may be stronger than it should be [*Oberheide et al.*, 2003].

We should point out that, in the lidar and tidal model comparison, which is discussed in Chapter 6, there are no fitting parameters in the either GSWM or TIME-GCM models results.

Reference:

Chapman, S., and R. S. Lindzen, Atmospheric Tides, 201pp., D. Reidel, Dordrecht, Holland, 1970.

Dickinson, R. E., E. C. Ridley, and R. G. Roble, A three-dimensional general circulation model of the thermosphere, *J. Geophys. Res., 86,* 1499-1512, 1981.

Forbes, J. M., Atmospheric tides, I, Model description and results for the solar diurnal component, *J. Geophys. Res., 87*, 5222-5240, 1982a.

Forbes, J. M., Atmospheric tides, II, The solar and lunar semidiurnal components, *J. Geophys. Res., 87*, 5241-5252, 1982b.

Forbes, J. M., Middle atmosphere tides, *J. Atmos. Terr. Phys., 46*, 1049-1067, 1984.

Forbes, J. M., The Upper Mesosphere and Lower Thermosphere: A Review of Experiment and Theory: Tidal and Planetary Waves. 67-87, 1994.

Fritts, D. C., Alexander, M. J., Gravity wave dynamics and effects in the middle atmosphere, *Rev. Geophys., 41(1),* 1003, 2003.

Hagan, M. E., J. M. Forbes, and F. Vial, A numerical investigation of the propagation of the quasi 2-day wave into the lower thermosphere, *J. Geophys. Res., 98*, 23, 193-23,205, 1993.

Hagan, M.E., J. M. Forbes, and F. Vial, On modeling migrating solar tides, *Geophys. Res. Lett., 22*, 893-896, 1995a.

Hagan, M. E, Comparative effects of migrating solar sources on tidal signatures in the middle and upper atmosphere. *J. Geophys. Res.101*, 21213-21222, 1996.

Hagan, M. E., J. L., Chang, and S. K. Avery, GSWM estimates of non-migrating tidal effects, *J. Geophys. Res., 102,* 16,439-16,452, 1997.

Hagan, M. E., M. D. Burrage, J. M. Forbes, J. Hackney, W. J. Randel, and X. Zhang, GSWM-98: Results for migrating solar tides, *J. Geophys. Res. ,104*, 6813-6828, 1999.

Hagan, M. E., R. G. Roble, and J. Hackney, Migrating thermospheric tides, *J. Geophys. Res., 106*, 12739-12752, 2001.

Hagan, M. E. and J. M. Forbes, Migrating and nonmigrating diurnal tides in the middle and upper atmosphere excited by tropospheric latent heat release, *J. Geophys. Res., 107*(D24), 4754, doi: 10.1029/2001JD001236, 2002.

Hagan, M. E. and J. M. Forbes, Migrating and nonmigrating semidiurnal tides in the upper atmosphere excited by tropospheric latent heat release, *J. Geophys. Res., 108*(A2), 1062, doi:10.1029/2002JA009466, 2003.

Hedin, A. E., Extension of the MSIS thermosphere model into the middle and lower atmosphere, *J. Geophys. Res.*, 96, 1159-1172, 1991.

Hedin, A. E., et al., Empirical wind model for the upper, middle, and lower atmosphere, *J. Atmos. Terr. Phys.*, 58, 1421-1447, 1996.

Holton, J. R., The Dynamic Meteorology of the stratosphere and Mesosphere, Meteor Monog. 15(37), *Amer. Met. Soc.*, MA, 1975.

Garcia, R.R. and S. Solomon, The effect of breaking gravity waves on the dynamics and chemical composition of the mesosphere and lower thermosphere, *J. Geophy. Res., 90*, 3850-3868, 1985.

Groves, G.V., Hough components of water vapor heating, *J. Atmos. Terr. Phys.*, *44*, 281-290, 1982.

Groves, G.V., A global reference atmosphere from 18 to 80 km, *AFGL Tech. Rep., TR-85-0129*, 1985.

Groves, G. V., Final scientific report, *AFOSR Rep. 84-0045, Air Force Off. Of Sci. Res.*, Bolling Air Force Base, Washington D.C., 1987.

Kato, S., Dynamics of upper atmosphere, *Center for Academic Publications*, Tokyo, Japan, 1980.

McLandress, C. and W. E. Ward, Tidal/gravity wave interactions and their infuence on the large-scale dynamics of the middle atmosphere: Model results, *J. Geophys. Res.*, 99, 8139-8155, 1994.

McLandress, C., The seasonal variation of the propagating diurnal tide in the mesosphere and lower thermosphere, part I, The role of gravity waves and planetary waves, *J. Atmos. Sci.*, 59, 893-906, 2001.

Miyahara, S., and Y. Miyoshi, Migrating and nonmigrating atmospheric tides simulated by a middle atmosphere general circulation model, *Adv. Space Res.*, 20, 1201-1207, 1997.

Richmond, A. D., E. C. Ridley, and R. G. Roble, A thermosphere/ionosphere general circulation model with coupled electrodynamics, *Geophys. Res. Lett., 19,* 601-604, 1992.

Roble, R. G., and E. C. Ridley, A thermosphere-ionosphere-mesosphere-electrodynamics general circulation model (TIME-GCM): Equinox solar cycle minimum simulations (30-500km), *Geophys. Res. Lett., 21,* 417-420, 1994.

Strobel, D. F., Parameterization of the atmospheric heating rate from 15 to 120km due to O_2 and O_3 absorption of solar radiation, *J. Geophys. Res.*, 83, 6225-6230, 1978.

Volland, H., Atmospheric tidal and planetary wave, *Kluwer Academic Publishers*, Norwell, Massachusetts, 1988.

Chapter 6: Seasonal variations of Diurnal and semidiurnal tidal-period perturbations

6-1. Introduction

As discussed in chapter 5, atmospheric solar tides are global oscillations with periods that are sub harmonics of a solar day. Migrating solar tides must have a westward phase velocity in synchronization with Earth's rotation. These waves oscillate with the local sun time. Global oscillations with periods of 24/n (n = integer) that are non-synchronous with the sun are non-migrating tides; they may be stationary, eastward, or westward propagating. At a single station, in addition to global tides, one may also observe local variations with frequencies that are harmonics of diurnal oscillation, but they are not tides. The knowledge of solar tides in the mesopause region, or often referred to the mesosphere and lower thermosphere region (MLT), is essential for the testing of dynamics and chemistry imbed in global models, as its characteristics can impact thermal and dynamical structure in the region. Experimentally, tides may be deduced from zonal averaged well distributed local time observations that cover full diurnal cycles. Short of such a complete global coverage, satellite observation which provides partial local time global coverage and ground-based local time observation at fixed locations provide complementary information revealing properties of migrating and non-migrating tides. Such studies are being pursued in the on-going collaboration with TIMED (Thermosphere, Ionosphere, Mesosphere and Electrodynamics) satellite observation.

Tidal signatures in the mesopause region (80 and 110 km) have been reported for more than a decade from ground-based stations. Most of these observations were carried out by ground-based radars, measuring zonal and meridional winds [Tsuda et al., 1988; Vincent et al., 1988; Manson et al., 1989; Avery et al., 1989; Frank and Thorsen, 1993]. Although relative temperature measurements are now possible with meteor radar [Tsumi et al., 1996; Hocking et al., 1997], study of temperature tides from radar observation has been rare. Temperature measurements with high spatial resolution in the mesopause region have been made by sodium and potassium lidars [Fricke, 1985]. Until recently, most of these measurements were made in nighttime, and only the amplitude and phase of the semidiurnal temperature tides [Williams et al., 1998] could be determined. Daytime temperature measurements with sodium lidar have been possible since 1995 [Chen et al., 1996], making possible the determination of diurnal tidal-period oscillation in mesopause region temperatures. To date, only two sets of data are long enough with yearlong coverage; these have led to the published reports on seasonal variations of diurnal and semidiurnal temperature tides [States and Gardner, 2000; She et al., 2002].

The Colorado State Sodium lidar has been upgraded from a one-beam to a two-beam system and the associated Faraday filters were improved to be robust enough for long-period observation under sunlit conditions. The result is that our lidar system is capable of simultaneous measurements of mesopause region temperature and horizontal winds, over full diurnal-cycles, weather permitting. Since May 2002, regular observations of mesopause region temperature, zonal and meridional winds have been carried out. By the end of April 2003, we have observed a total of 1,491 hours with 659 hours under sunlit conditions. Since this extended data set may still not be long enough to form monthly

means to compare with model predictions, we grouped them on bi-monthly basis for tidal analysis. This part of the thesis reports the bi-monthly diurnal and semidiurnal tidal-period amplitudes and phases in mesopause region temperature, zonal and meridional winds over Fort Collins, CO (41°N, 105°W) based on this data set. The zonal wind results can and will be compared to the yearly seasonal variation of E-W wind perturbations at diurnal and semidiurnal periods based on MF radar observation in nearby Platteville, recently reported [Manson et al., 2003], while the general study of yearly variation of tidal period perturbations in temperature, zonal and meridional winds will be compared to Global Scale Wave Models (both versions '00 and '02) and the 2002 Thermosphere, Ionosphere, Mesosphere and Electrodynamics general circulation model (TIME_GCM) of National Center of Atmospheric Research (NCAR). These models were discussed in Chapter 5.

6-2. Data Set and Analysis

The lidar signals consist of photon profiles of Na fluorescence every 2 minutes from east and north beams, individually pointing 30 ° from zenith. For this study, we first sum the profiles in each hour and vertically smoothed with a Hanning window with full width at half maximum of 2km. The resulting profile is analyzed to deduce line-of-sight wind and temperature for each beam. By assuming the hourly mean vertical wind is negligible, an hourly mean zonal wind profile can be determined from the east-beam observation and meridional wind from the north-beam observation. Since the lidar return signal from each beam gives a temperature, an hourly mean temperature profile for this study is determined from the mean of the two measured values. The measurement precision for

temperature and wind with 2 km spatial resolution and 1 hr integration were estimated under nighttime fair sky condition to be, respectively, 0.5 K and 1.5 m/s at the Na peak (92 km), and 5 K and 15 m/s at the edges (81 and 107 km) of the sodium layer. Due to the necessity of using a Faraday filter for observation under sunlit condition, the received signal is attenuated by a factor of 4 to 5, and we degrade the spatial resolution to 4km for these data, leading to a measurement uncertainty 1.5 times larger than nighttime depending on the residual sky background through the Faraday filter.

Though a total of 1,491 hours of observation amounts to more than 62 times 24 hours of coverage, only about half of these were continuous observations longer than 24 hours at a time. In order to avoid tidal aliasing resulting from data gap of several hours, as in our earlier work on temperature tides [She et al., 2002], with the data between May 2002 and April 2003, we could only compile a total of 29 sets of 24-hour continuous data with gaps at most of 2 hours. There were only 18 sets of data with full diurnal cycle coverage in our earlier study of temperature tides [She et al., 2002], where we grouped the 18 sets into 4 seasons. Though the current data set is well distributed throughout a year, it is still not long enough to form monthly means to compare with model predictions. As a compromise we grouped the data into bi-monthly sets, giving the number of 24-hour sets in each group of 5, 6, 4, 4, 3 and 7, respectively for May-Jun, Jul-Aug, Sep-Oct, Nov-Dec, Jan-Feb, and Mar-Apr. Among the 29 full diurnal cycle observations, there were 4 consecutive 48-hour continuous sets, in Jul '02, Sep '02, Jan '03 and Mar '03. The longest set is an 80-hour continuous observation in Aug '02. The bi-monthly set of Jul-Aug '02 is interesting in that there were three 24-hour sets each month with the August observation made continuously. This bi-monthly data, consisting of two 3-day

composites were studied in detail and the result reported recently [She, 2004]. When diurnal- and semidiurnal-period oscillations were investigated for individual days (full diurnal cycles), we find considerable variability from one day to the next, with amplitudes much bigger than model prediction, implicating contamination of diurnal and semidiurnal tides by longer period modulation (planetary waves, including 2-day waves) and shorter period perturbations (gravity waves). For the case reported, a minimum of 3 days of observation is needed for the coherence of solar forcing to prevail over the variability in diurnal-mean as well as in diurnal and semidiurnal tidal oscillations, leading to the expected convergence to climatology in a multi-day composite observation. Though the amount of data in some bi-monthly sets is still weak (only 3 sets in Jan-Feb '03 for example), we feel the bi-monthly composites over-all should yield results, representative of diurnal and semidiurnal perturbations over Fort Collins, CO (41°N, 105°W).

The procedure for data analysis is typical and was described previously [She 2004]. Briefly, a bi-monthly data set of hourly mean temperature and wind profiles, each consisting of several 24-hour continuous data sets, at 0.5km intervals, are linearly fitted to a constant plus sum of oscillations with diurnal, semidiurnal, terdiurnal and quadiurnal periods at each altitude. The best fitted amplitude and phase for each period with uncertainties are over sampled in altitudes to yield smoother profiles. The resulting diurnal and semidiurnal tidal-period perturbations for each bi-monthly interval are plotted along with either GSWM and/or TIMED-GCM tidal predictions for comparison, and for the investigation of tide. Since we only use 24-hour continuous data, the fitted amplitudes and phases for different tidal components would be independent from one another. We discuss only diurnal and semidiurnal components here; the study of terdiurnal (8-hour

tide) [Smith and Ortland, 2001] and quatradiurnal (6-hour) tides may be a future project. In the analysis outline above, the bimonthly diurnal mean profiles are also deduced. These diurnal means, along with 8 year's CSU Na-lidar nocturnal temperature data, may also be compared to TIME-GCM diurnal means. The seasonal variation of diurnal means is of interest in its own light. We discuss the results and model comparison in Appendix I.

Before we present and compare observation to tidal models, there are caveats. First, when tidal amplitude is comparable to its assessed uncertainty, it could induce a huge uncertainty (as much as half of the tidal period in question) into the tidal phase, because then it will be extremely difficult to seek out the peak amplitude from a data time series with noise of comparable magnitude. Presumably, this could occur in both observation and numerical modeling. So, if there is a sudden jump in the tidal phase, the associated tidal amplitude may be comparable to or smaller than its uncertainty. In this case, the uncertainty in the observed phase would be fairly large. When the observed phase uncertainty is more than a quarter of the tidal period, the observed phase is no longer meaningful. Second, observations at a single station pick up both global and local perturbations. Depending on which one dominates, the observed results could be very different from the model predictions, which only consider global effects. Third, if the observation in a given day catches some transient event, local or global, it could greatly distort the result, especially so for tidal amplitude, and thus causing a big difference between observation and model prediction. This last difficulty can be overcome by long-period extended lidar data acquisition.

6-3. Annual variations of observed diurnal oscillation and comparison to models

We now present our bi-monthly mean oscillations of diurnal period. Since the tidal period oscillations are driven externally and coherently, the phase of the response, indicating the times of maximum temperature, zonal and meridional winds, is fairly robust. We present the seasonal variation in diurnal phases first in Figs. 6-1 and 6-2, along with the GSWM00 & 02 tidal phases predictions. In these following figures, the diurnal phases are plotted as a function of altitudes between 80 and 105km. Though the phase speed (or vertical wavelength) during some data set period appears to change as a function of altitude, for most cases in Figures 6-1 and 6-2, one can draw a straight line between 85 and 95km and deduce a single-phase speed for this altitude range, as the representative downward phase progression of the tidal perturbation.

Among the 18 diurnal phase plots, between 85 and 95km, there are 3 cases, which show an abrupt change in the phase curve and 1 case shows a bend in the curve. In the 3 cases with abrupt change, May-Jun temperature, Fig. 6-1(a3), Sep-Oct meridional wind, Fig. 6-2(c2) and Nov-Dec meridional wind, Fig. 6-2(c3), the abrupt phase change took place at an altitude, at about 89km, 91km and 88km, respectively, where the corresponding amplitudes are fairly small resulting possibly from the destructive interference of more than one tidal mode (see Figs 6-3(a3) and 6-4(c2) for the corresponding amplitudes). So the resulting phase uncertainty is unusually large. We may ignore the value at the abrupt change and still draws a line by connecting the values before and after the jump. The same situation arises for the additional abrupt change in Fig 6-2 (c3) at 96km, and the similar comment can be made for this jump.

There are also some cases with a bend in the phase calculation, The May-Jun zonal wind represents a genuine phase change from one altitude range to the other, see Fig 6-1(b3). This bend case, appearing above 97km, could be results of the poor summer lidar data quality at the top edge of the sodium layer, which is due to the relative low sodium density during the summer months. So we will ignore it in the phase calculation in the Table 1 below. Since the phase speed between 85 and 90km and that between 94 and 97km appears to be the same, we took this speed of 1.35km/hr to be representative. Although this zonal wind phase experiences such a difficulty, the corresponding amplitude, Fig 6-3(b3), appears to be in agreement with GSWM00 between 85 and 95km. These phase speeds and/or vertical wavelengths are so deduced for all 18 cases, and listed in the second column of Table 1 for comparison (the wavelength's error is about ±5km).

Table 1: Vertical wavelength of diurnal tides deduced from phase profiles (85 - 95km)

Vertical λ_z in km	CSU Lidar			GSWM			TIME-GCM		
Bi-mon. (# DC)	T	U	V	T	U	V	T	U	V
Jan(2)-Feb(1)	40	42	17*	26	25	31	30	30	46
Mar(4)-Apr(3)	32	28	34	27	28	30	40	34	60
May(3)-Jun(2)	16	32	48	23	29	34	52	70	73
July(3)-Aug(3)	18	34	89	21	26	30	51	74	60
Sep(2)-Oct(2)	24	27	31	24	26	30	24	26	38
Nov(2)-Dec(2)	Trapped	26	30	30	27	26	30	28	29

 # DC= number of full diurnal cycle data sets (24hr continuous observation).
*** Vertical wavelength between 94 and 102km; below 94km showing trapped mode.**

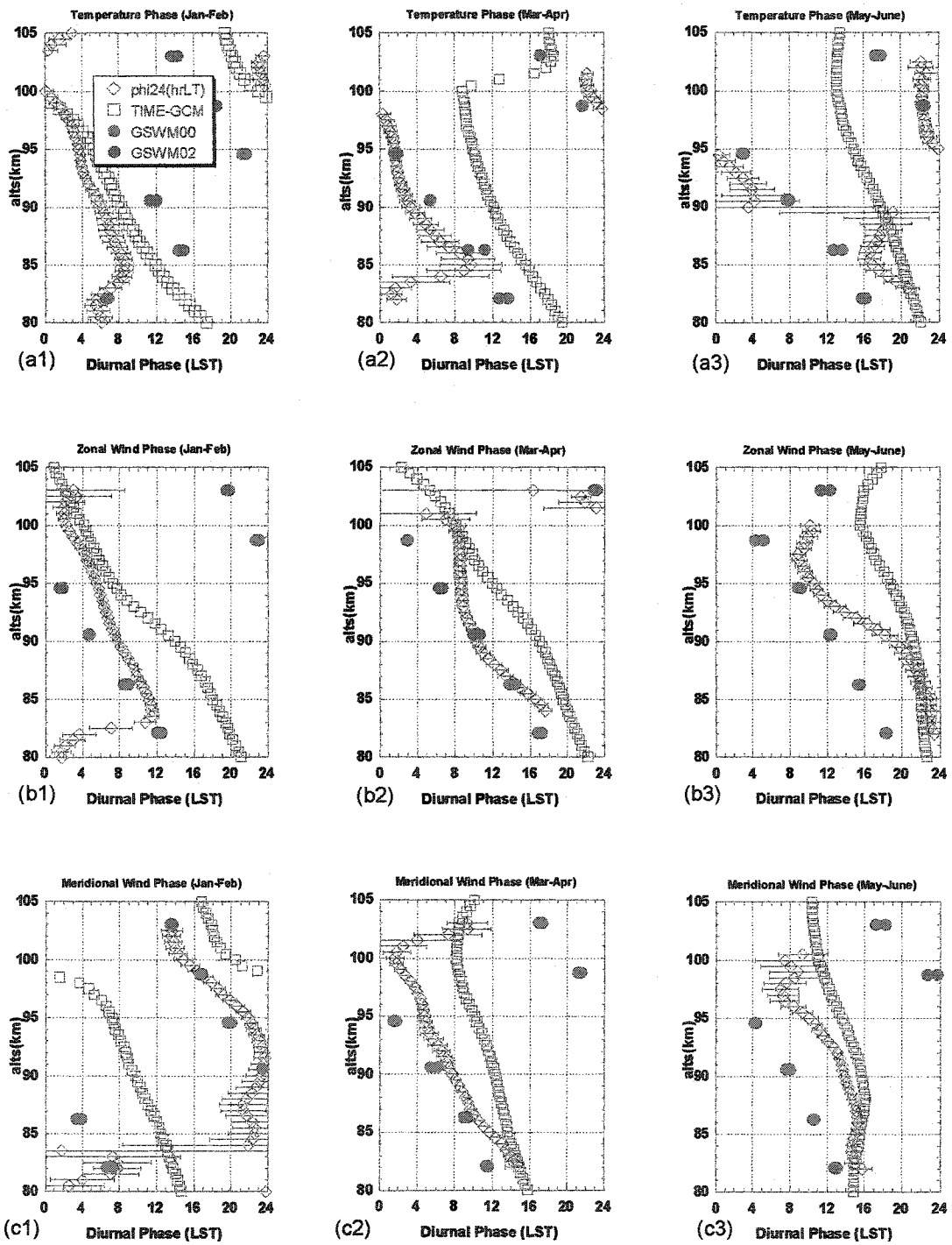

Fig. 6-1 Phases of bi-monthly mean diurnal oscillations (Jan-Feb, Mar-Apr and May-Jun) in temperature, (a1), (a2) and (a3), zonal wind, (b1), (b2) and (b3), and meridional wind, (c1), (c2) and (c3). Also plotted are GSWM00, GSWM02, and TIMED GCM02 predictions. Here the TIME-GCM predictions with the 2002 NCEP input are compared to 2002 observation for May-Jun, and to 2003 observation for Jan-Feb and Mar-Apr.

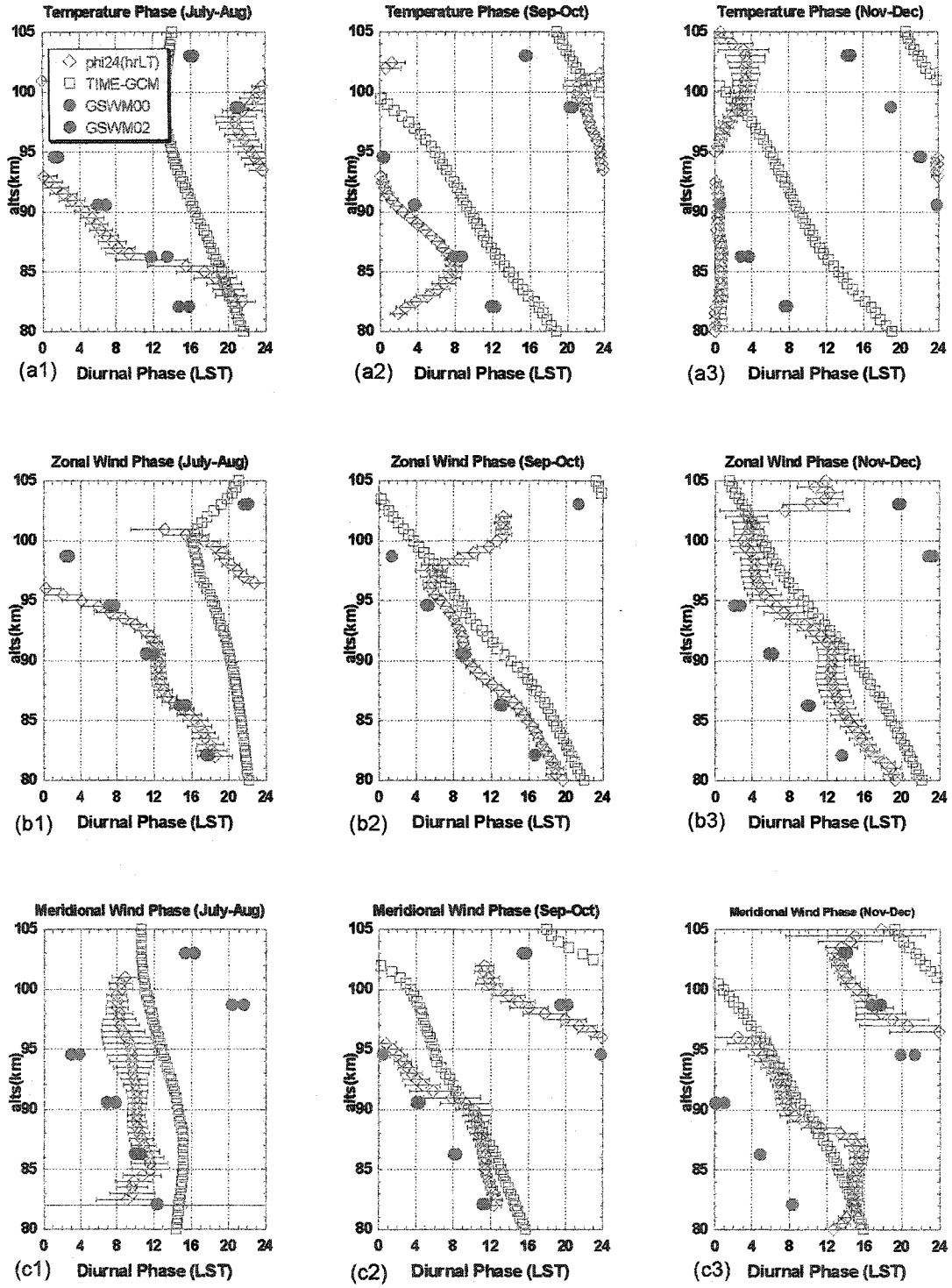

Fig. 6-2 Same as Fig. 1, except for (Jul-Aug, Sep-Oct, and Nov-Dec). Here the TIME-GCM predictions with the 2002 NCEP input are compared to 2002 observations.

We have compared observation of diurnal phases to the prediction of both GSWM00 and GSWM02, as well as that of TIMED-GCM. Here, we derived bi-monthly model amplitudes and phases from the monthly model output for comparison. The diurnal tidal phases comparisons between observation and models are shown in Figs 6-1 and 6-2. In general the difference between GSWM00 and GWSM02 predictions in diurnal phase is within or smaller than the error bar of observation, so we can treat these two predictions as one.

For the diurnal phases of temperature between 85km and 100km, other than Nov-Dec, Fig 6-2 (a3), the observed phases are in excellent agreement with GSWM predictions. There is also very good agreement with TIMED-GCM predictions for Jan-Feb, Fig6-1 (a1) and Sep-Oct, Fig 6-2 (a2). For the bi-monthly mean of Mar-Apr, Fig 6-1 (a2), May-Jun, Fig 6-1 (a3), and Jul-Aug, Fig 6-2 (a1), the TIME-GCM predicted phases lag, and their phase speeds higher than both observed and GSWM predictions. For these months, there is general agreement in phase between observation and all three models in lower altitudes between 80 and 85km. Above 100km, the TIME-GCM predictions show trapping behaviors (no downward phase progression, but almost constant value in one period), and the observed curve also deviate from GSWM and turn more vertical above 90km. The behavior of observed Nov-Dec bi-monthly, Fig. 6-2(a3), which shows non-propagating diurnal oscillations with high temperature near midnight, is very different from both GSWM and TIME-GCM predictions where they show the same phase speed of ~1.5km/hr, and GSWM leads TIME-GCM by 8 hours. The possible implication of this considerable discrepancy between observation and model will be discussed below.

We again found excellent agreement between observation and GSWM diurnal zonal wind phase predictions for all 6 bi-monthly means. As explained earlier, even the May-Jun diurnal phase, which has a genuine phase change (bend) near 91km, and may be considered as agreement. Like in temperature, the TIMED-GCM predicts higher phase speed in May-Jun, Fig 6-1 (b3), and Jul-Aug, Fig 6-2(b1), bi-monthly means. Other than Jul-Aug, Fig 6-2(c1), the observed meridional diurnal phases are in agreement with GSWM, while the TIME-GCM predicts higher phase speeds for Mar-Apr, Fig 6-1 (c2) and May-Jun, Fig 6-1 (c3). The observed Jul-Aug phase speed of meridional wind is ~5km/hr, which is much higher than the GSWM prediction of ~1.3km/hr. Though lagging by 4hrs, the TIMED-GCM predicted phase speed of May-Jun meridional wind is in good agreement with observation.

Following the procedures for diurnal tidal phase, we have also compared observation of diurnal amplitudes to the prediction of both GSWM00 and GSWM02, as well as that of TIMED-GCM. The comparisons are shown in Figs 6-3 and 6-4. In general the altitude dependence (or shape) between GSWM00 and GWSM02 predictions in diurnal amplitudes is the same. Due to the inclusion of non-migrating tidal sources, the amplitude of GSWM02 prediction experiences a dramatic increase, and is about a factor of 2 larger than that of GSWM00. In the discussion below, when we state the agreement between observations with GSWM00, we imply that the GSWM02 prediction overestimates the observation by about a factor of 2. Conversely, agreement with GSWM02 prediction would imply the observation is ~2x larger than GSWM00 prediction.

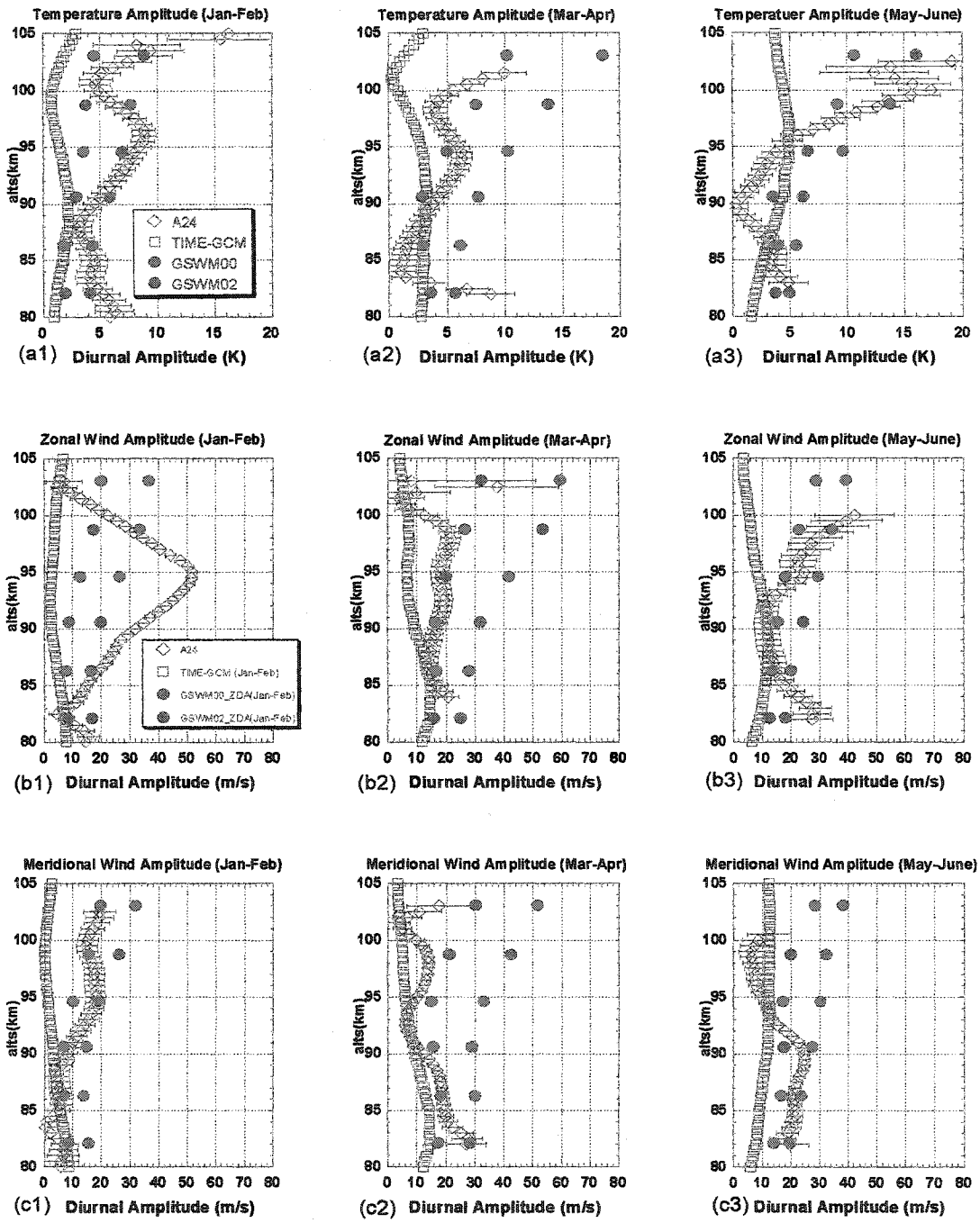

Fig. 6-3 Amplitudes of bi-monthly mean diurnal oscillations (Jan-Feb, Mar-Apr and May-Jun) in temperature, (a1), (a2) and (a3), zonal wind, (b1), (b2) and (b3), and meridional wind, (c1), (c2) and (c3). Also plotted are GSWM00, GSWM02, and TIMED-GCM02 predictions. Here the TIME-GCM predictions with the 2002 NCEP input are compared to 2002 observation for May-Jun, and to 2003 observation for Jan-Feb and Mar-Apr.

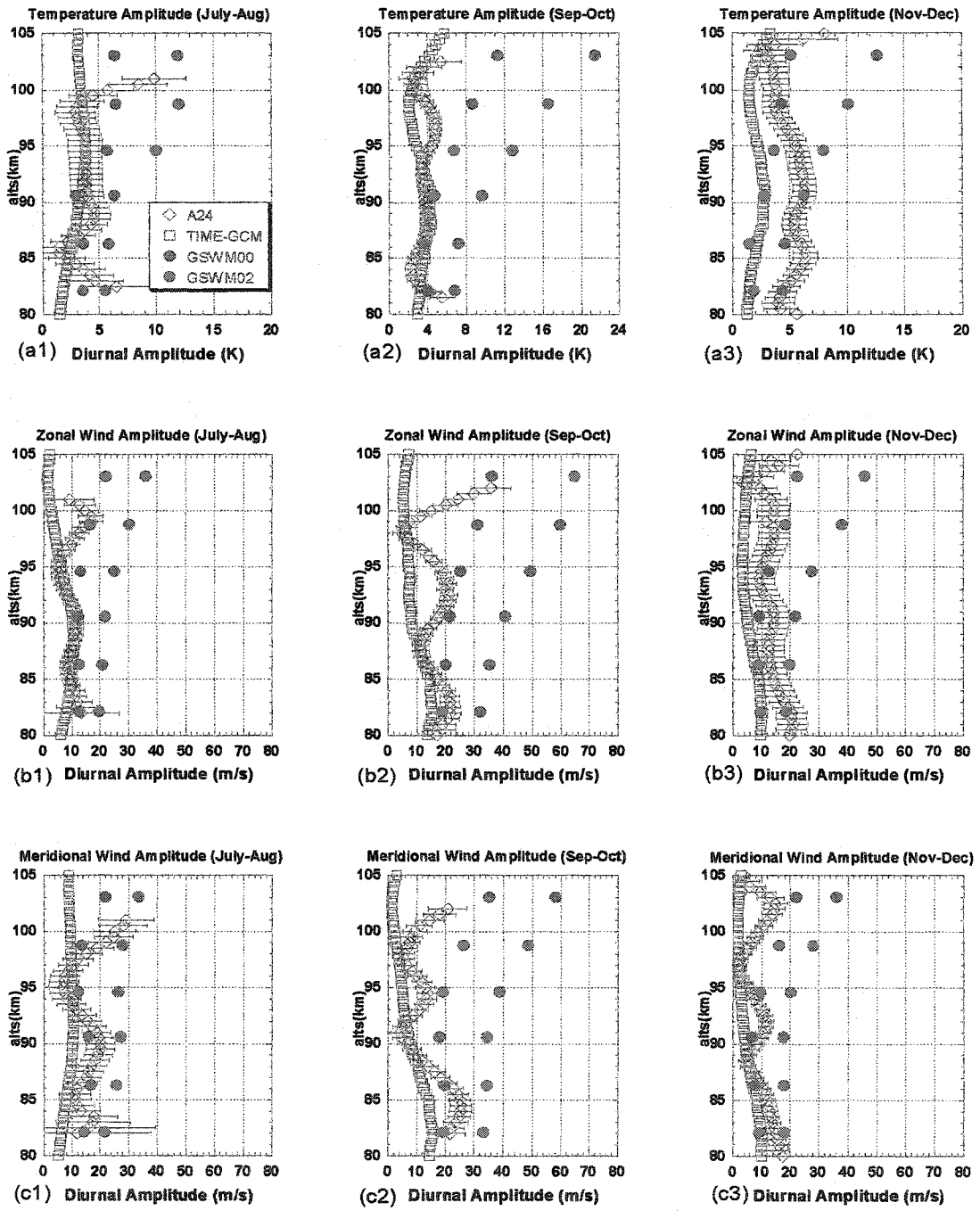

Fig. 6-4 Same as Fig. 3, except for (Jul-Aug, Sep-Oct, and Nov-Dec). Here the TIME-GCM predictions with the 2002 NCEP input are compared to 2002 observations.

For the diurnal temperature amplitudes, GSWM00 predictions are between 2 to 4K between 80 and 90km in altitudes. The amplitudes are then increased linearly from 90km

to 105km to ~5K in Jan-Feb, Fig 6-3 (a1), Jul-Aug, Fig 6-4 (a1), and Nov-Dec, Fig 6-4 (c1), and to ~10K in other three bi-monthly periods. As mentioned earlier, the GSWM02 predictions are similar in altitude dependence, but with about twice in magnitude. Below ~90km, we found observation in agreement with GSWM00 for Mar-Apr, Fig. 6-3 (a2), May-Jun, Fig. 6-3 (a3), Jul-Aug, Fig. 6-4 (a1), Sep-Oct, Fig. 6-4 (a2), and with GSWM02 in Jan-Feb, Fig. 6-3 (a1) and Nov-Dec, Fig. 6-4 (a3), suggesting that non-migrating contributions are more significant in winter months. Below 90km, TIME-GCM predictions are in good agreement with those of GSWM00. Above 90km, the observed amplitude profiles of Jan-Feb, Fig. 6-3 (a1), Mar-Apr, Fig. 6-3 (a2), and May-Jun, Fig. 6-3 (a3), exhibit wavy patterns, with amplitudes increasing considerably above 100km to values comparable to GSWM02 predictions for Jan-Feb and May-Jun. The interference effect is more pronounced for May-Jun with severe destructive interference occurring at 90km; other than this minimum, the observed amplitude agrees with GSWM predictions quite well. The variability associated with such wavy patterns in the tidal amplitude will be discussed below. Like the profile of Jul-Aug, Fig. 6-4 (a1), below 100km, the observed profiles for Sep-Oct, Fig. 6-4 (a2), and Nov-Dec, Fig. 6-4 (a3), are nearly isothermal; the Jan-Feb and Mar-Apr profiles are in good agreement with TIMED-GCM predictions.

The observed zonal wind diurnal amplitudes for Mar-Apr, Fig. 6-3 (b2), Jul-Aug, Fig. 6-4 (b1), and Nov-Dec, Fig. 6-4 (b3) are nearly constant and in general agreement with GSWM00 predictions, which are in agreement with TIME-GCM for Jul-Aug, but larger by ~2x for Mar-Apr and Nov-Dec profiles. The observed profiles for Jan-Feb, May-Jun, and Sep-Oct all again show the wavy structures; their values for May-Jun profile between

85 and 95km are comparable to GSWM and TIME-GCM predictions, while the values near 95km for Jan-Feb is strikingly larger than both GSWM00 and TIME-GCM predictions, respectively by 4 and 10 times. The observed values above 95km are smaller than GSWM00 but comparable to TIME-GCM predictions for the Sep-Oct profile. The observed meridional wind amplitudes all show mild wavy structures with bi-monthly means comparable to GSWM00 and larger than TIME-GCM predictions below 90km. The observed values above 90km are smaller, comparable to and larger than GSWM00 predictions, respectively for Mar-Apr, Fig. 6-3 (c2), Sep-Oct, Fig. 6-4 (c2), and Nov-Dec, Fig. 6-4 (c3); Jan-Feb, Fig. 6-3 (c1), and Jul-Aug, Fig. 6-4 (c1); and May-Jun, Fig. 6-3 (c3). The observed diurnal meridional wind amplitudes are larger than TIME-GCM predictions for all bi-monthly mean tides.

In short, except for Nov-Dec diurnal temperature and Jul-Aug meridional wind, the observed diurnal phases are in good agreement with GSWM predictions. The observed phase speed of Jul-Aug meridional wind is comparable to TIME-GCM prediction and higher than GSWM prediction, while the observed phase of Nov-Dec diurnal temperature is a trapped mode with both models showing a propagating phase speed of ~1.3km/hr. The trapped mode refers to the wave that its energy is trapped within a region. Beyond this region, its energy will be decreasing as it goes up. The related phase will stay almost constant along the altitude. The so-called propagating mode's energy, however, will propagate up with the wave. As in our case, the heating source seems to be turned on every midnight. The observed phase speeds in Mar-Apr, May-Jun and Jul-Aug temperatures, May-Jun and Jul-Aug zonal winds, and Mar-Apr and May-Jun meridional winds are all lower than the TIME-GCM predictions. The detailed comparison between

observed and model phase speeds is shown in Table 1. The observed diurnal amplitudes show considerable wavy structure. These effects are most pronounced in Jan-Feb temperature and in Jan-Feb, Mar-Apr and May-Jun zonal winds. Observed diurnal temperature amplitudes are in good agreement with GSWM00 predictions for Mar-Apr, and May-Jun, with GSWM02 for Jan-Feb, and with TIME-GCM for Jul-Aug. For Sep-Oct, the observed amplitudes are in agreement with GSWM00 below 90km and with TIME-GCM above 90km, while that for Nov-Dec are in agreement with GSWM02 and GSWM00, respectively for below and above 90km. The observed zonal and meridioanl wind amplitudes below 90km are in general agreement with GSWM and TIME-GCM predictions, while their values above 90km are smaller than GSWM00 predictions and larger than TIME-GCM predictions, except for Jan-Feb zonal wind, where observed value at 95km is larger than GSWM00 and TIME-GCM, respectively by 4 and 10 times, and for May-Jun meridional wind, where the observed values are larger than all model predictions by more than a factor of two.

As mentioned, most of the lidar diurnal tidal phase observations are in good agreement with GSWM00&02, except the temperature diurnal tidal phase in Nov-Dec, which shows trapped mode behavior instead of propagating mode. It is interesting that this temperature diurnal tidal phase behavior repeated itself in Nov-Dec, 2003. If we plot the temperature diurnal tidal phase of Nov and Dec in 2002 separately (not shown in this paper), they show quite similar trapped mode characteristic. This eliminates the possibility that this trapped mode is from the combination of two out of phase waves from different months. Likely, there exists a local diurnal oscillation in Nov-Dec that favors midnight heating. The cause of this local heating source is unknown. Also, since the diurnal tidal sources

forcing is getting weak (H_2O) in the winter, local tidal effects may become the dominant role in the diurnal oscillation. This will be discussed further in the section of tidal consistency. When observed diurnal tidal amplitude observations are comparable to GSWM00, we do not usually see the classical behavior of tidal amplitude increasing with the altitude as predicted by the model. Instead, the observed diurnal amplitudes show damping effects at upper mesopuase, and the wavy pattern through out the profile. The damping effects may be related to the gravity wave breaking or dissipation (turbulent/eddy gravity wave dissipation can also accelerate the tides). Thus it drags the diurnal tidal amplitude at high altitude. The larger than observations tidal amplitudes in GSWM02 model imply that the non-migrating tidal source due to the deep convection activity of rain drop formation may not play as an important role at mid-latitude over Fort Collins, CO as suggested by model. However the migrating tidal sources, like H_2O (IR) in the troposphere, O_3 (UV) in the stratosphere and lower mesosphere are relatively consistent, so that the migrating tides still play a major role. Again, this will be discussed further in the lidar tidal consistency study.

By comparing the observed bi-monthly mean diurnal oscillations for a period of one year to a model such as GSWM00 at 42°N, also binned bi-monthly, we discuss the annual variation of observed diurnal oscillations over Fort Collins, CO (41°N, 105°W). To provide a visual comparison, we plot in Fig. 6-5 altitude-bi-monthly contour plots of diurnal amplitudes and in Fig. 6-6 diurnal phases of temperature, zonal and meridional winds, along with the corresponding GSWM00 predictions of diurnal tide contours for comparison. We should be cautioned by the observation above 100km and below 83km in summer months due to poor data quality in these months. As noted, a recent paper by

Manson et al. [2003] compared observed diurnal tide in zonal wind measured by MF radar in nearby Platteville, CO (40.2°N, 104.7°W) to the GSWM00 predictions at 39°N. In general, both zonal wind measurements yield reasonably agreement with GSWM00 predictions, though the discrepancy with our observation is noticeably less. We mention here that the difference between GSWM00 at 39°N, binned monthly, which was used by Mannson et al., and that at 42°N, binned bi-monthly, which we use, is relatively small; they may be considered as the same for the purpose here.

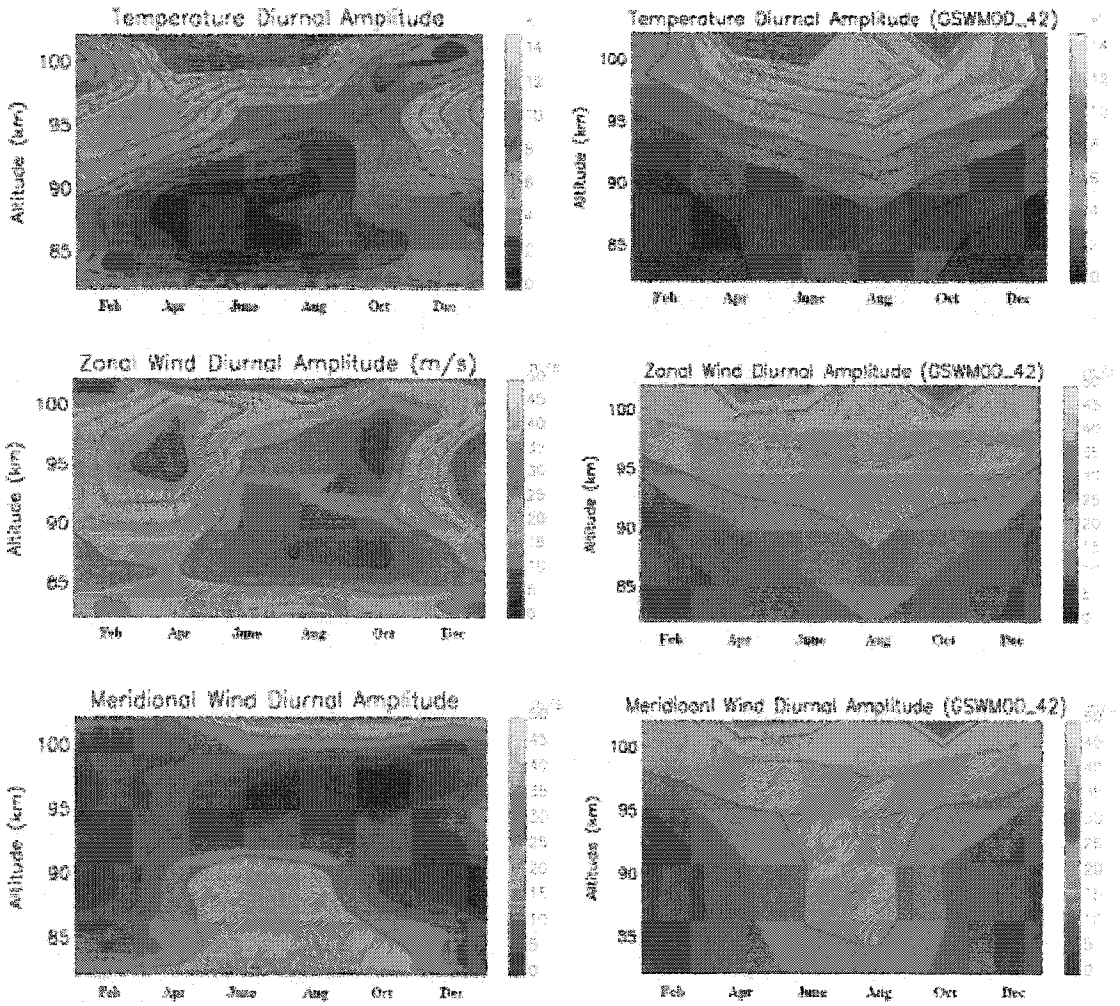

Fig. 6-5 Seasonal variation of diurnal tidal amplitudes: comparison between bi-monthly observation (left) and bi-monthly mean GSWM00 prediction (right). Top, middle, and bottom panels are for temperatures, zonal wind, and meridional winds, respectively.

The GSWM00 diurnal temperature phase, top right panel of Fig.6-6, is divided into 3 bands with phases in lower altitude summer lag those in the mid-altitudes, which in turn lead those in higher altitude winter; the observed phase captures this general feature, but with less symmetry. The observed diurnal phase in zonal wind captures the features of GSWM00 predictions quite well in seasonal symmetry. However, the phases in winter

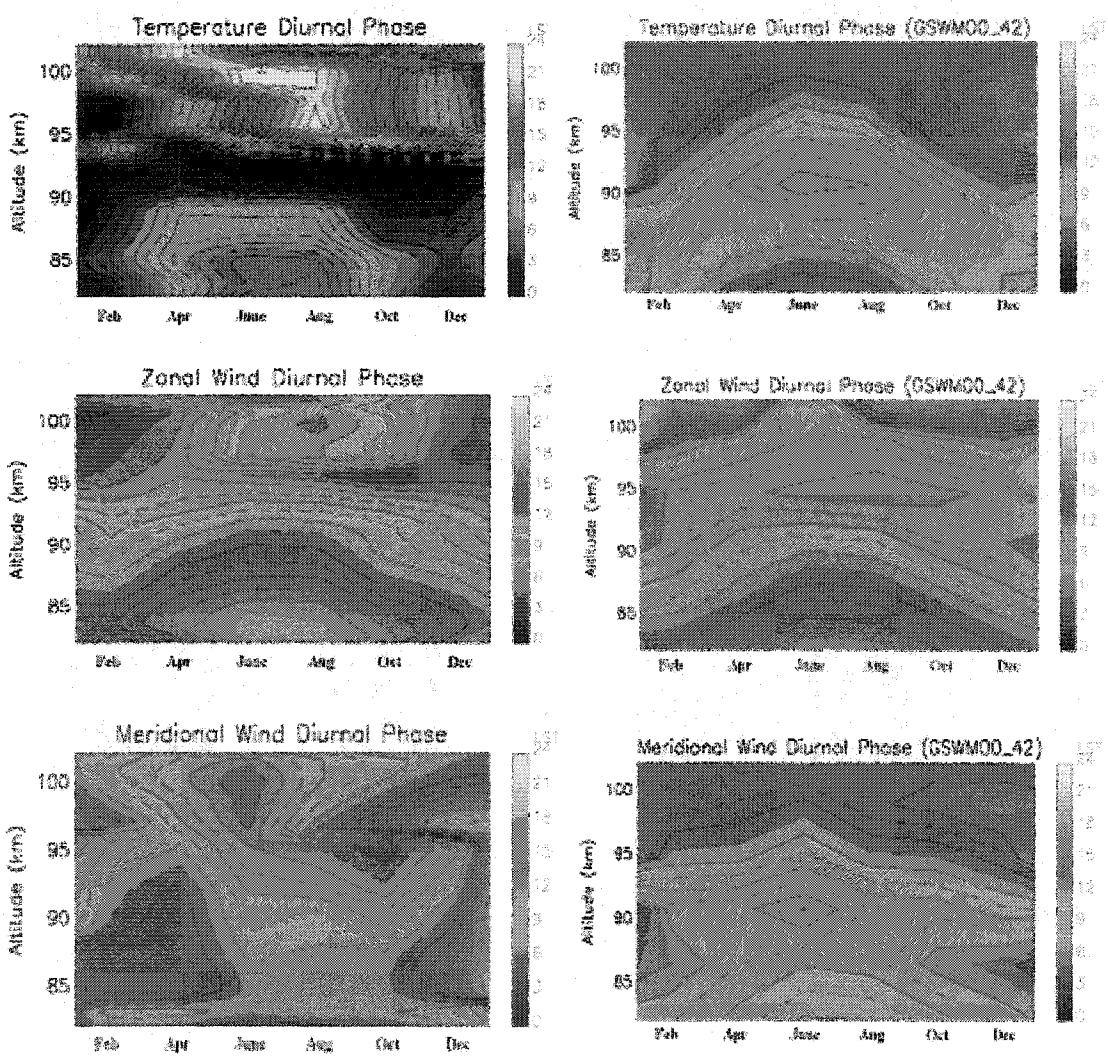

Fig. 6-6 Same as Fig. 5, except for diurnal tidal phases.

months between 95 and 100km lag those between 90 and 95km by ~3hr in observation, contrary to GSWM00 predictions. This particular discrepancy exists between zonal wind observation from Patteville MF radar and GSWM00 predictions [Manson et at, 2003].

The observed diurnal phase in meridional wind was in marginal agreement with the GSWM00 prediction. Part of the discrepancy is the result of treating local time 24 and 0 differently near 95km in the contour plot, whereas they are the same in reality. The observed diurnal amplitude contour plots of temperature and zonal wind, top and middle panels of Fig. 6-5, capture the relative magnitudes in both seasonal and altitude distributions of GSWM. The observed meridional wind amplitude also captures the general pattern of GSWM00, with magnitude higher below 90km and lower by a factor of 2 above 90km.

6-4. Annual variations of observed semidiurnal oscillations and comparison to models

We now turn our attention to the study of bi-monthly mean oscillations of semidiurnal period. Like in the investigation of diurnal tide, we present the seasonal variation in semidiurnal phases first, and in Figs. 6-7 and 6-8, and we then compared the observation to GSWM00, GSWM02 and TIME-GCM predictions. As expected, the observed main vertical wavelengths are longer than those for diurnal components. The two versions of GSWM predictions are nearly the same. The agreements in semidiurnal tidal phases are not as good. However, contrary to the diurnal case, the winter semidiurnal phases of Nov-Dec, Fig. 6-8(c3), are in excellent agreement with the GSWM predictions. Unlike the model predictions, the observed semidiurnal temperature phases in May-Jun, Fig.6-7(a3), Jul-Aug, Fig. 6-8(a1), and Sep-Oct, Fig. 6-8(a2), show nearly trapping vertical wavelengths. For zonal and meridional winds, except for May-Jun, Fig. 6-7(b3) and Fig.6-7(c3), the observed phase speeds are in good agreement with both GSWM and TIME-GCM predictions. In most of these cases, the observed phases are between GSWM

and TIME-GCM predictions, with the former lagging and latter leading the observed value by 2-3hrs, respectively. The discrepancy between observed and model semidiurnal phase speeds in temperature, zonal and meridional winds for May-Jun, which all show

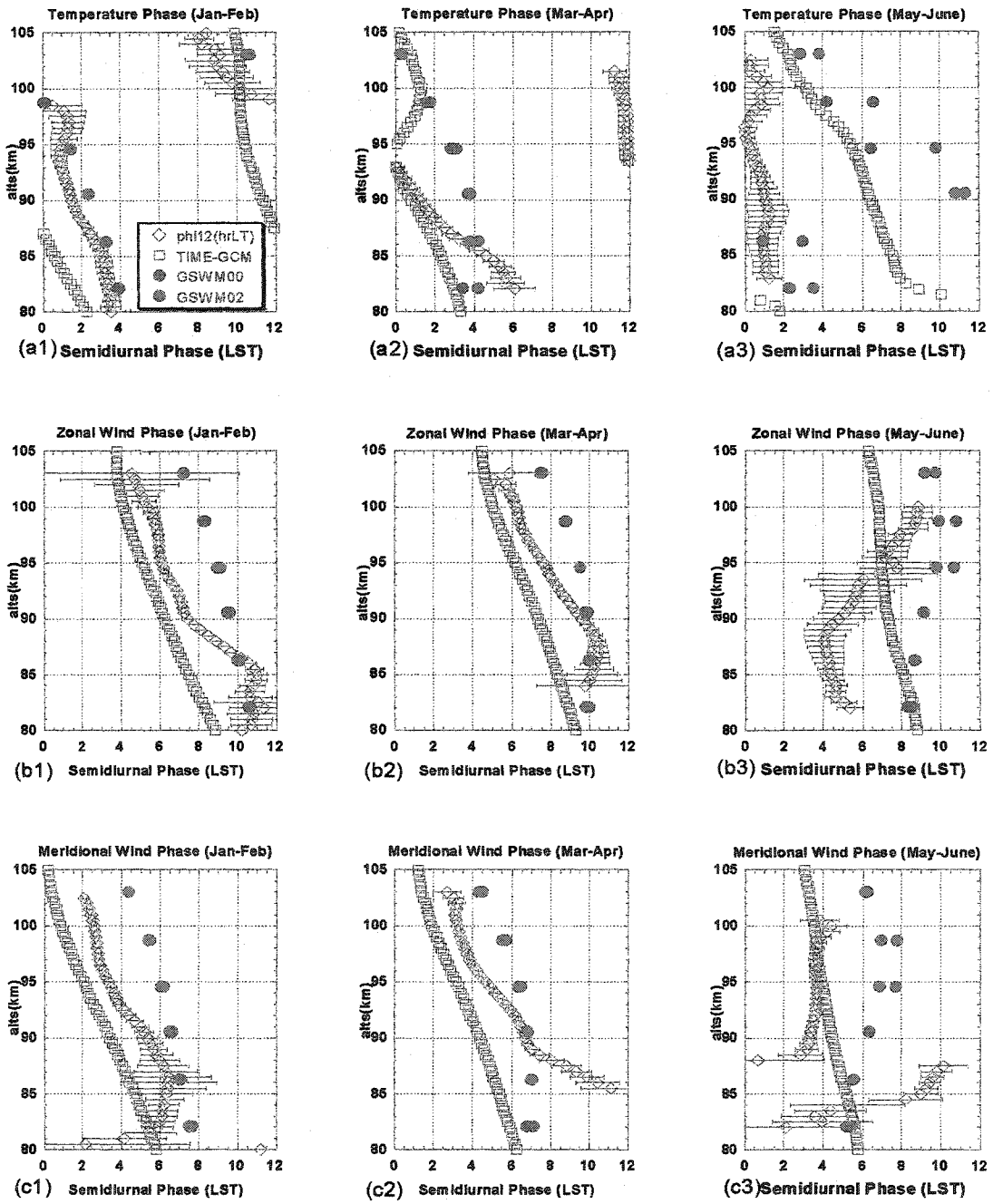

Fig. 6-7 Same as Fig. 1, except for semidiurnal tidal period oscillations

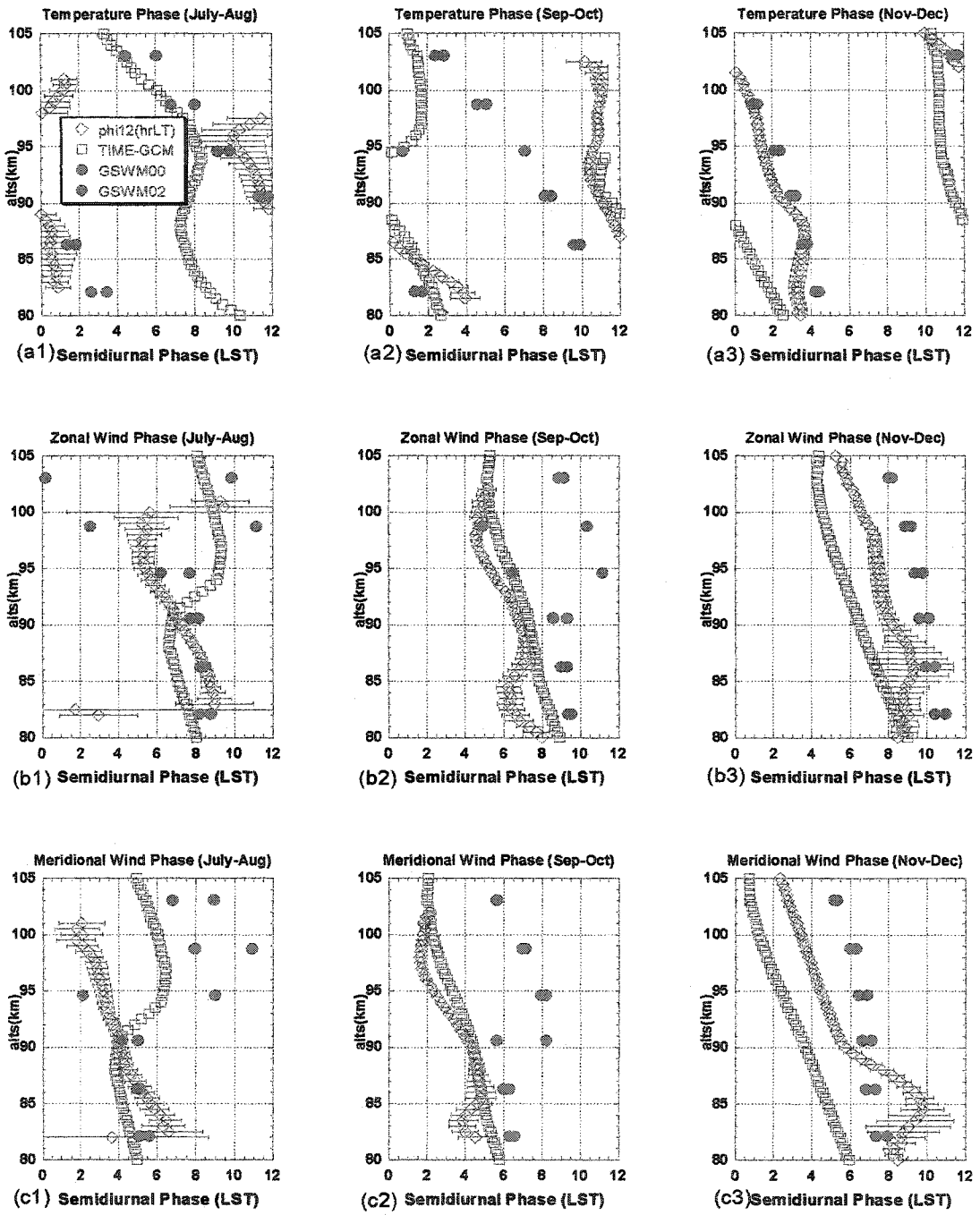

Fig. 6-8 Same as Fig. 2, except for semidiurnal tidal period oscillations

considerable trapping as compared to model predictions. To what extent do these discrepancies persist will be discussed below in the tidal consistency section. The comparison of mean vertical wavelength between 85 and 95km are presented in Table 2.

Table 2: Vertical wavelength of semidiurnal tides deduced from phase profiles (85 - 95km)

Vertical λ_z in km	CSU Lidar			GSWM			TIME-GCM		
Bi-mon. (# DC)	T	U	V	T	U	V	T	U	V
Jan(2)-Feb(1)	51	58	43	46	66	60	34	53	42
Mar(4)-Apr(3)	25[a]	34	32	81	48	60	61	54	48
May(3)-June(2)	trapped	-30	-120[b]	38[c]	-96[b]	-75[b]	38	120	105
July(3)-Aug(3)	trapped	33	60	21	21	36	24	72	78
Sep(2)-Oct(2)	21	36	40	21	43[c]	42[c]	36	64	72
Nov(2)-Dec(2)	62	60	60	58	100	92	100[c]	54	54

 # DC= number of full diurnal cycle data sets (24hr continuous observation).
[a] Vertical wavelength between 85 and 93km; above 93km showing trapped mode.
[b] Negative wavelength indicates propagating upward phase progression.
[c] Based on phase slope above 95km, where the amplitude is relatively large.

Turning to the study of annual variation and comparison of semidiurnal amplitudes, Figs 6-9 and 6-10, we first point out that unlike for the diurnal amplitudes, there is little difference between GSWM00 and GSWM02 predictions in semidiurnal amplitudes. There are a couple of reasons. First, the latent heat release associated with the rain drop formation has its most atmospheric response in the equatorial region (latitude -20° to +20°). Second, its atmospheric response peaks around 115km to 120km, which is beyond our lidar detection range [Hagan, 1996]. However, there is excellent agreement between GSWM and TIME-GCM in the semidiurnal amplitude predictions up to 100km for summer months; for these months, both models predict nearly constant, but relatively small amplitudes compared to observation. In general, GSWM predicts two categories of semidiurnal amplitude profile between 80 and 100km. First category of profiles starts at

80km with smaller amplitude, which increases gradually to 90 km, after which the amplitude takes at a faster rate of increase, changing the value by a factor of 3-5 from 90km to 105km. All profiles for Jan-Feb, Mar-Apr and Nov-Dec fall into this type. Other than Jan-Feb temperature, the observed profiles in this category are in good agreement with the GSWM prediction. For these profiles, the TIME-GCM predicts nearly constant but somewhat smaller amplitude with values in reasonable agreement with GSWM and observation below 90km. However the TIME-GCM predicted amplitudes way too small above 95km. There exists a destructive interference at ~100km in the observed Jan-Feb semidiurnal temperature, which causes its amplitude to deviate from GSWM predictions. The second major category of GSWM predictions shows nearly constant amplitude profiles between 80 and 100km as can be seen in May-Jun, Jul-Aug, and Sep-Oct profiles. In these cases, the model agreement between GSWM and TIME-GCM is clear. Much of the disagreement between model prediction and observation appears to come from a constructive interference existing in the observed amplitude profile at ~90-95km, which show a factor of 2-4 times enhancement in the middle of the observed profiles. These effects are evident on May-Jun, Jul-Aug and Sep-Oct profiles in temperature, zonal and meridional winds. The case of May-Jun zonal wind semidiurnal amplitude, Fig. 6-8(b3), is somewhat different. Here the agreement occurs between 85 and 95km, while larger observed values are seen in altitudes above and below. Interestingly, similar altitude dependence is observed in the May-Jun zonal wind diurnal amplitude, Fig. 6-3(b3). The other exception is the observed May-Jun semidiurnal meridional amplitude, which is in agreement with model predictions below 90km, but larger by a factor of 2 above.

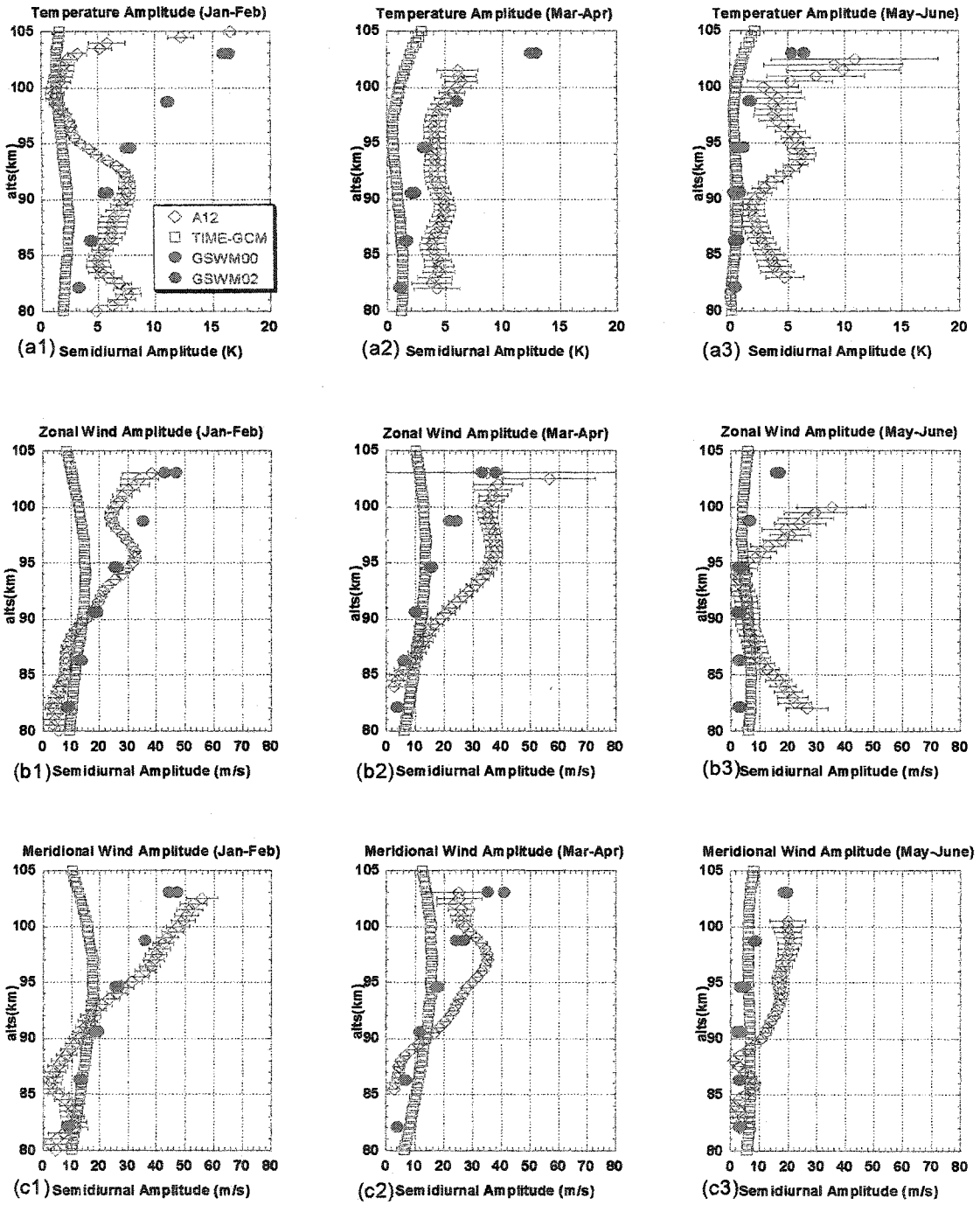

Fig. 6-9 Same as Fig. 3, except for semidiurnal tidal period oscillations

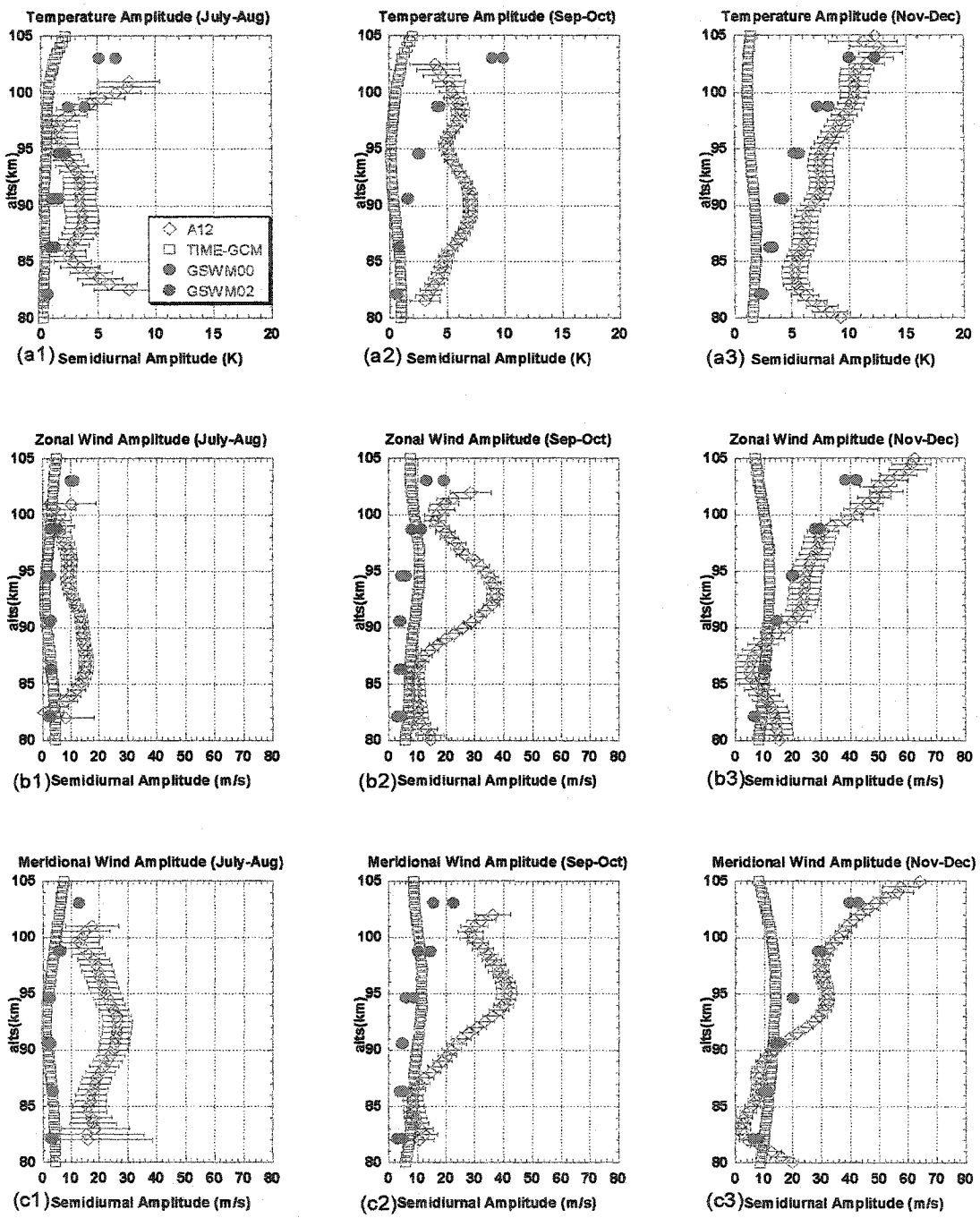

Fig. 6-10 Same as Fig. 4, except for semidiurnal tidal period oscillations.

In all these plots above, we pay attention to those plots where the semidiurnal amplitudes for both model and observation are big enough to produce meaningful

semidiurnal tidal phase. This leads us to focus on phase comparison plots of the winter (Nov-Dec, Jan-Feb), spring (Mar-Apr) and fall (Sep-Oct) months. In the comparison, we should ignore the region where the tidal amplitude is relatively small when we investigate the tidal phase. The exceptional agreement between observation and models in semidiurnal amplitudes and phases in winter indicates the great success of models in these months. Other than the temperature semidiurnal phases, the spring (Mar-Apr) and autumn (Sep-Oct) comparisons also showed positive results. The abnormal, discontinuous features in the spring and autumn temperature semidiurnal tidal phase plots, Figs. 6-7(a2) and 6-8(a2), may be the result of combining two quite different semidiurnal tidal behaviors before and after equinoxes (Check Appendix II, in which each 29 complete diurnal cycle tidal results were plotted separately). This discontinuous behavior in semidiurnal phase in equinox months, however, does not occur in semidiurnal zonal and meridional wind phases, nor does it occur in diurnal phases in temperature or wind. One might suspect that a local perturbation is at work, but we await correlated study with radar winds and more lidar temperatures to understand this puzzle more clearly. Both observation and model show the peak semidiurnal amplitude in winter and minimum amplitude value in summer, which means the semidiurnal tidal sources (O_3, O_2 and H_2O) are competing differently in different seasons [Hagan, 1996]. The extremely small semidiurnal amplitudes in model predictions (smaller than observation) in the summer months (from May to August) not only make it difficult to study the related phase behavior, it also raise the question about possible missing semidiurnal tidal source in the model. For example, there might be a consistent local source. Its atmospheric response is in phase with other known semidiurnal tidal sources, and therefore, the

resulting semidiurnal tidal amplitude gets boosted. Another possible explanation is that the atmospheric response of H_2O and O_3 might not be completely out of phase in the summer [Hagan, 1996], so that there might be less cancellation between these two responses. Or, one of these two sources or their atmospheric responses is underestimated in summer by the model.

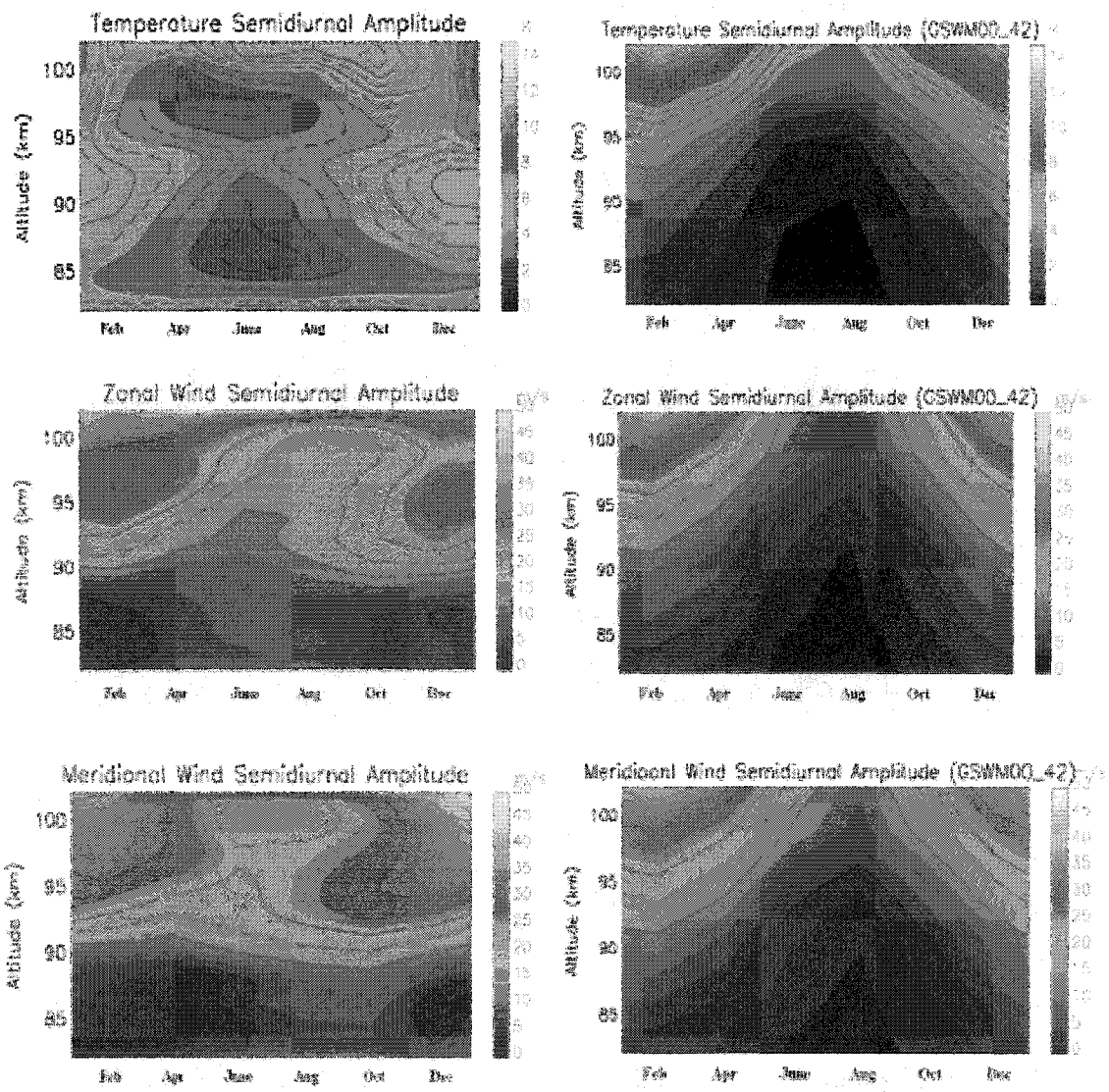

Fig. 6-11 Same as Fig. 5, except for semidiurnal tidal amplitudes.

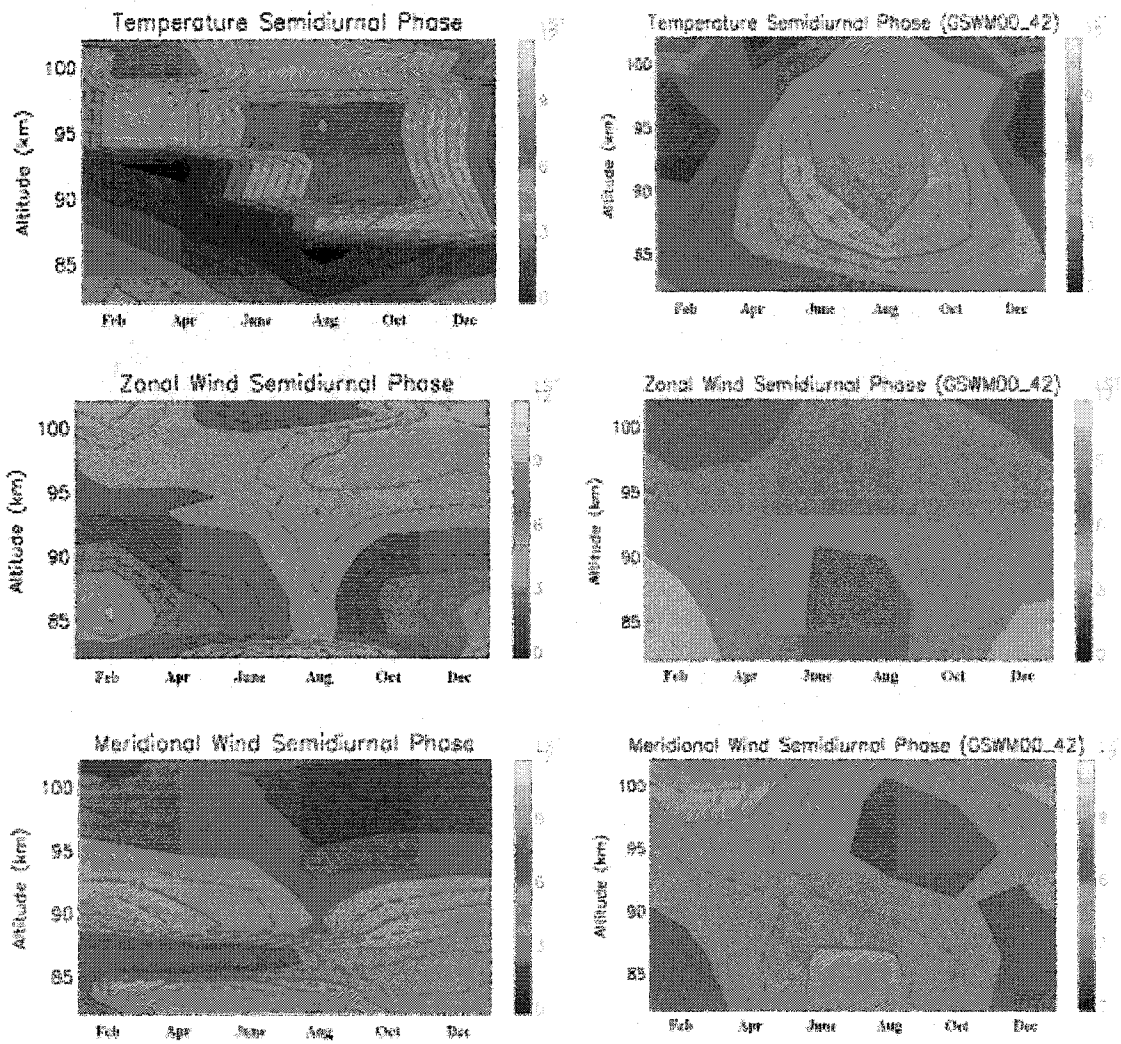

Fig. 6-12 Same as Fig. 6, except for semidiurnal tidal phases

By comparing the observed bi-monthly mean semidiurnal oscillations for a period of one year to a model such as GSWM00, also binned bi-monthly, we discuss the seasonal variation of observed semidiurnal oscillations over Fort Collins, CO (41°N, 105°W). To provide a visual comparison, we plot in Fig. 6-11 altitude-bi-monthly contour plots of semidiurnal amplitudes and in Fig. 6-12 semidiurnal phases of temperature, zonal and meridional winds, along with the corresponding GSWM00 predictions for comparison.

Again, we should ignore the observation data above 100km and below 83km during the summer, due to the relative poor data quality at the edge of the sodium layer during these periods. Though the semidiurnal amplitude contour plots show similar structure to the GSWM, unlike the diurnal cases, the observed values are considerably larger, especially in summer months. The GSW00 semidiurnal temperature phase has a prominent structure in Jul-Sep, top right panel, Fig. 12, between 90 and 95km with phases lagging the rest of the plot. The observation indeed captured this structure very well. The temperature amplitude variations show similar structure as well, with GSWM00 prediction smaller in summer, but larger in winter above 90km. The agreement in semidiurnal zonal wind phase between observation and GSWM00 is marginal, though they appear to have structures that resemble each other with a much larger range in observation. The observed semidiurnal tide thus appears to have shorter vertical wavelength than model calculation. The agreement in semidiurnal zonal wind amplitudes is very good in both structure and magnitude below 100km. Like in zonal wind, the agreement in semidiurnal meridional wind phase between observation and GSWM00 is marginal, though they also appear to have similar structures with a much larger range in observation. The agreement between observation and GSWM00 predictions in meridional wind amplitude is not as good as that of zonal wind; it nonetheless captures the seasonal structure predicted by the model. Relative to the recent comparison [Manson et al., 2003] between observed semidiurnal zonal wind tide in nearby Platteville, CO (40.2°N, 104.7°W) measured by MF radar and the GSWM00 predictions at 39°N, the seasonal variation of our observation is in better agreement with the model prediction. For example, the MF radar observed semidiurnal zonal wind amplitude showed semiannual

variation, while the lidar observed amplitude show only annual variation in agreement with the GSWM00 prediction.

6-5. On tidal consistency and variability

Up to the end of 2003, CSU Na-lidar has about 20 months of full diurnal cycle observation. To build tidal climatology, the consistency and variability of the observed tidal behavior need to be tested and studied. Since our data set is still not long enough to do a credible job in this regard, we chose in this section to compare selected bi-monthly tidal results between years 2002 and 2003. The bi-monthly periods chosen for the comparison are May-Jun, Jul-Aug and Nov-Dec, because there exists higher degree of discrepancy between observation and model predictions in semidiurnal temperature phase speeds in May-Jun and Jul-Aug, and in diurnal temperature phase in Nov-Dec. The corresponding phase speeds in zonal and meridional winds for Jul-Aug and Nov-Dec are however in reasonable agreement. We do not discuss the consistency of Sep-Oct semidiurnal temperatures because the observed phase speeds are in good agreement with the TIME-GCM prediction. With more and more data accumulated, hopefully we can smooth out the tidal-period variations within every month, and build up the tidal climatology for the mid-latitude region.

Over all, both diurnal and semidiurnal tidal amplitudes for these three periods are relatively consistent between 2002 and 2003, despite the fact that there were more full diurnal cycle coverage in 2003 with 7, 8 and 6 data sets, respectively, for May-Jun, Jul-Aug and Nov-Dec; this compares to 5, 6 and 3 data sets, respectively, in 2002. Shown in Fig. 6-13 are semidiurnal temperature tides for these three periods in both years. As expected, the semidiurnal temperature phases for Nov-Dec, Fig. 6-13(f), are in agreement

between the two years and with the model predictions. The same can be stated about the amplitudes. Though the phase speeds of semidiurnal temperature tides do not agree with model predictions in May-Jun, Fig. 6-13(b), the observed phase speeds between the two years show similar vertical structure. The semidiurnal phases for zonal and meridional winds for both years (not shown) are also similar and both showed trapping for considerable altitude range. There exists an obvious shift in July-Aug temperature semidiurnal phases, Fig. 6-13(d), between 2002 and 2003 data set, by ~4hrs at 85km and by ~8hrs between 90 and 95km. In a correlated manner, the semidiurnal temperature amplitudes, Fig. 6-13(c), show considerable different altitude-dependence. On the other hand, the observed semidiurnal zonal and meridional wind tides in Jul-Aug (See plots in Appendix III, where every tidal component of this 3 periods is shown.) are in general agreement for these periods between the two years. The corresponding diurnal temperature tidal amplitudes and phases are shown in Fig. 6-14. Here, as expected, the phases for May-Jun and Jul-Aug are in agreement between the two years and with model predictions. The phase agreement in May-Jun, Fig. 6-14(b) was somewhat distracted by the huge error bars near 90km and 85km, respectively, for 2002 and 2003 due to the destructive interference observed at these altitudes in the corresponding amplitude profiles, Fig. 6-14(a). For Nov-Dec, Fig. 6-14(f), the diurnal temperature tidal phase disagree with model predictions, but the observed phases between the two years are in excellent agreement. Surprisingly, the observed diurnal amplitudes for these periods are also in very good agreement between the two years. Even the altitude where the slope of diurnal amplitude changes for these two years is very close (around 92-93km).

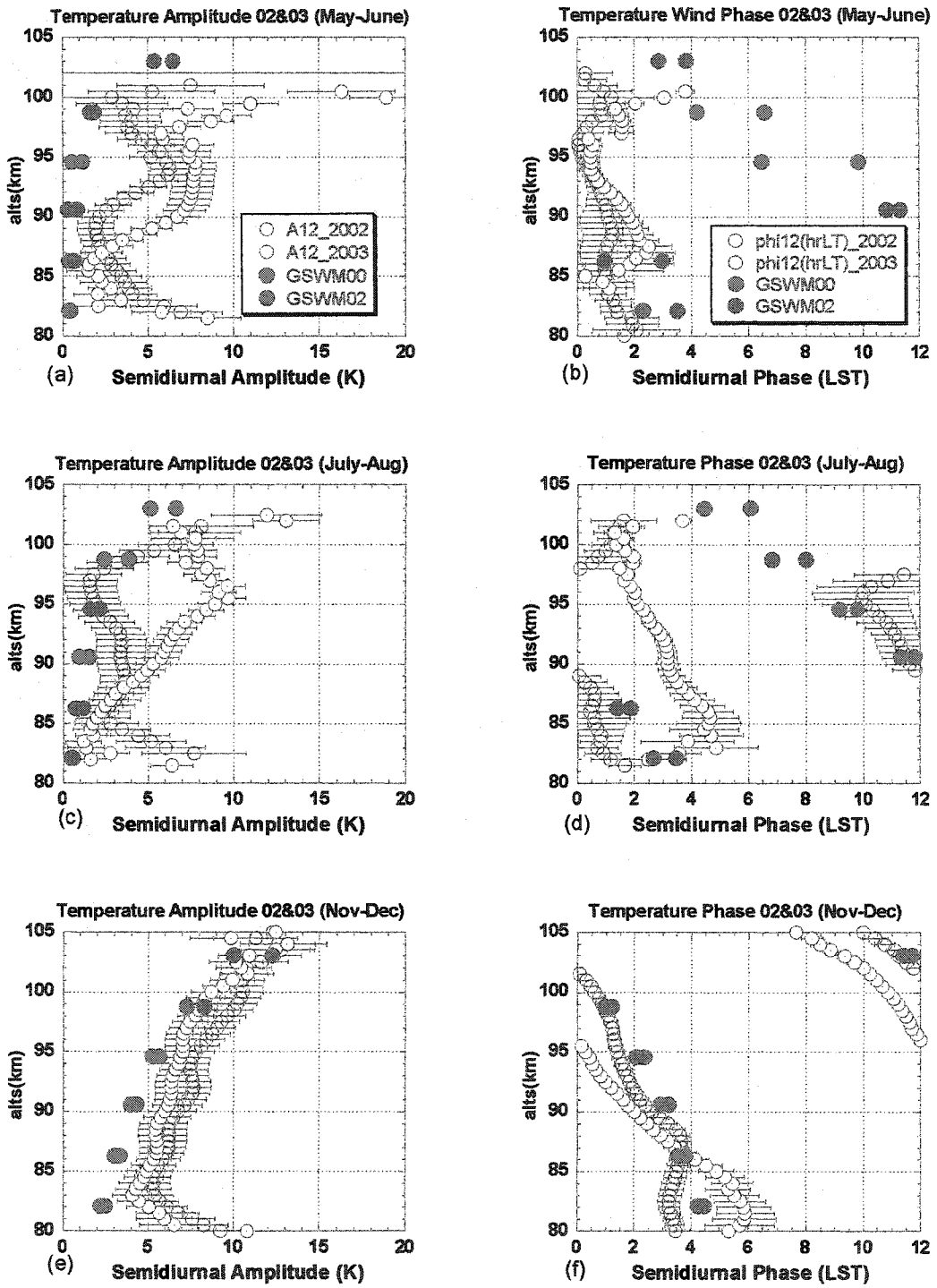

Fig. 6-13 Observed amplitudes and phases of bi-monthly semidiurnal temperature tides of May-Jun, (a) and (b), Jul-Aug, (c) and (d), and Nov-Dec, (e) and (f) are compared between 2002 (red) and 2003 (black). These observations are also compared to GSWM00 and GSWM02 predictions.

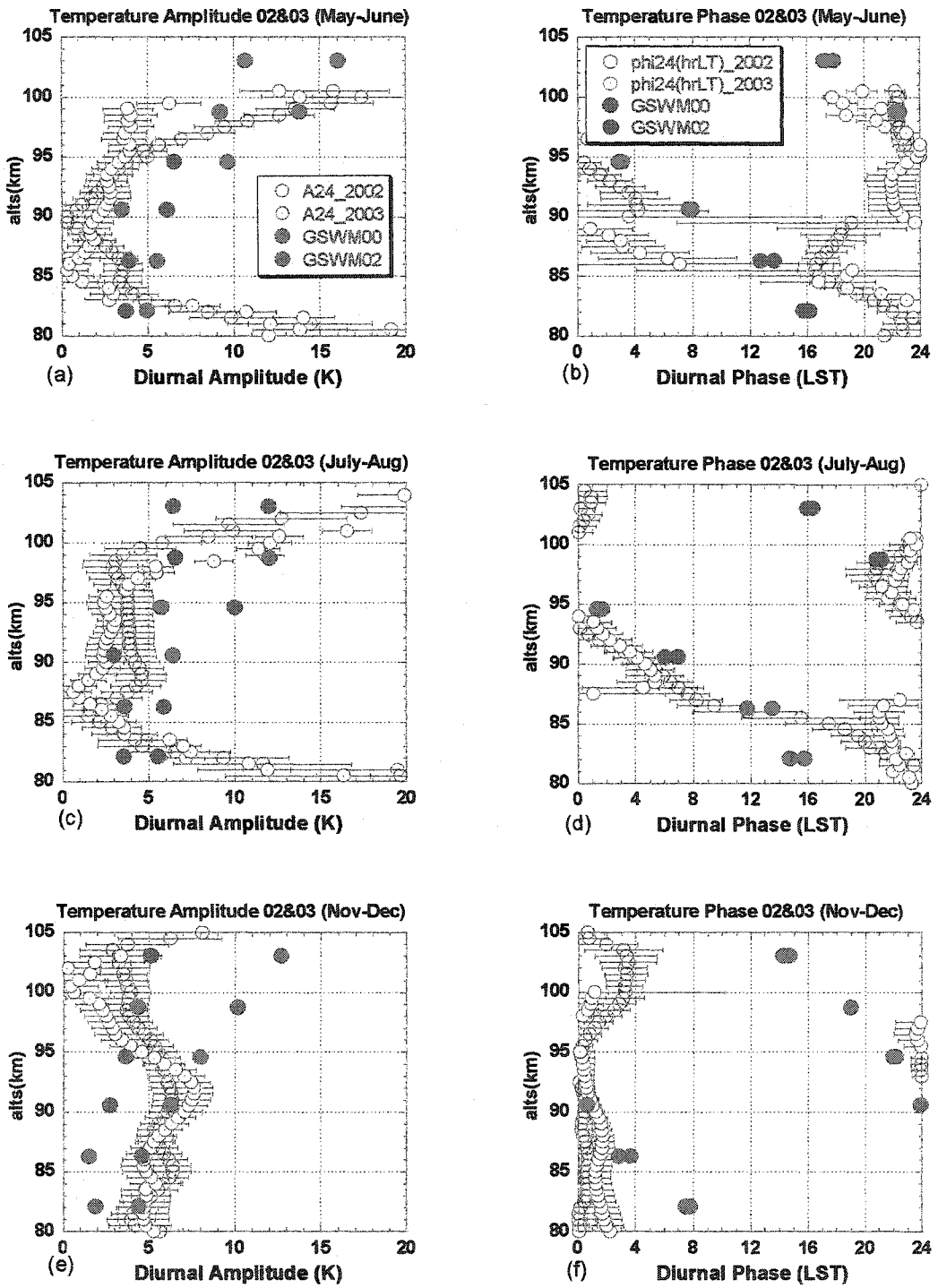

Fig. 6-14 Same as Fig. 13, except for diurnal temperature tides.

The observed consistency for the cases that disagree with model prediction is interesting and revealing. The Nov-Dec diurnal temperature perturbations are an

excellent and fortunate example, for which our earlier temperature observations in 1997-1999 may provide supporting information. Compared to observation of She et al. [2002], except for Nov-Dec, the bi-monthly mean diurnal temperature tidal phases reported here are in agreement with earlier results of seasonal tidal temperatures as they both are in agreement with GSWM00 predictions. She et al. [2002] binned 6 diurnal data sets in Dec, Jan, and Feb together as winter, and their Fig. 2(h) showed observed diurnal winter temperature phase with downward phase propagation in agreement with GSWM00. Their winter result is in agreement with our Jan-Feb observation [Fig.6-1 (a1)], but disagree with our Nov-Dec result [Fig.6-2 (a3)], giving rise to the possibility that the observed diurnal oscillations over Fort Collins are different between Jan-Feb and Nov-Dec. This suggestion apparently is supported by the winter tidal variability study presented in Fig. 4(f) of the same paper, in which they showed diurnal temperature phases of 4 days in Jan-Feb (days 29, 39, 40, 51) and 2 days in Dec (days 348 and 350). Interestingly, they showed downward propagating phase progressions for the 4 days in Jan-Feb in agreement with our Fig. 6-1(a1), and trapped phases for the 2 days in Dec, again in agreement with our Fig. 6-2(a3). The tidal consistency revealed in our observation between data obtained in 2002-2003 and in 1997-1999 is gratifying. It likely suggests that there exist significant local contributions to diurnal temperature perturbations in Nov-Dec, while the corresponding perturbations in Jan-Feb appear to be dominated by global perturbations. The trapped diurnal temperature phase in Nov-Dec as shown in Fig. 6-14(f) suggests the existence of a local source in favor of midnight heating. Also, since the diurnal tidal sources forcing is getting weak (H_2O) in the winter, local tidal effects may play the dominant role in the diurnal oscillation. The origin of this midnight heating source is

difficult to pin down. The diurnal amplitudes for 2002 and 2003 as shown in Fig. 6-14(e) are consistent; their profiles between 80 and 92km, ~5K, are in agreement with GSWM02, suggesting that the observed values have captured non-migrating tidal contributions. However, the decrease in tidal amplitude to a minimum near 100km is worth noticing. The two individual Dec days observed in 1998 [Fig.4 (e) in She et al., 2002] give very different diurnal amplitude profiles with a maximum value near 95km. All these could suggest the dominance of perturbations, which may depend on local conditions and vary from one year to another. That trapping (nearly constant phase along the altitude profile) in Nov-Dec seems occur only in diurnal temperature tidal phase, Fig.6-14(f), and not in wind phases, i.e., Figs. 6-2(b3) and 6-2(c3) is perplexing. However, this may be the work of a local heating source that impact temperatures, while the horizontal wind is still controlled by global perturbations.

The wavy patterns that exist in many diurnal amplitudes may be investigated. Like our results presented here, the earlier diurnal temperature results [She et al., 2002] also showed in their Figs. 2(a) and 2(e) wavy patterns in Spring and Autumn diurnal temperature amplitudes with a wavelength ~10km. Using 24-hour continuous data, they also plotted diurnal tidal amplitudes for individual days, four in Spring [their Fig. 4(i)] and five days in Autumn [their Fig. 4(a)]. Eight of these nine days showed wave patterns with a vertical wavelength ~10km but with altitudes of the extreme shifted somewhat relative to one another. Though the causes for the existence of persisting wave pattern in tidal amplitudes are not clear, beating between two modes with different wavelengths is suggested [She et al., 2002]. The appearance of a wave structure in diurnal tidal amplitudes in equinox over Fort Collins appears to be a consistent feature.

The local time offset is one of the main issues of the semidiurnal tides consistency study. The semidiurnal tides in some months show considerable local time offset (such as temperature semidiurnal phase in Jul-Aug, Fig. 6-13(d)), even though the vertical wavelengths are almost the same. If the offset is less than a couple of hours, we can still say that they are in phase. However, the observed local time phase offset of ~4hr or ~8hr in the semidiurnal phases could bring out another question about the phase locking of the tidal wave between these two different years observation. For Jul-Aug observation, presumably there were sufficient data sets, seven for 2002 and eight for 2003, yet the bi-monthly mean phases are still shifted. Multi-year observations appear to be needed for its resolution.

Again, in both of these two years, diurnal amplitudes often do not increase with altitude as theory predicted, but with considerable vertical structures, whereas semidiurnal amplitudes mostly behave more in agreement with theory. One explanation may be related to the gravity wave breaking around upper mesopause region. Gravity wave breaking deposits momentum and causes turbulence in the mesopause, and the net effect is to reduce the diurnal tide amplitude at mid-latitude region, due to the relative short vertical wavelength of the diurnal tides [Garcia and Solomon, 1985]. On the other hand, because of the longer vertical wavelength (faster phase speed) of the semidiurnal tide, the gravity wave breaking does not affect the semidiurnal tide very much. Also, the diurnal tides are on the edge between propagating and trapped modes at mid-latitude, whereas the semidiurnal tides are dominated by propagating modes in this region [Forbes, 1995].

6-6. Conclusion

Starting from May 2002, the CSU lidar group has been able to perform full diurnal cycle observation semi-regularly. The one-year's observation results, from May 2002 to April 2003, give us the ability to study the seasonal variation of solar thermal tidal behavior over Fort Collins, CO. We compared our observation tidal results with GSWM (both 00 and 02 versions) and TIME-GCM prediction, and the comparison results are encouraging. To further evaluate the comparison, we analyzed the newer data acquired after May 2003 for select periods where large discrepancy exists between model and observation, as well as invoked on 1998 temperature observations to investigate tidal consistency. A number of conclusions could be derived from our analysis.

First, except for Nov-Dec temperature, there exists excellent agreement in diurnal phase speed between observation and all three models predictions. In terms of absolute value, observed phases agree with GSWM predictions (nearly the same between 00 and 02 versions) better than with TIME-GCM predictions.

Second, by comparing the results of winter temperatures from 2003 observation as well as from earlier 1998 temperature data, we find the discrepancy between Nov-Dec observation and model predictions in diurnal tidal phase persists from one year to the next. We suggest that the nearly trapped diurnal temperature phase, not accompanied by the corresponding horizontal wind phases, is likely caused by a local (longitudinal dependent) source of diurnal period, in favor of midnight heating.

Third, the observed diurnal amplitudes agree very well with GSWM00 predictions, which are typically smaller (larger) by a factor of 2 than GSWM02 (TIME-GCM). In

equinox months, Mar-Apr and, the observed diurnal amplitudes in meridional wind take values very close to TIME-GCM predictions.

Fourth, the general agreement in diurnal amplitudes with GSWM00 rather than GSWM02 suggests the dominance of migrating diurnal tides over Fort Collins (41°N, 105°W). Though observation data from a single station are not sufficient for the determination of tide, the considerable agreement between observation and GSWM00 in diurnal amplitudes and especially in phases suggest that other than Nov-Dec diurnal temperature, much of the observed diurnal tidal-period oscillations are likely migrating diurnal tides passing over Fort Collins, CO. The over-damping in TIME-GCM amplitudes above 95km compared to observation, during equinox and summer months, may result from an over-estimate of gravity wave forcing in the 02 version of the TIME-GCM model.

Fifth, unlike observed semidiurnal amplitudes, which increase with altitude as predicted by model, the observed diurnal amplitudes often over-damped above 90km, possibly influenced by gravity wave breaking or dissipation.

Sixth, There exist persisting wavy patterns in diurnal and semidiurnal amplitudes with wavelength of ~10km, particularly so in equinox months. This is likely the result of beating between two modes with the same tidal-period. The origin of this awaits further correlative studies.

Seventh, the agreement between observation and GSWM predictions (nearly same between 00 and 02) in winter, i.e., Jan-Feb and Nov-Dec, is very good for both semidiurnal amplitudes and phases. In general, the agreement in phase between

observation and model predictions is not as good as for diurnal tide. The agreement in semidiurnal phase speed with TIME-GCM is generally the best.

Eighth, other than in winter months, the model predictions for semidiurnal amplitudes are considerably smaller than observation, particularly so in summer months, suggesting miscounting a semidiurnal source, or misfiguring the competition between H_2O and O_3 heating sourced in the summer.

Ninth, based on bi-monthly means we plotted altitude-bimonthly contours of observed diurnal and semidiurnal amplitudes and phases for temperature, zonal and meridional winds. The counterparts derived from bi-monthly means of GSWM00 model predictions were also plotted for comparison. Though the observations capture the features of the model in general, these plots reveal some of their differences in a more apparent manner.

Tenth, the explanation for the pronounced differences between the GSWM and the TIME-GCM predictions is beyond the purview of this report.

In summary, our bi-monthly mean decomposition of diurnal and semidiurnal tidal-period oscillations in mesopause region temperature, zonal and meridional winds, yielded results in general agreement with GSWM00 model predictions. This work represents the first comprehensive study of this type based on observational data, containing both temperature and horizontal wind. The consistency study of lidar tidal results was conducted by analyzing newer data (May03-Dec03) during selected periods within the current May 02-Apr 03 data set, where observation shows considerable discrepancy from model predictions in tidal phases. Since the result of the limited study shows consistency among the yearlong data set, newer data and the temperature observations in 1998, this

yearlong data set appears to be long enough for the determination of diurnal and semidiurnal components of solar tides. We plan to continue the same data acquisition mode for two additional years, at the end of which time we will report tidal climatology as well as tidal variability in more detail. At that time, we should have enough data to credibly assess tidal variability, and to bin the data monthly to match the resolution of tidal models.

References:

Avery, S. K., R. A. Vincent, A. Phillips, et al., High latitude tidal behavior in the mesosphere and lower thermosphere, *J. Atmos. Terr. Phys., 51*, pp 595-608, 1989.

Chen, H., C. Y. She and Eric Korevaar, "Na Vapor Dispersive Faraday Filter", *Opt. Lett. 18*, 1019-1021 (1993).

Chen, H., M. A. White, D. A. Krueger et al., Daytime mesopause temperature measurements using a sodium-vapor dispersive Faraday filter in lidar receive. *Opt. Lett. 21*, 1003-1005, 1996.

Forbes, J. M., Tidal and planetarty waves, in The Upper Mesosphere and Lower Thermosphere: A Review of Experiment and Theory, *Geophys. Monogr. Ser., vol. 87*, edited by R. M. Johnson and T. L. Killeen, pp.67– 87, AGU, Washington, D. C., 1995.

Franke, S. J., and D. Thorsen, Mean winds and tides in the upper middle atmosphere at Urbana (40°N, 88°W) during 1991-92, *J. Geophys. Res., 98*, 18607-18615, 1993.

Fricke, K. H. and U. von Zahn, Mesopause temperatures derived from probing the hyperfine structure of the D2 resonance line of sodium by lidar, *J. Atmos. Terr. Phys. 47*, 499, 1985.

Garcia, R.R. and S. Solomon, The effect of breaking gravity waves on the dynamics and chemical composition of the mesosphere and lower thermosphere, *J. Geophy. Res., 90*, 3850-3868, 1985.

Hagan, M. E., Comparative effects of migrating solar sources on tidal signatures in the middle and upper atmosphere, *J. Geophys. Res.*, 101, 21,213 –21,222, 1996.

Hagan, M. E., R. G. Burrage, J. M. Forbes, et al., GSWM-98: Results for migrating solar tides, *J. Geophys. Res.* 104, 6813-6828, 1999.

Hagan, M. E. and R. G. Roble, Modeling diurnal tidal variability with the National Center for Atmospheric Research thermosphere-ionosphere-mesosphere-electrodynamics general circulation model, *J. Geophys. Res. 106*, 24,869-624,882, 2001.

Hagan, M. E., and J. M. Forbes, Migrating and nonmigrating diurnal tides in the middle and upper atmosphere excited by tropospheric latent heat release, *J. Geophys. Res.*, 107(D24)-ACL-6(1-15), 4754, doi:10.1029/2001JD001236, 2002.

Hagan, M. E., and J. M. Forbes, Migrating and nonmigrating semidiurnal tides in the upper atmosphere excited by tropospheric latent heat release, *J. Geophys. Res.*, 108(A2)-SIA-6(1-14), 1062, doi:10.1029/2002JA009466, 2003.

Hedin, A. E., et al., Revised global model of thermospheric winds using satellite and ground-based observations, *J. Geophys. Res.*, 96, 7657-7688, 1991.

Hocking, W.K., and T. Thayaparan, Simultaneous and co-located observation of winds and tides by MF and Meteor radars over London, Canada, (43N, 81W) during 1994-1996, *Radio Sci., 32*, 833-865, 1997.

Manson, A. H., C. E. Meek, H. Teitelbaum, et al., Climatologies of semi-diurnal and diurnal tides in the middle atmosphere (70-110 km) at middle latitudes (40-50), *J. Atmos. Terr. Phys., 51*, pp 579-593, 1989.

Mason, A. H., C. E. Meek, S. K. Avery, et al., Ionosperic and dynamical characterstics of the mesosphere-lower thermosphere region over Plattevill (40°N, 105°W) and comparisons with the region over Saskatoon (52°N, 107°W), *J. Geophys. Res., VOL.108, NO. D13*, 4398, 2003.

Manson, C. E. Meek, Maura Hagan, et al., Global Distributions of Diurnal and Semi-Diurnal Tides: Observations from HRDI-UARS of MLT Region and Comparisons with GSWM-02 (Migrating, Non-migrating Components), (In preparation, 2004).

Oberheide, J., M. E. Hagan, G. Lu,et al., Sampling the NCAR TIME-GCM and GSWM for TIMED and CEDAR related studies and preliminary model/observation comparisons, *CEDAR Meeting*, Longmont, CO, USA, June 2003.

Roble, R.G., On the feasibility of developing a global atmospheric model extending from the ground to the exosphere, in Atmospheric Science Across the Stratoapuse, Geophysical Monograph, 123, American Geophysical Union, 53-67, 2000.

She, C. Y., S. Chen, B. P. Williams, et al., Tides in the mesopause region over Fort Collins, CO (41°N, 105°W) based on lidar temperature observations covering full diurnal cycles. *J. Geophys. Research, 107, NO,* 10.1029/2001JD001189, 2002.

She, C. Y., Initial full-diurnal-cycle mesopause region lidar observations: Diurnal-means and tidal perturbations of temperature and winds over Fort Collins, CO (41N, 105W), PSMOS 2002, *J. Atmo. Solar-Terr. Phys.* (In press, 2004).

Smith, A. K., and D. A. Ortland, Modeling and analysis of the structure and generation of the terdiurnal tide, *J. Atmos. Sci.*, 58, 3116– 3134, 2001.

States, R. J., and C. S. Gardner, Temperature structure of the mesopause region (80 – 105 km) at 40_N latitude, 2, Diurnal variations, *J. Atmos. Sci.*, 57, 78– 92, 2000.

Tsuda, T., S. Kato, A. H. Manson, et al., Characteristics of semidiurnal tides observed by the Kyoto meteor radar and Saskatoon medium-frequency radar, *J. Geophys. Res., 93,* 7027-7036, 1988.

Tsumi, M., T. Tsuda, T. Nakamura et al., Wind Velocity and Temperature Fluctuations due to a Two-day Wave Observed with Radio Meteor Echoes, *J. Geophys. Tes.,* 101, 9425-9432, 1996.

Vincent, R. A., T. Tsuda and S. Kato, Asymmetries in mesospheric tidal structure, *J. Atmos. Terr. Phys., 51,* pp 609-616, 1989.

Williams B.P., R. G. Roble, and C. Y. She Seasonal climatology of the nighttime tidal pertubation of temperature in the midlatitude mesopause region. *Geophys. Res. Letter,* Vol.25 3301-3304, 1998.

Chapter 7 Conclusion, Implication and Future work

The CSU Na-lidar has been observing the thermal and dynamic behaviors of the mesopause region above Fort Collins, CO (105° W, 40.5° N) for over a decade. The full-diurnal-cycle observation capability, starting from May 2002, adds a new dimension into the CSU lidar history. It makes 24-hour continuous observation possible, allowing the investigation of tidal-period perturbations and of the associated interactions with gravity waves on the one hand and with planetary waves on the other. It gave us the first yearlong data set, covering full diurnal cycles, on mesopause region temperature, zonal and meridional winds. From the analysis of this yearlong data set, one obtains the seasonal variation of mean values as well as of the solar thermal tides (diurnal and semidiurnal) above Fort Collins, CO. The science objectives of this thesis research is to acquire the yearlong data set and to perform a consistent study of seasonal variation of diurnal and semidiurnal tidal oscillations over Fort Collins, CO, and to assess the associated variability based on this data set and limited additional data set from more recent observations. In order to perform robust long-period observation that led to this data set, technical improvement on Faraday filter, whose robustness is required for long-period observation under sunlit conditions, were made and implemented. Both the technical achievement and science results are summarized below.

Although the first temperature observation under sunlit condition was made in 1996 using a Faraday filter in the lidar receiver system (a CSU innovation for lidar), the filter

transmission function required re-calibration in every few days. This is mainly due to the unavoidable environmental temperature changes that occurred at the field site, which altered the temperature around the tip and the vapor pressure of sodium cell inside the Faraday filter, despite the fact that the cell temperature was controlled to a preset value. The problem became more acute when the system was used for simultaneous temperature and line-of-sight wind measurements, since the requirement for a stable transmission function is more stringent for wind measurements. We solved this problem by employing dual temperature controls on the sodium cell, setting the cell body and the tip-off region at different temperatures, respectively, at 170°C and 148°C, thereby controlling the temperature and vapor pressure of the sodium atoms separately and independently. In this manner, we were able to maintain the density of Na atoms in the cell nearly constant during tens of hours of operation. In addition, we turn the set-points for the cell temperature to 50°C and for the tip-off region to 0°C, when the Faraday filter is at standby, so that the condition of the Na cell is less susceptible to ambient temperature changes. This modification and procedural change not only gives us a robust Faraday filter, its lifetime was also much prolonged. The concept for needing independent controls on temperature and pressure of the Na cell is obvious. Without its proper implementation, the Faraday filter with moderate thermal mass (like ours) would not have a chance to be stable. A new generation of Faraday Filter, designed by Biff Williams and Kam Arnold, is now under construction, and hopefully it will soon be deployed for the system. The new novel design could combine both channels with only one Faraday filter and at the same time recover the 50% signal loss resulting from the first linear polarizer. Another big improvement is going to be the new 30-inch telescopes,

which are already standing in the observation room waiting for integration into the lidar system. This will increase the optical signal by a factor of 4.6. The new Faraday Filter will increase the signal under sunlit condition by another factor of 2. The factor of 4.6 improvement at night will reduce the measurement error by a factor of 2.2. Because the larger telescope will also increase noise from the sky background, which dominates the photon noise near local noon, the improvement resulting from the nearly 10 times increasing signal is more difficult to assess. Hopefully, we will be able to quantify these improvements experimentally.

The tidal analysis based on the yearly full-diurnal-cycle data binned bimonthly produces diurnal and semidiurnal amplitudes and phases in general agreement with present models (GSWM00, GSWM02 & TIME-GCM02). The agreement is best with the GSWM00 model for diurnal tides. Discrepancies do exist. However, for the bimonthly periods with discrepancy between observation and model predictions, we analyzed the more recent data taken during the same bimonthly period, and found general agreement between two data sets. This preliminary consistency test suggests that the reported tidal oscillations based on diurnal-cycle observation likely represent climatology of tides reliably. As this campaign continues for two more years, we should obtain enough data for a robust evaluation on the seasonal variation of climatology as well as variability of diurnal and semidiurnal tidal oscillations.

Excellent agreement between observation and GSWM00 prediction in diurnal tides suggests that in general, migrating diurnal tide dominates the diurnal-period oscillations observed over Fort Collins, CO. On the other hands, the models underestimate the observed semidiurnal tidal amplitudes in non-winter months, suggesting that there exist

considerable local perturbations at the semidiurnal period. While agreement suggests possible understanding, discrepancy would implicate interesting discovery, which warrants further study. In this connection, many interesting and unknown phenomena showed up in our limited tidal analyses. For example, the temperature diurnal tide in the Nov-Dec period showed trapped mode characteristic, though the zonal and meridional wind showed downward phase progression. The observed trapped diurnal phase in Nov-Dec temperatures appears to persist from one year to the next, suggesting the existence of a local source in favor of midnight heating during this period. What causes this heating is still not clear. This is only one illustration of the richness of the data set; many more cases worthy of model studies could be forthcoming. The accompanying Na density and the associated dynamics and chemistry are not studied in this thesis, but the data acquired could be equally revealing for scientists who are interested in Na chemistry.

Our group is funded to continue similar observation for two more years; this will no doubt produce more interesting case studies as well as reliable tidal-period climatology and variability invoking the interaction with gravity waves and planetary waves. We have also begun to engage modelers, notably at NCAR, as well as radar data in collaboration with colleagues in Canada and Japan. In addition, our lidar is a ground-based station in the CEDAR-TIMED collaboration. As such we can take the advantage of TIMED satellite data by working with those scientists and their global information on waves and dynamics. We hope to make timely contributions to the active community science efforts to advance understanding of the very interesting MLT region of the atmosphere.

Appendix 1 Bimonthly Mean Diurnal Mean Temperatures, Zonal and Meridional Winds

In this appendix, we present the bimonthly mean temperature; zonal wind and meridional wind based on full diurnal cycle observations. In the following figures, both the profiles of observed diurnal means and the constant terms in the tidal means (fit means) are plotted against the 2002 version of TIME-GCM diurnal means.

In Fig. I-1, we see an agreement within 10K for the Mar-Apr, Sep-Oct, and Nov-Dec bimonthlies. However, the TIME-GCM predicts 20K warmer winter mesopause in Jan-Feb and 20K cooler summer mesopause in May-Jun and Jul-Aug. The overestimation in winter-summer mesopause temperature difference is likely the result of stronger gravity wave activities being input into the TIME-GCM [Oberheide et al., 2003, see page 143.]. Since the nighttime temperature climatology (with and without Mt. Pinatubo warming effect removed) over Fort Collins based on eight years of nocturnal observation was published [She et al., 2000, see page 81], we also plot the nocturnal bimonthly temperature profiles with Mt. Pinatubo effect removed (in blue square) in Fig.I-1 for comparison. Considering the possible contamination due to diurnal tide in the nocturnal temperatures and the diurnal means derived from only one years of observation, the agreement is considered to be good. The discrepancy between 85 and 95km in non-summer months (Jan-Feb, Mar-Apr, and Sep-Oct in Fig. I-1) with nocturnal temperatures being ~5K warmer, is attributable to chemical heating at night in the mesopause region [Mlynzak and Solomon, 1993, see page 81]. The day-night difference in this connection has been discussed previously [Chen et al., 2000, see page 54].

A similar situation exists in the bimonthly zonal wind comparison between model and observation. In Fig. I-2, we show bimonthly zonal wind comparison between observation and TIME-GCM prediction. They are in very good agreement in equinox, i.e., Mar-Apr and Sep-Oct bimonthlies. In other months, both observation and prediction show zero crossing of zonal wind in the mesopause region. The TIME-GCM however overestimated the west wind magnitudes in winter and underestimated the east wind magnitudes in

summer. The agreement in equinox months and discrepancy in solstice months suggests that the gravity wave parameterization in the TIME-GCM still requires adjustment.

In Fig. I-3, we compare observed meridional winds to the TIME-GCM predictions. As expected, the prediction captures well the meridional circulation in response to the seasonally dependent gravity wave activities with flows from summer to winter poles in solstice and flows in quiescent condition at equinox. The meridional wind is negative between 80 and 90km in winter and positive for the entire altitude range (80 to 100km) in summer, reflecting stronger gravity wave activities in winter (as compared to summer), thus breaking at a lower altitude. The observation mean fields are in general agreement with the model prediction with noticeable variations along the altitude. For example, the observed Mar-Apr meridional wind varies from ~-10m/s below 92km to ~4m/s above 92km, while the prediction stays within ±2m/s. In the Jan-Feb plot, the observed meridional wind and the TIME-GCM prediction both cross zero at 92km and 95km, respectively, while the wind speed changed from –30m/s (-10m/s) to 20m/s (3m/s) for observation (prediction) below and above the zero point.

Appendix I: Mesopause Mean Fields

Temperature Mean

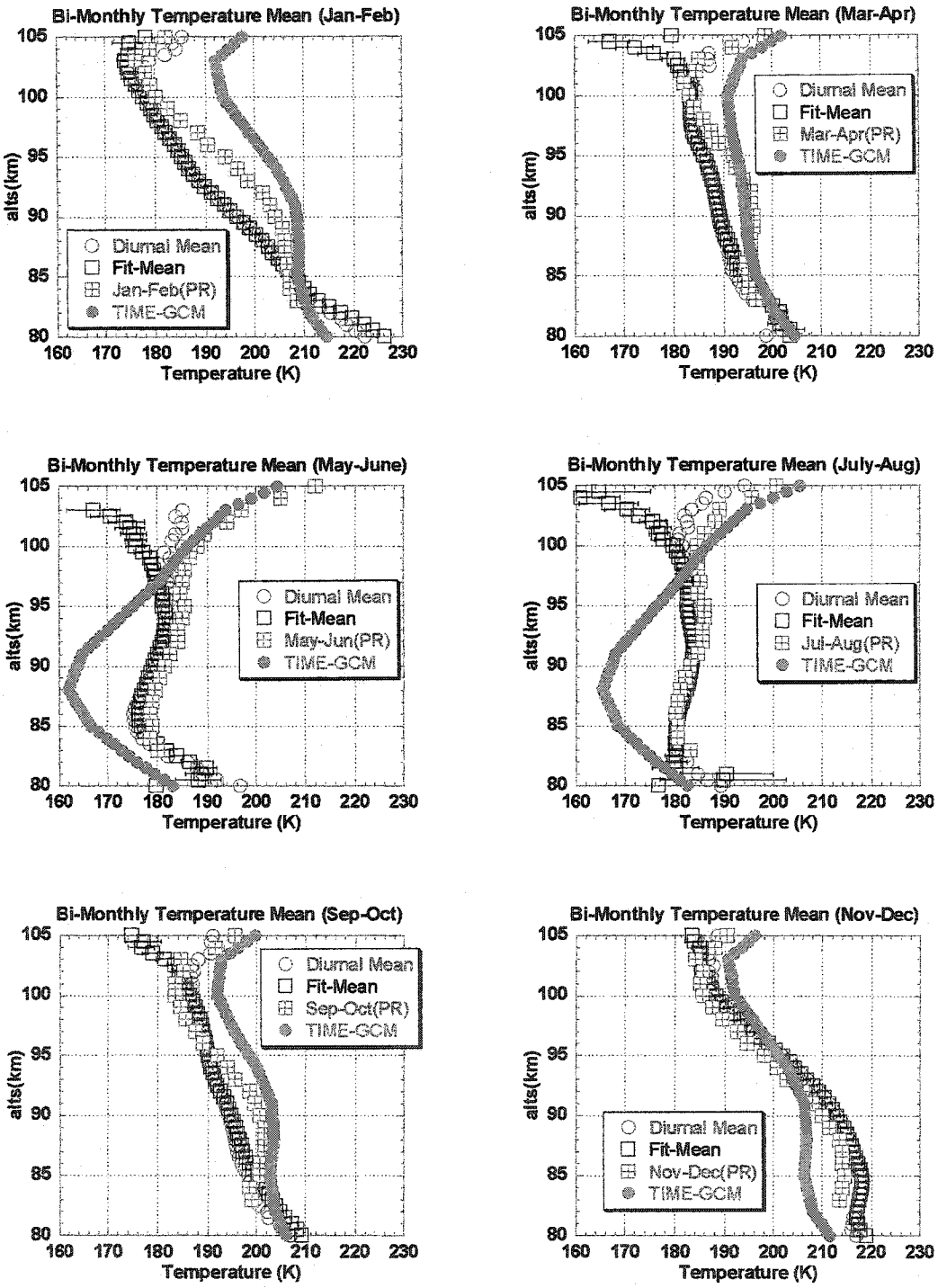

Fig. I-1Bi-monthly mean temperature

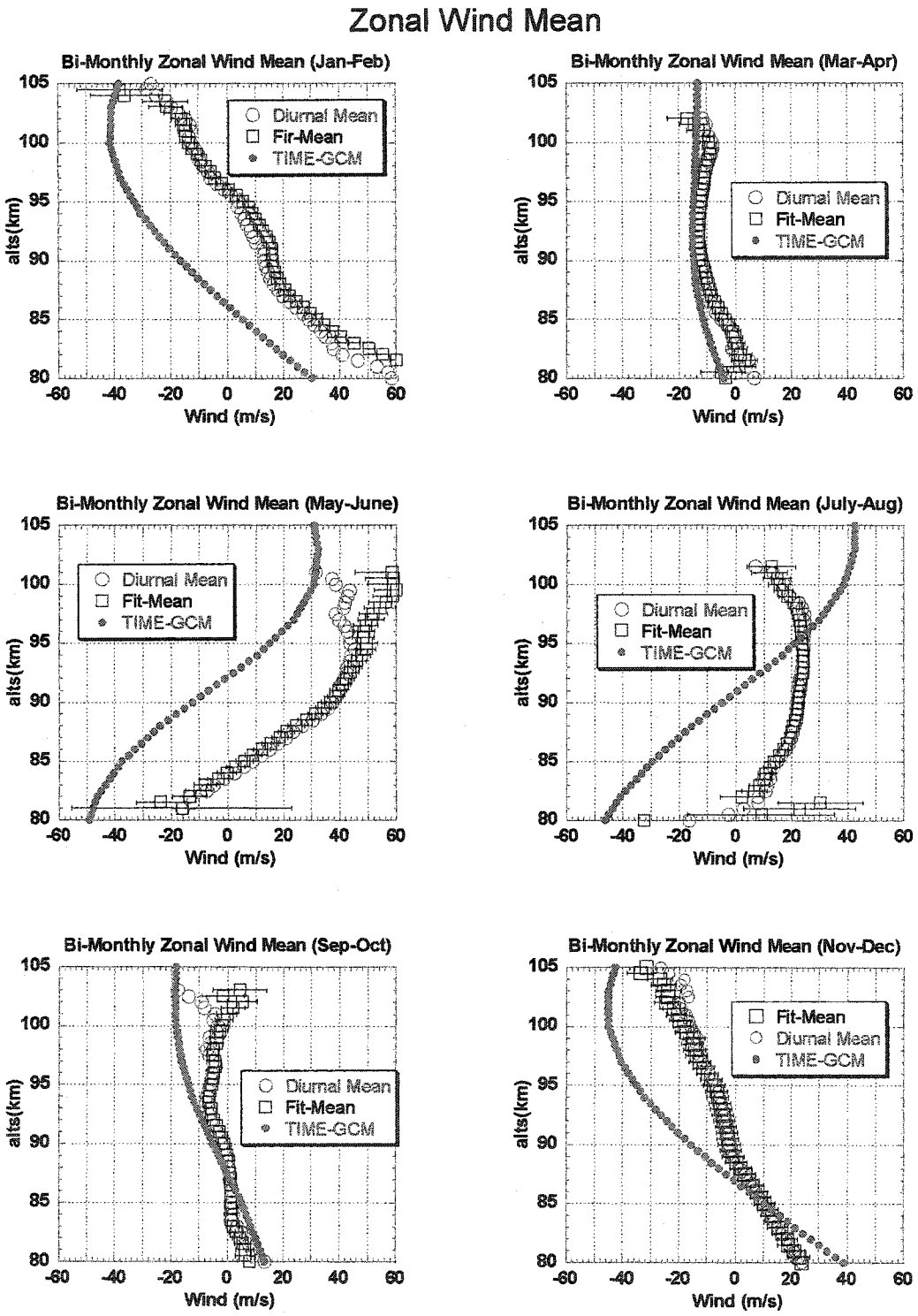

Fig. I-2 Bi-monthly mean zonal wind

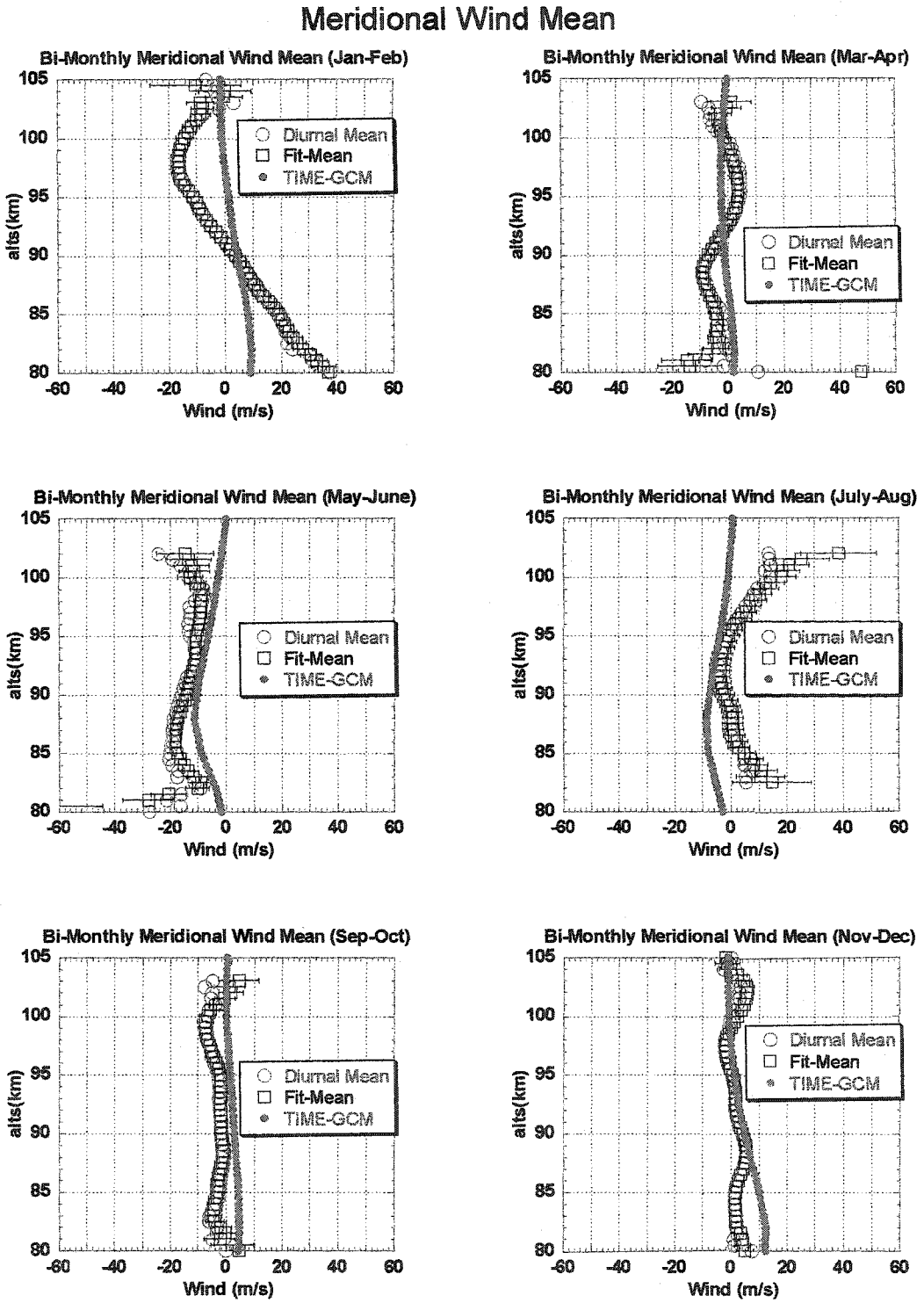

Fig. I-3 Bi-monthly mean meridional wind

Appendix II: Day-to-day tidal variations

In this section, based on the first yearlong diurnal cycle observation of the CSU lidar observation, all 29 sets of continuous diurnal cycle observation of tidal result are plotted. This gives some idea of the day-to-day tidal behavior variation above Fort Collins. We put every complete diurnal cycle tidal component result of the bi-month period (same period we chose in the thesis) in one figure. For example, in Fig II-1, we collect the diurnal and semidiurnal tides' amplitude and phase in Jan-Feb period. The top two rows are diurnal tidal (temperature, zonal and meridional wind) behaviors, including the diurnal amplitude (1^{st} row) and diurnal phase (2^{nd} row). The two rows on the bottom part of the figure include the semidiurnal tidal behaviors of the same period. Every complete 24-hour data set is marked with related UT day.

Overall the day-to-day observed tidal variation is generally consistent in every period, although during some periods this variation is considerable. For example, in the March and April period of 2002 (Fig.II-2), the temperature semidiurnal tidal phase behavior shows significantly different behavior. During the November to December period, the meridional wind diurnal phases are all over the plot, whereas most of the temperature diurnal phases of that period show somewhat trapped wave mode-like characteristic. All these are unsolved mysteries right now, and need further diurnal cycle observation.

To minimize the statistical error, but also to be able to capture the seasonal variation of the tidal perturbation, we use the bi-monthly data period in this thesis.

Mesopause Day to Day Tidal Variation (T: Temperature, U: Zonal Wind, V: Meridional Wind)

Diurnal

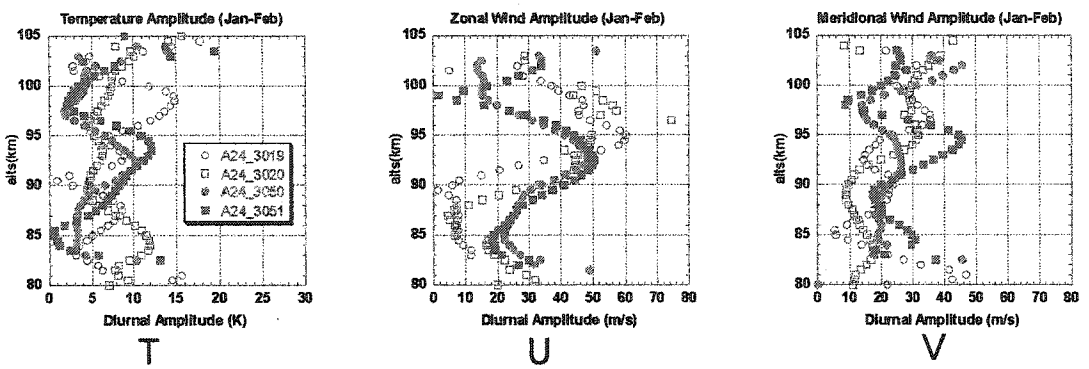

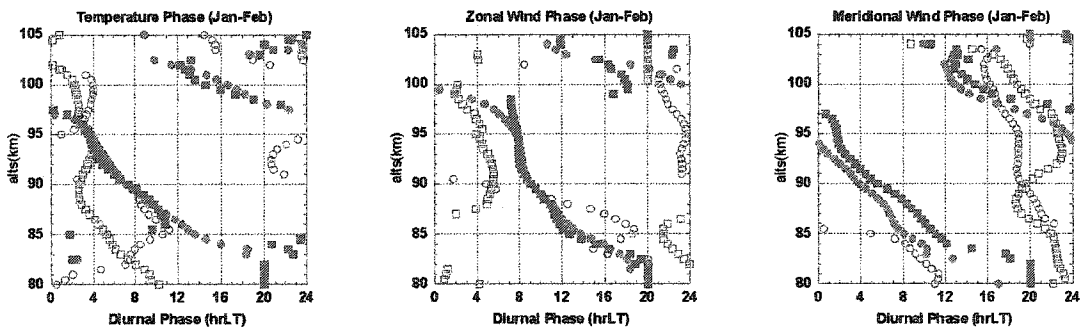

Semidiurnal

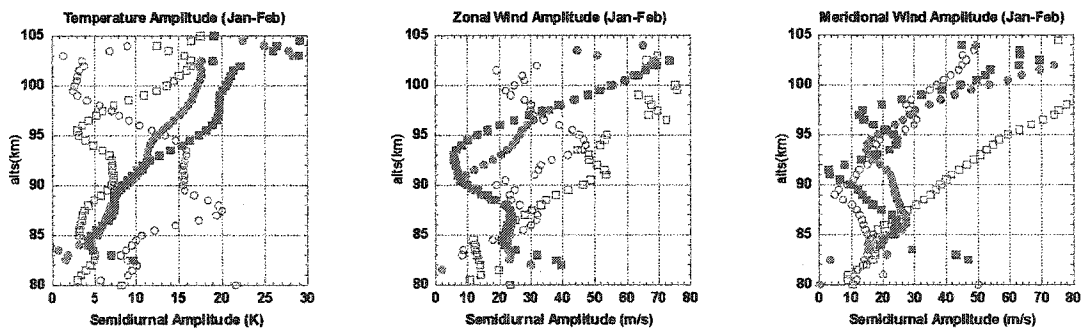

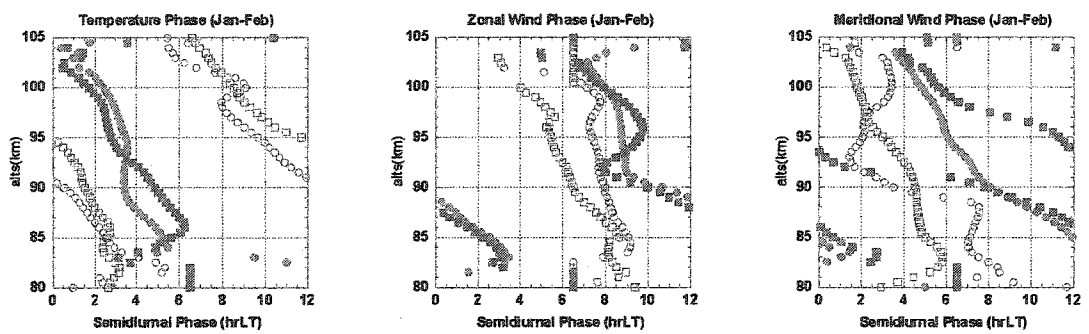

Fig. II-1: Jan-Feb

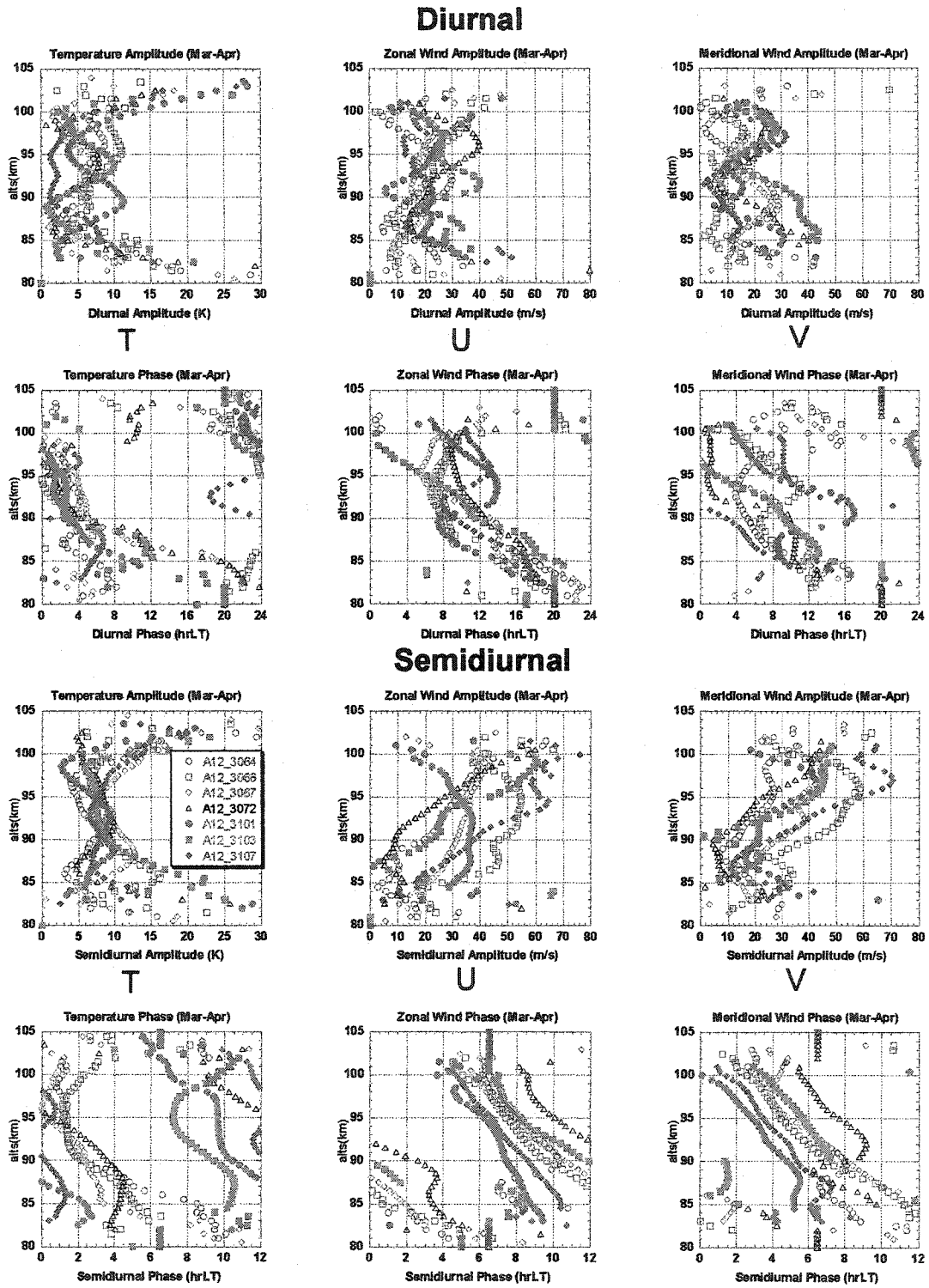

Fig. II-2 Mar-Apr

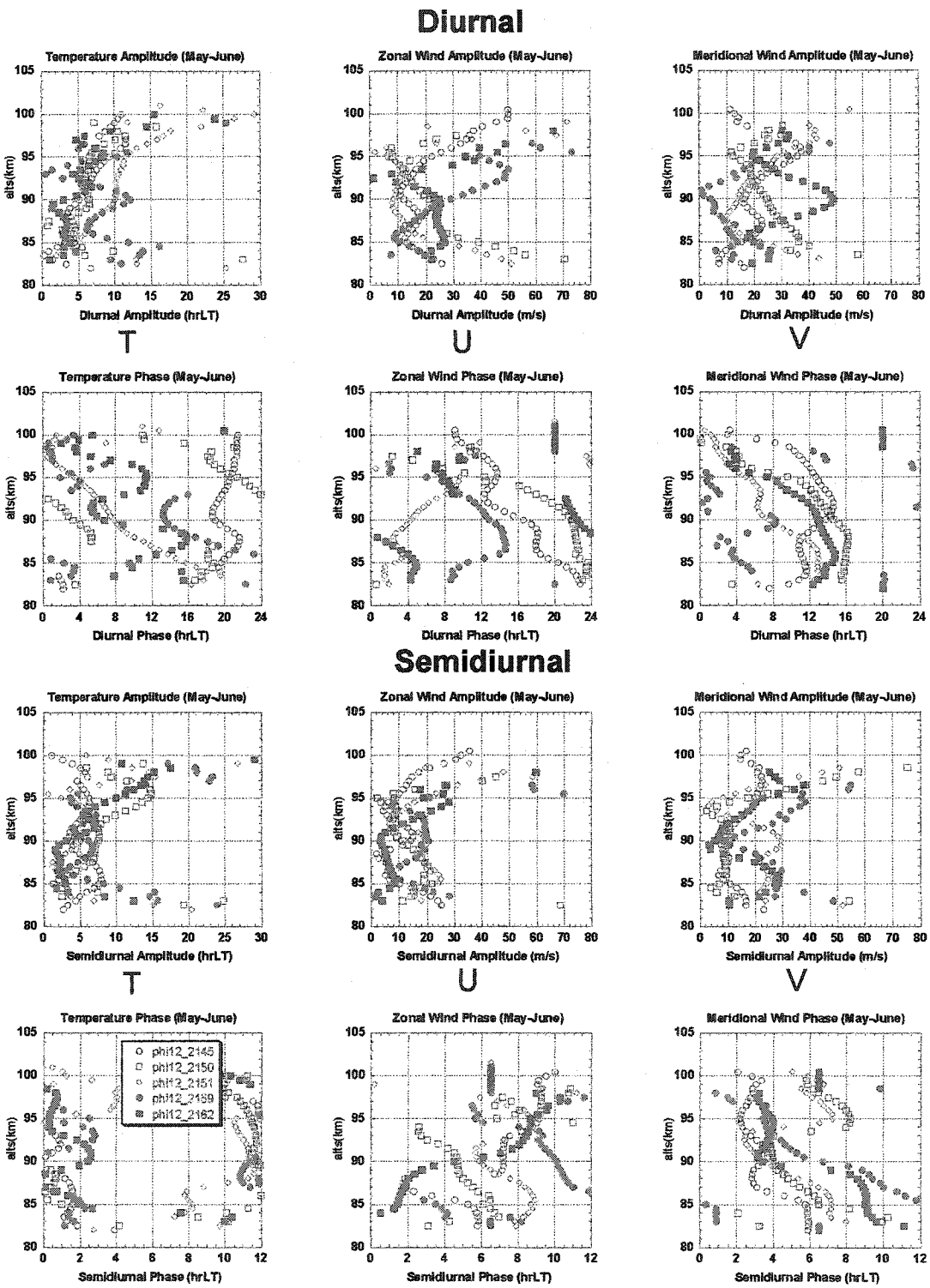

Fig. II-3 May-June

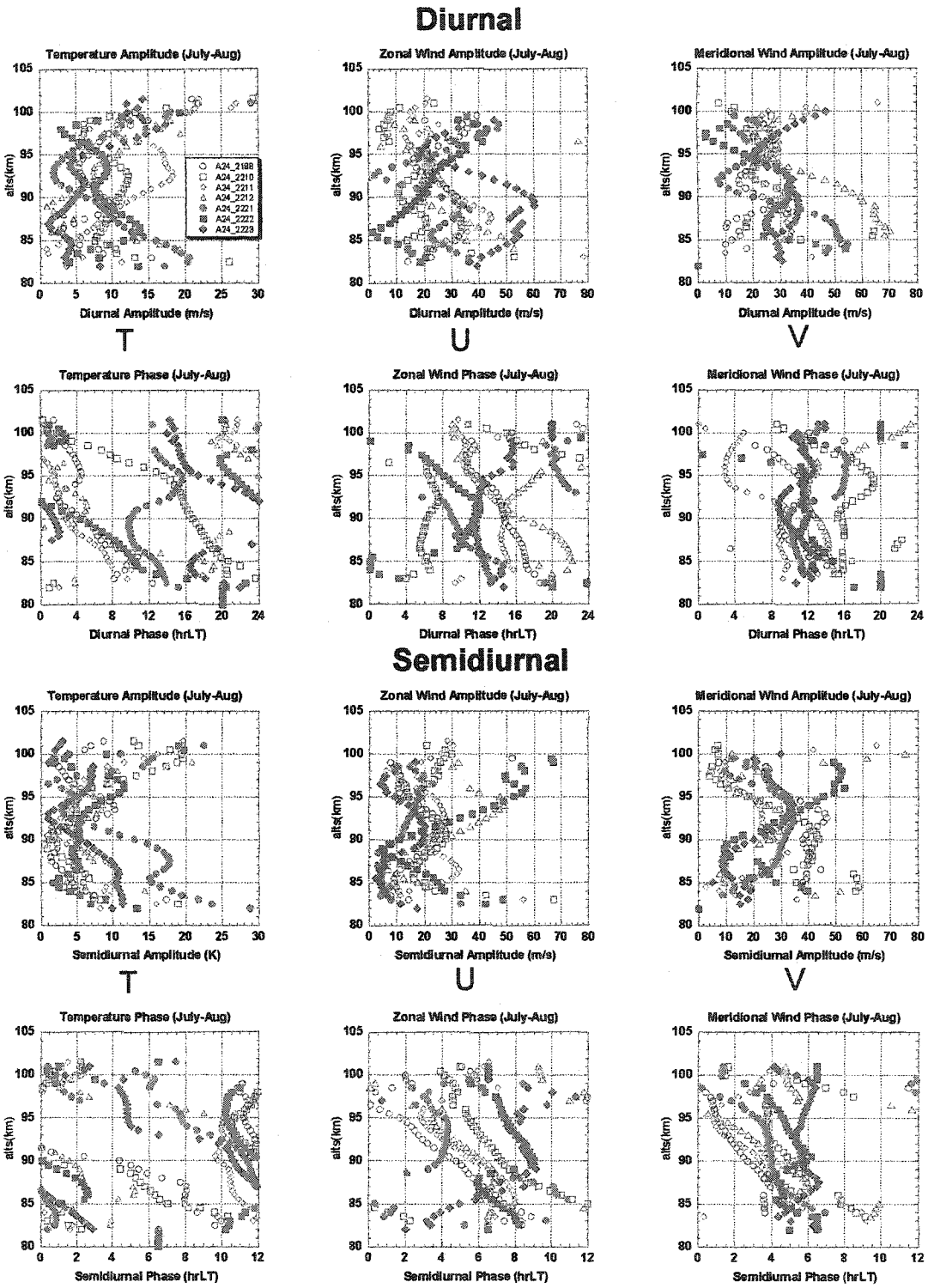

Fig. II-4 July-Aug

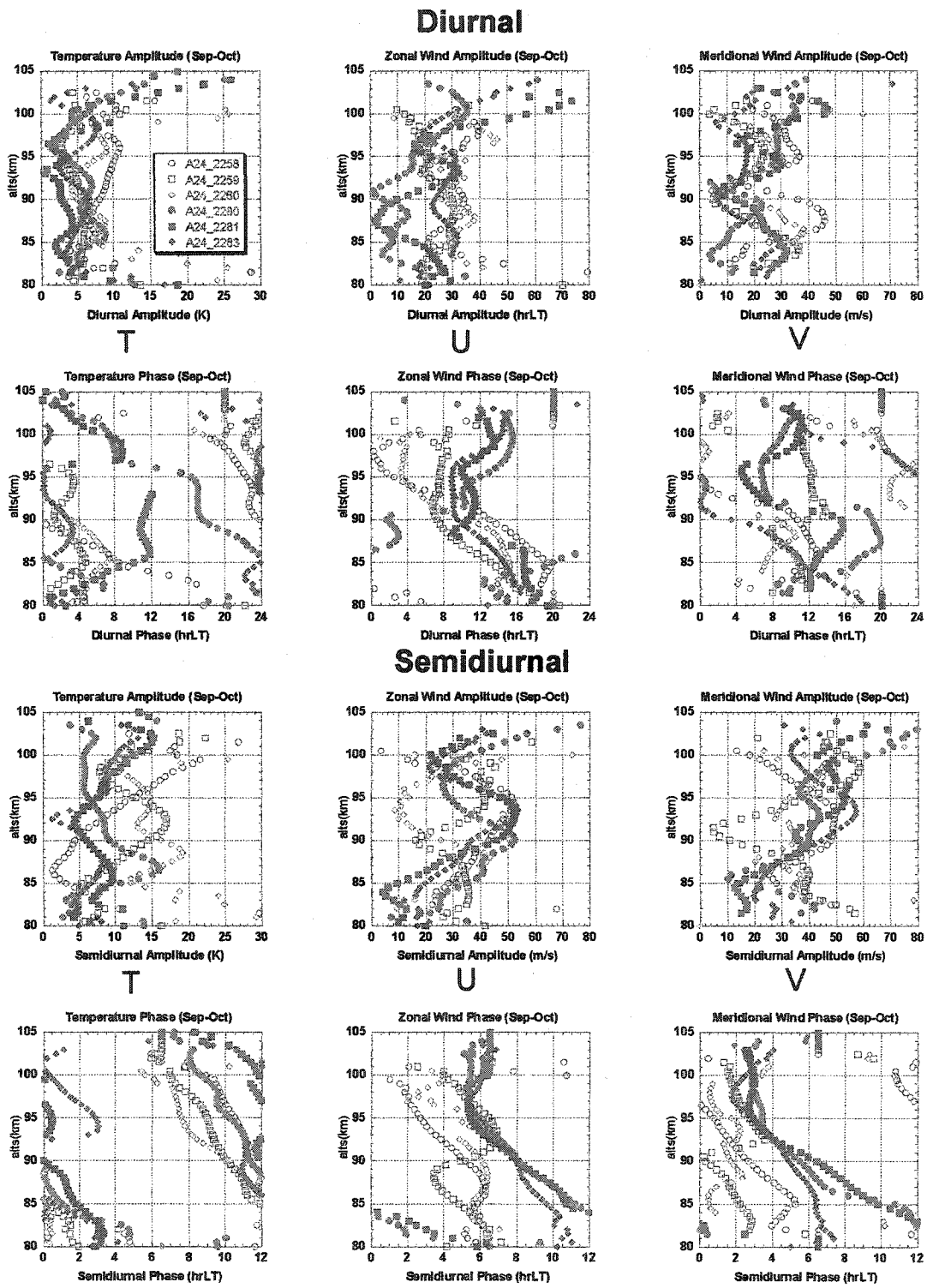

Fig.II-5 Sep-Oct

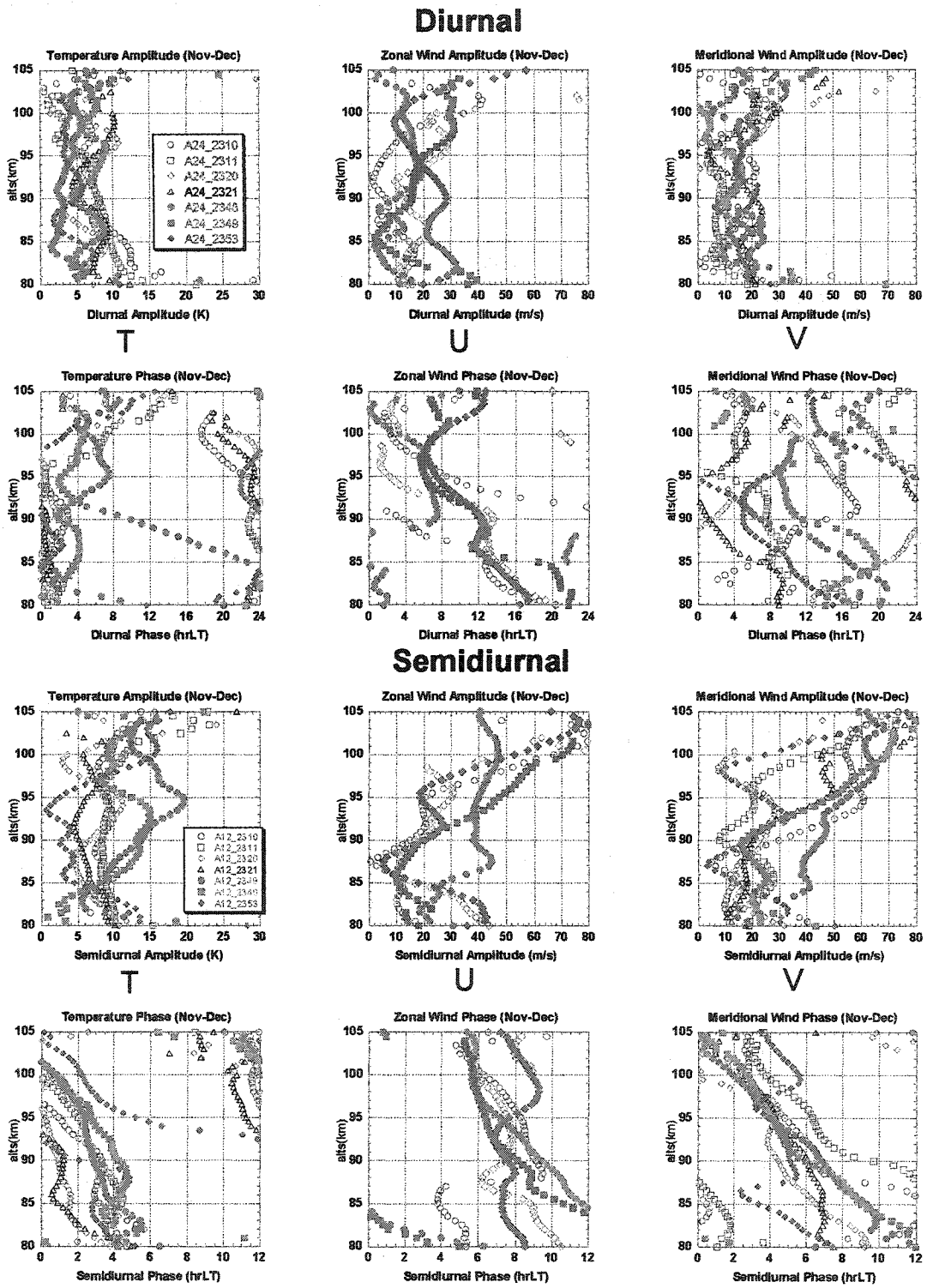

Fig. II-6 Nov-Dec

Appendix III: Tidal consistency

We have shown the temperature tidal consistency study of May-June, July-Aug and Nov-Dec periods in Chapter 6. To complete those discussions, we list the related zonal and meridional wind tidal behaviors of those periods in 2002 and 2003.

For diurnal tide consistency, the zonal and meridional winds diurnal tide behaviors in these three periods show consistency in 2002 and 2003 (both diurnal amplitudes and diurnal phases). But, nothing like the temperature diurnal phase trapped mode behavior in Nov-Dec period, in both 2002 and 2003, the zonal and meridional winds diurnal phases in this period (Fig. III-1 & Fig. III-2) show consistent typical propagating mode characteristic: downward diurnal phase progression. This phenomenon is very interesting and needs further study.

For the zonal and meridional semidiurnal tide consistency study (Fig. III-3 and Fig. III-4), again, during the Nov-Dec period, both semidiurnal amplitudes and phases show good consistency. Although the summer months semidiurnal winds tides' behaviors are not as consistent as winter months, they still show some consistencies. However, in July-Aug period of 2002 and 2003, we saw some inconsistent events in the zonal and meridional wind semidiurnal amplitudes. Both zonal and meridional wind semidiurnal tidal amplitudes show similar vertical behavior below 94-94km, but above this level, 2003 results are increasing along with the altitude increasing, whereas the 2002's results are showing opposite behavior. Amazingly, the temperature semidiurnal amplitudes of the same period in these two years (Fig. 6-13) also show the opposite vertical structure.

Appendix Plot III: Mesopause Winds (Zonal & Meridional) Tidal Consistency

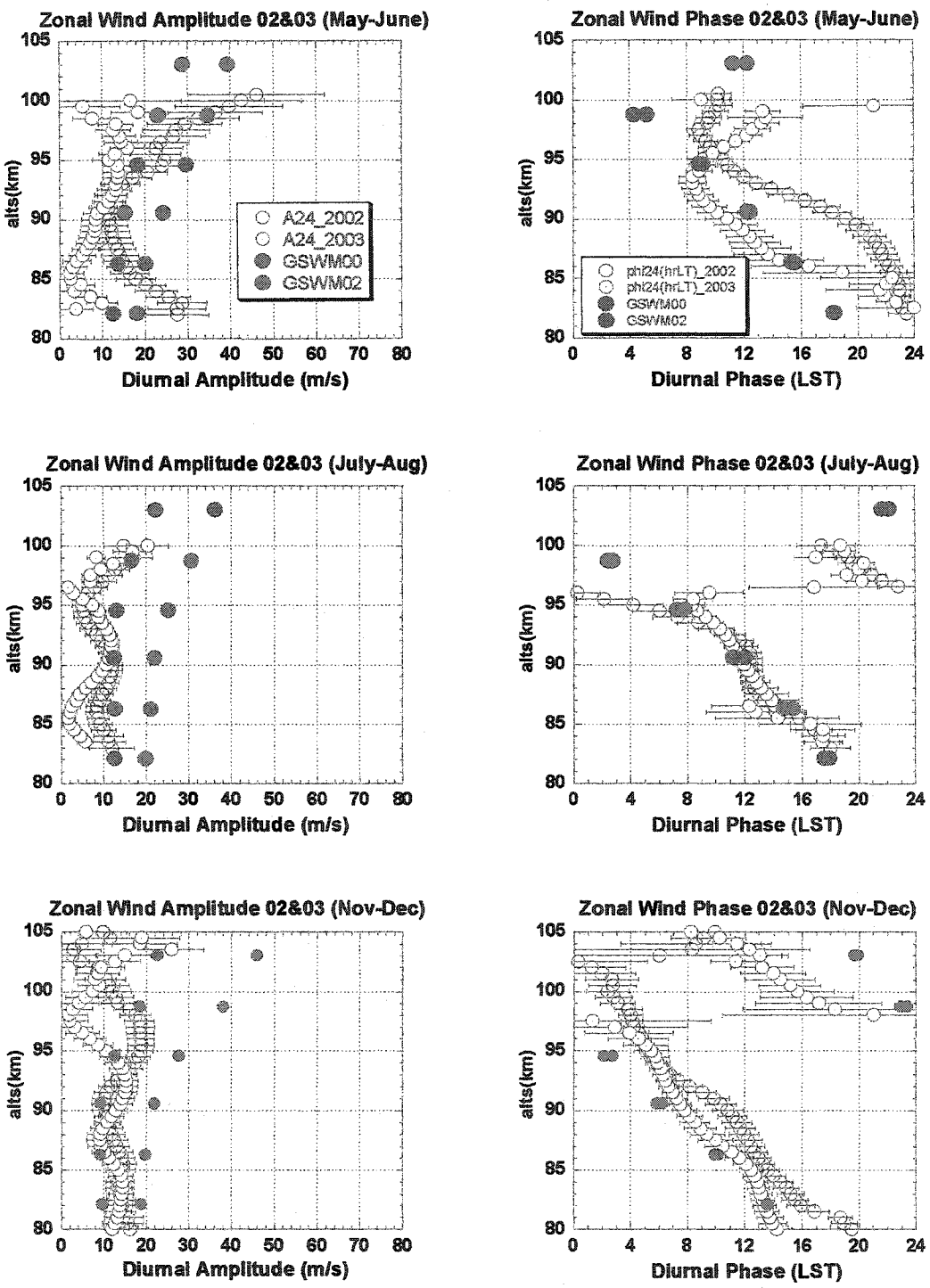

Fig. III-1 Zonal Wind Diurnal Tidal Amplitude & Phase 2002 vs. 2003

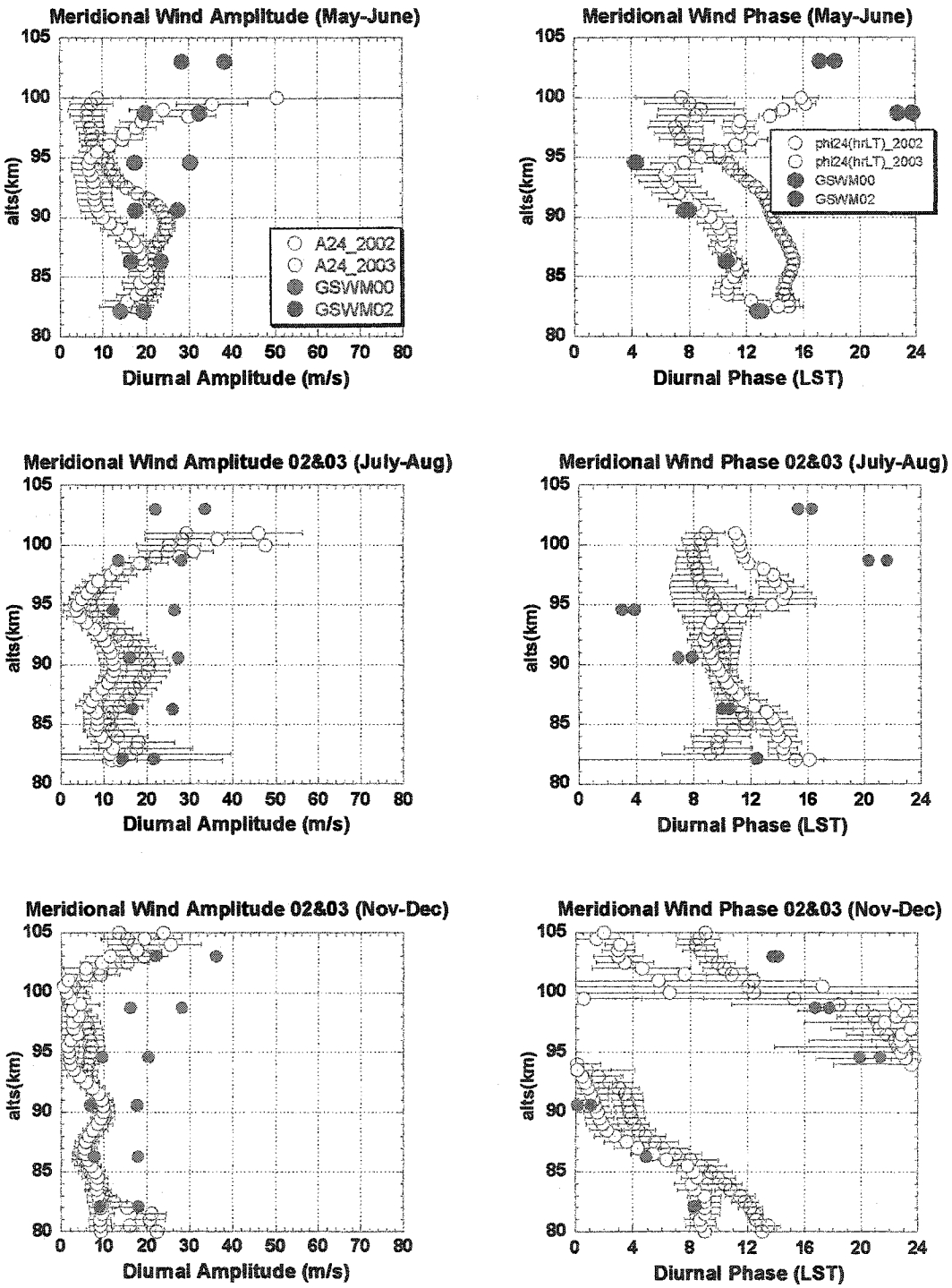

Fig. III-2 Meridional Wind diurnal Tidal Amplitude & Phase 2002 vs. 2003

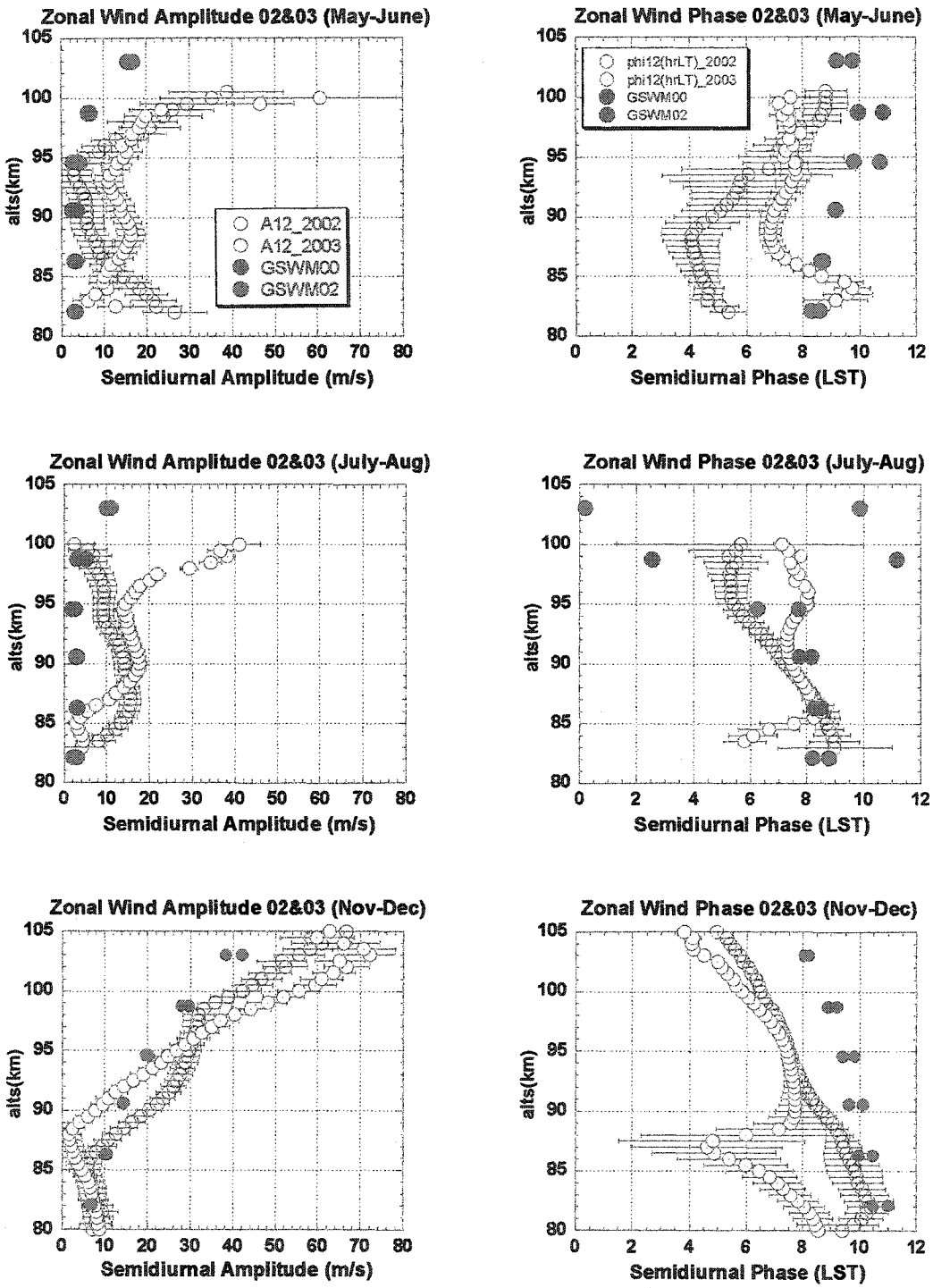

Fig. III-3 Zonal Wind Semidiurnal Tidal Amplitude & Phase 2002 vs. 2003

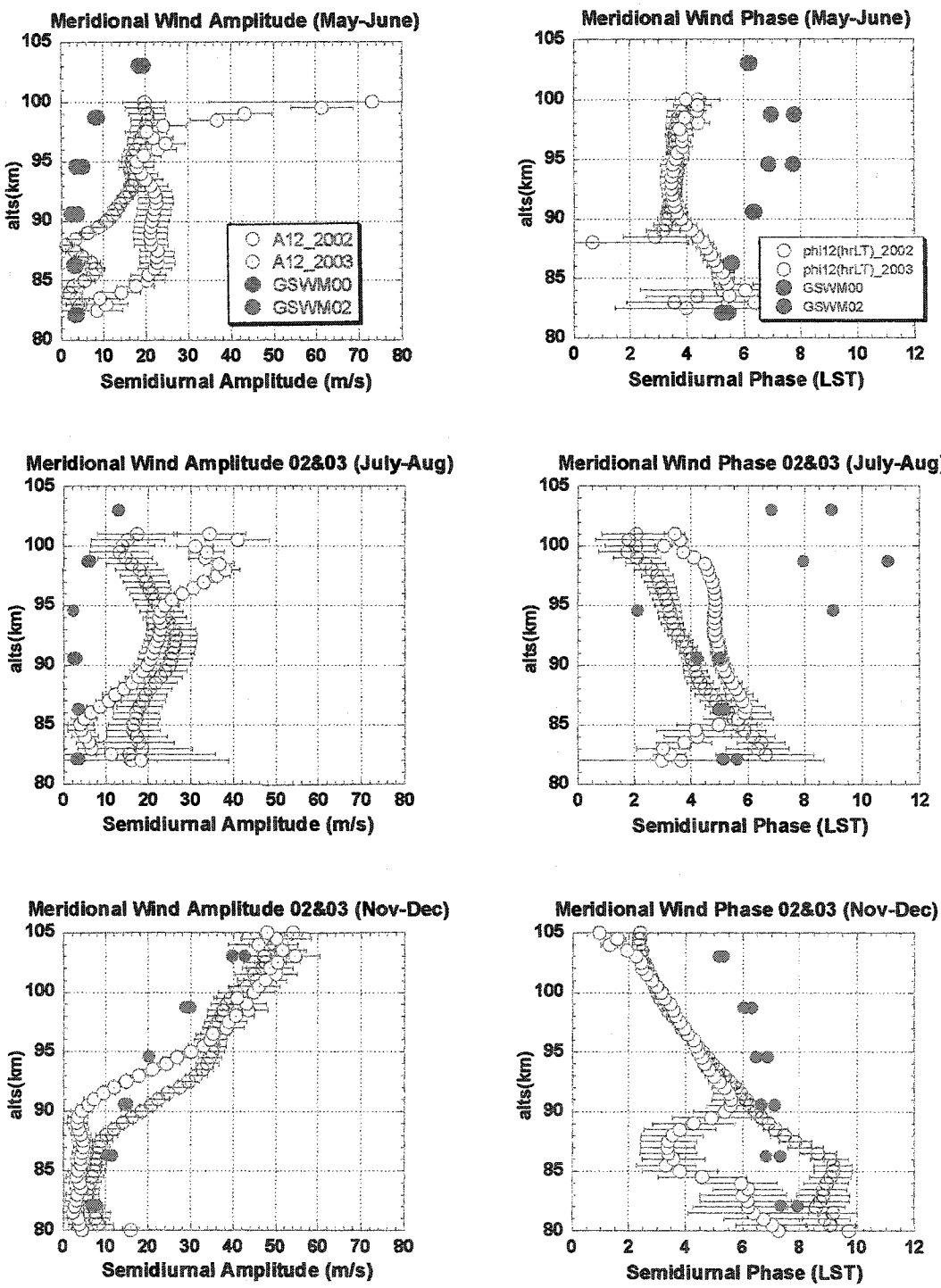

Fig. III-4 Meridional Wind Semidiurnal Tidal Amplitude & Phase 2002 vs. 2003